Magnetoplasmon Excitations and Magnetotransport Properties of Two-Dimensional Electron Gas in GaN/AlGaN Heterostructures

Karol Nogajewski
Faculty of Physics
University of Warsaw

A thesis submitted for the degree of
Doctor of Philosophy

Warsaw 2013

To the Memory of
my dearest uncle
Mirek

Podziękowania /Acknowledgements

W pierwszej kolejności chciałbym podziękować mojemu Promotorowi, dr. hab. Jerzemu Łusakowskiemu, za ogromne wsparcie, którego doświadczyłem z Jego strony w czasie całych studiów doktoranckich. W szczególności jestem mu wdzięczny za to, że pomimo wielu różnic, jakie dzielą nasze charaktery, zawsze próbował spojrzeć na problemy, które napotykałem, z mojej perspektywy. Nigdy również nie sprzeciwił się stanowczo, kiedy wiedziony własną intuicją fizyczną chciałem eksplorować ścieżki, co do sensowności których nie zawsze był przekonany.

Profesor Marian Grynberg służył mi swoją wiedzą i życiową mądrością ilekroć tylko tego potrzebowałem. Bez wielu godzin rozmów na tematy wykraczające niekiedy daleko poza sprawy naukowe, nie tylko niniejsza rozprawa nie miałaby obecnego kształtu, ale również ja sam byłbym pod wieloma względami innym, w moim prywatnym odczuciu gorszym, człowiekiem.

Poczynając od czasów studiów magisterskich, dr Krzysztof Karpierz ukształtował mnie w dużej mierze jako fizyka eksperymentatora. Znakomitą część swoich umiejętności i technicznej wiedzy niezbędnej w codziennej praktyce laboratoryjnej zawdzięczam właśnie jemu.

Profesorowi Wojciechowi Knapowi pragnę podziękować za zaufanie, którym darzył mnie od naszego pierwszego spotkania. Bez jego przeświadczenia, że jestem właściwą osobą do podjęcia badań nad wzbudzeniami magnetoplazmowymi w strukturach GaN/AlGaN, ta praca nigdy by nie powstała.

I am indebt to Prof. Michael S. Shur, who kindly provided me with the samples and helped a lot during preparation of the manuscripts that have been published so far.

I would like to thank Prof. Vyacheslav V. Popov, who guided me through theoretical aspects of the solid-state plasma physics at the initial stage of my studies on this subject.

I am very grateful to Dr. Milan Orlita for his thorough help with the Fourier experiment as well as for careful proofreading of the following thesis.

Doktorowi Markowi Potemskiemu chciałbym podziękować za szansę, którą od niego otrzymałem, jak również to, że mimo początkowych trudności i wielu nerwowych chwil nie zmienił swojej decyzji.

Doktor hab. Andrzej Witowski pomógł mi bardzo w przygotowaniach do przeprowadzenia badań z wykorzystaniem spektrometru Fourierowskiego, jak również w pierwszej fazie opracowania danych eksperymentalnych, za co pragnę mu w tym miejscu gorąco podziękować.

Marcinowi Białkowi dziękuję za wsparcie, na które mogłem liczyć z jego strony

w sprawach związanych z utrzymywaniem układu eksperymentalnego w pełnej gotowości operacyjnej.

I would like to thank Dr. Frédéric Teppe for his kindness, support and encouraging me to write my PhD thesis in English.

Jestem wdzięczny prof. Jackowi Kossutowi, prof. Witoldowi Bardyszewskiemu, dr. hab. Krzysztofowi Byczukowi, prof. UW oraz dr. hab. Piotrowi Szymczakowi za wiele cennych rozmów, które pogłębiły znacząco moje rozumienie problemów poruszonych w niniejszej rozprawie.

Dziękuję mojej mamie za to, że nigdy dotąd nie przestała we mnie wierzyć i wspierała mnie we wszystkich działaniach, jakie podejmowałem. Choć czasami może być to trudne do zauważenia, świadomość tego, że jest i nieustannie czuwa nade mną, pomaga mi stawiać czoła nawet najtrudniejszym wyzwaniom, jakie napotykam na swojej drodze.

Dzięki Ewie mam mam dla kogo żyć, uśmiechać się i spoglądać w przyszłość z nadzieją, że jutrzejszy dzień będzie jeszcze lepszy. Bez tego przeświadczenia niejednokrotnie już przestałbym dostrzegać sens w tym, czym się na co dzień zajmuję.

Dziękuję także moim Bliskim i Przyjaciołom za ogrom życzliwości, troski i wsparcia, jakich doświadczyłem od nich przez dotychczasowe lata. Bez ich pomocy wiele rozdziałów mojego życia nie zostałoby w ogóle napisanych, a inne z pewnością nie doczekałyby się szczęśliwego zakończenia.

Streszczenie

Azotek galu (GaN) jest obecnie jednym z najważniejszych półprzewodników, zwłaszcza z punktu widzenia wysokotemperaturowych i wysokoczęstotliwościowych zastosowań w dziedzinach takich jak szybka elektronika, optoelektronika oraz optyka światła niebieskiego, fioletowego, a także ultrafioletu. Biorąc pod uwagę badania podstawowe, skoncentrowane na fundamentalnych zjawiskach, do jakich dostęp dają struktury półprzewodnikowe z rodziny III-V, wciąż pozostaje jednak w cieniu układów opartych na arsenku galu. Dotyczy to w szczególności kolektywnych wzbudzeń dwuwymiarowego gazu elektronowego (z ang. *two-dimensional electron gas*, 2DEG). Ważną klasą tych wzbudzeń są oscylacje gęstości ładunku, nazywane zwykle oscylacjami plazmowymi lub falami plazmowymi dla podkreślenia faktu, że ochłodzony do odpowiednio niskiej temperatury 2DEG o dużej gęstości zyskuje wszystkie cechy, jakie są uznawane za charakterystyczne dla plazmy - jednego z czterech podstawowych stanów skupienia materii. W obecności zewnętrznego pola magnetycznego (B), fale plazmowe stają się potężnym narzędziem w próbkowaniu nielokalnych właściwości 2DEG, które wedle wiedzy autora niniejszej pracy, nie były jeszcze systematycznie badane w układach opartych na GaN. Stąd też, podstawowym celem tej rozprawy było przynajmniej częściowe wypełnienie powyższej luki poprzez przeanalizowanie wpływu efektów nielokalnych na widmo wzbudzeń poddanej wpływowi pola magnetycznego dwuwymiarowej plazmy elektronowej w heterostrukturach GaN/AlGaN.

Badane próbki miały postać tranzystorów polowych o dużej powierzchni ($1{,}6\,\mathrm{mm}\times 1{,}6\,\mathrm{mm}$), wyposażonych w bramki o konstrukcji siatek dyfrakcyjnych o różnym okresie (L) i szerokości (W) tworzących je pasków metalu. Rozważono cztery struktury o okresach z przedziału $2{,}0\,\mu\mathrm{m} - 4{,}0\,\mu\mathrm{m}$ i odstępie pomiędzy sąsiadującymi ze sobą paskami siatki, $S = L - W$, równym $0{,}35\,\mu\mathrm{m}$ lub $0{,}85\,\mu\mathrm{m}$. Podstawową rolą siatek było zapewnienie sprzężenia optycznego pomiędzy wzbudzeniami magnetoplazmowymi w 2DEG a padającym na próbkę promieniowaniem elektromagnetycznym. Spolaryzowane elektrycznie, służyły one również do kontroli koncentracji 2DEG w kanale tranzystora. Poza strukturami ze sprzęgaczami siatkowymi mieliśmy także do dyspozycji próbkę referencyjną o dokładnie tych samych, co wyżej wymienione, wymiarach geometrycznych, ale nieposiadającą bramki. Wszystkie próbki zostały wytworzone na wysokiej jakości heterostrukturze GaN/AlGaN wyhodowanej stroną galową do góry na podłożu szafirowym za pomocą techniki MEMOCVD® (z ang. *Migration-Enhanced Metal-Organic Chemical Vapor Deposition*). Każda z nich zawierała kwazi-dwuwymiarowy gaz elektronowy o gęstości powierzchniowej $N_0 \sim 10^{13}\,\mathrm{cm}^{-2}$, pochodzący zarówno ze spontanicznej i piezoelektrycznej polaryzacji, jak i domieszkowania bariery AlGaN-owej atomami krzemu (donorami) na poziomie $2 \times 10^{18}\,\mathrm{cm}^{-3}$.

Właściwości transportowe naszych struktur zostały określone na podstawie dwukontaktowych pomiarów zależności oporu kanału tranzystora od pola magnetycznego, $R(B)$, przeprowadzonych w temperaturze 4,3 K – 8 K dla zadanej polaryzacji elektrycznej bramki ($V_g \leqslant 0$) oraz pola $\boldsymbol{B}$ (do 10 T) skierowanego prostopadle do płaszczyzny 2DEG. W celu prawidłowego wyznaczenia diagonalnych składowych tensora magnetooporności, podczas ich wykonywania, wzięto pod uwagę oba zwroty pseudowektora indukcji magnetycznej (równoległy i antyrównoległy do kierunku wzrostu heterostruktury). Analiza oscylacji Shubnikov'a-de Haas'a rozwijających się w wysokopolowej części krzywych $R(B)$ umożliwiła nam określenie koncentracji 2DEG (N) jako funkcji V_g jak również tak zwanego kwantowego czasu relaksacji, τ_q, dla $V_g = 0$. Zaobserwowaliśmy, że w próbkach charakteryzujących się większą szczeliną pomiędzy sąsiadującymi ze sobą paskami bramki, przyłożenie do sprzęgacza siatkowego napięcia $V_g < 0$ skutkowało wytworzeniem przestrzennej modulacji N, podczas gdy w tych z węższymi szczelinami, każdy segment bramki kontrolował N na długości całego okresu struktury. Minimalna odległość wymagana do pojawienia się dwóch populacji nośników ładunku o wyraźnie różnych koncentracjach była dla nas początkowo zaskoczeniem, albowiem przekraczała prawie czterokrotnie typowy dystans, jaki wynika z dyfuzji i efektu wnikania pola elektrycznego do przestrzeni poza konturem bramki (z ang. *electric-field-fringing effect*). Posiłkując się wnioskami płynącymi z niezależnych eksperymentów przeprowadzonych przez innych badaczy, opartych na skaningowej mikroskopii pojemnościowej oraz pomiarach fotoprądu indukowanego promieniowaniem UV, przypisujemy obecnie to zjawisko ładowaniu stanów powierzchniowych w barierze AlGaN-owej (zidentyfikowanych jako stany typu akceptorowego), które może prowadzić do rozszerzenia fizycznych wymiarów źródła potencjału elektrostatycznego nawet o 0,5 µm. Jak pokazano, taki mechanizm powinien być szczególnie efektywny w przypadku urządzeń charakteryzujących się znaczącymi prądami upływności bramki, co bardzo dobrze odpowiada strukturom badanym w ramach niniejszej rozprawy.

Nisko-polowa część wyników magnetotransportowych poddanych odpowiedniej symetryzacji pomogła nam w oszacowaniu zależącej od koncentracji ruchliwości elektronów oraz czasu relaksacji pędowej, τ_t. Nieoczekiwanie wysoka wartość stosunku $\tau_\mathrm{t}/\tau_\mathrm{q}$ dla $V_g = 0$, wynosząca dla różnych próbek od 25 do prawie 40 i związana częściowo z niejednorodnością warstwy 2DEG, której trudno uniknąć w przypadku kryształów o dużej powierzchni, również wskazała na obecność stanów powierzchniowych obsadzonych elektronami i działających jako źródło daleko-zasięgowego potencjału rozpraszającego.

W celu wyjaśnienia ogólnego kształtu krzywych $R(B)$ otrzymanych na próbkach ze sprzęgaczami siatkowymi proponujemy w niniejszej pracy model oparty na zjawisku spotęgowanego prądem upływności bramki geometrycznego magnetooporu, które wedle naszej wiedzy nie było do tej pory opublikowane. Jak pokazujemy, poddany skrupulatnej analizie bazującej na opisie zakrzywienia ścieżek prądowych metodą mapowania konforemnego, efekt ten może dać głęboki wgląd we właściwości badanego układu, umożliwiając na przykład wyznaczenie przestrzennego rozkładu gęstości prądu upływności bramki wzdłuż kanału tranzystora polowego. Określenie kształtu tego rozkładu okazało się być w naszym przypadku niezwykle ważne dla zrozumienia zadziwiająco słabej podatności modów magnetoplazmowych na napięcie przyłożone do bramki, jaką zaobserwowaliśmy na większości próbek będących przedmiotem badań tej rozprawy.

Optyczna część naszych pomiarów była oparta na dwóch typach uzupełniających się eksperymentów magnetotransmisyjnych. W ramach pierwszego z nich, badania obejmujące zakres spektralny od 0,6 THz do 15 THz zostały przeprowadzone w temperaturze 1,8 K z wykorzystaniem spektrometru Fourierowskiego sprzężonego z polem magnetycznym do 13 T. Dostarczyły one widm zarejestrowanych dla różnych wartości B i niespolaryzowanej intencjonalnie bramki. W przypadku drugiego eksperymentu, źródłem światła o częstotliwości 2,52 THz kierowanego na próbkę utrzymywaną w temperaturze 4,3 K – 8 K był pompowany optycznie laser dalekiej podczerwieni. Ze względu na stałą energię pobudzenia, sygnał transmisyjny był mierzony albo w funkcji B do 10 T przy zadanej wartości napięcia przyłożonego do bramki, albo też w zależności od V_g do -5 V dla $B = \text{const}$. Tak jak w trakcie wykonywania badań magnetotransportowych, w obu eksperymentach optycznych pole $\boldsymbol{B}$ było skierowane prostopadle do płaszczyzny 2DEG.

Wyraźne ślady wzbudzeń magnetoplazmowych zostały zaobserwowane w widmach transmisyjnych wszystkich próbek, na których zostały przeprowadzone pomiary. Wysoka jakość danych doświadczalnych, uzyskana między innymi dzięki zastosowaniu transformacji numerycznej znanej jako auto-dekonwolucja Fourierowska (z ang. *Fourier Self-Deconvolution*), pozwoliła na skonstruowanie diagramów dyspersyjnych zarejestrowanych modów oscylacji magnetoplazmowych. Po przeprowadzonej z ich pomocą analizie, okazało się, że punkty eksperymentalne oznaczające lokalne minima odpowiednich krzywych transmisyjnych, reprezentują bądź tzw. górne mody hybrydowe (z ang. *upper-hybrid modes*, UHM) powstające z fal plazmowych istniejących również w granicy $B \to 0$, bądź też mody odkryte na gruncie teoretycznym przez I. B. Bernsteina, które pojawiają się wyłącznie w poddanej wpływowi pola magnetycznego plazmie o przewodności zależącej tak od częstotliwości, jak i od wektora falowego. Wedle naszej wiedzy, nikomu przed nami nie udało się zaobserwować modów Bernsteina (BM) w strukturach półprzewodnikowych opartych na GaN/AlGaN.

W fizyce plazmy, mody te są uznawane za bezpośredni próbnik nielokalnych właściwości ośrodka, w którym propagują się z częstotliwościami bliskimi harmonicznym częstotliwościom rezonansu cyklotronowego. Ponieważ energia dowolnie wybranego BM rośnie z polem magnetycznym szybciej aniżeli energia UHM, dla pewnej wartości B mody te powinny stać się zdegenerowane. Taki scenariusz wykluczają jednak względy symetrii, za sprawą których, w rzeczywistości dochodzi między nimi do silnego oddziaływania, które na wspomnianych wyżej diagramach dyspersyjnych objawia się w postaci niedozwolonych przecięć (lub odpychania) pomiędzy krzywymi odpowiadającymi UHM i danemu BM. Poza obszarami oddziaływania, amplituda modów Bernsteina bardzo szybko osiąga na tyle małe wartości, że wyekstrahowanie ich z danych doświadczalnych staje się niezwykle trudnym zadaniem. Co więcej, mierzona w jednostkach energii odległość pomiędzy krzywymi dyspersyjnymi w granicach niedozwolonych przecięć maleje ze wzrostem rzędu BM. W konsekwencji, nie budzące żadnych wątpliwości dowody istnienia uzyskano do tej pory jedynie dla dwóch pierwszych modów Bernsteina zaobserwowanych na próbkach wykonanych z wysokiej jakości heterostruktur GaAs/AlGaAs (mamy w tym przypadku na myśli eksperymenty przeprowadzone w funkcji pola magnetycznego dla zadanej gęstości powierzchniowej 2DEG). Pomimo znacznie gorszych parametrów 2DEG, otrzymaliśmy dokładnie te same rezultaty na strukturach GaN/AlGaN, co wyraźnie pokazuje ich potencjał w konkurowaniu z układami opartymi na GaAs również w dziedzinie badań podstawowych materii skondensowanej. Warto zwrócić także uwagę na fakt, że dzięki bogatym widmom złożonym z wielu rezonansów magnetoplazmowych (o częstościach dochodzących włącznie do 10 harmonicznej fundamentalnej częstości plazmowej określonej przez najdłuższy wektor falowy odpowiadający okresowi sprzęgacza siatkowego) byliśmy w stanie dokonać weryfikacji istniejącej teorii półklasycznej, która opisuje wzbudzenie magnetoplazmowe, w stopniu, jaki nie był osiągalny we wcześniejszych badaniach podjętych z pomocą struktur GaAs/AlGaAs.

Układ niniejszej rozprawy przedstawia się następująco. Jest ona złożona z dwóch części zatytułowanych „Rozważania teoretyczne" i „Wyniki eksperymentalne". Każda z nich obejmuje dwa rozdziały. W rozdziale pierwszym, konstruujemy systematycznie opis oscylacji dwuwymiarowej plazmy poddanej wpływowi pola magnetycznego, poczynając od przypadku gazu swobodnych elektronów i przechodząc stopniowo do coraz bardziej złożonych struktur półprzewodnikowych. W rozdziale drugim, przypominamy krótko podstawy wybranych zjawisk magnetotransportowych występujących zarówno w niskich jak i wysokich polach magnetycznych. Naszym głównym celem jest w tym przypadku zebranie wszystkich wyrażeń, jakie są potrzebne do zrozumienia szczegółów opracowania i interpretacji danych eksperymentalnych zaprezentowanych w drugiej części pracy. Rozdział trzeci zawiera dyskusję na temat ogólnych właściwości sprzęgaczy siatkowych, jak również dostarcza wyczerpujących informacji odnośnie badanych próbek GaN/AlGaN. W rozdziale czwartym opisujemy szeroko zarówno techniki doświadczalne jak i wyniki pomiarów magnetotransportowych i magnetooptycznych, które są następnie poddane interpretacji z wykorzystaniem modeli teoretycznych rozwiniętych w rozdziałach pierwszym i drugim. Pracę zamyka krótkie podsumowanie wszystkich najważniejszych rezultatów, które zostały w niej ogłoszone.

Abstract

Gallium nitride (GaN) is nowadays one of the most important semiconductors, especially from the point of view of high-temperature and high-frequency applications in the fields of high-speed electronics, optoelectronics and blue, violet as well as ultraviolet optics. Concerning basic research, however, focused on fundamental phenomena that can be explored in III-V semiconductor structures, it still remains in the background of gallium-arsenide-based systems. It is particularly true for collective excitations of a two-dimensional electron gas (2DEG). An important class of these excitations are charge-density oscillations, usually referred to as plasma oscillations or plasma waves in order to emphasize the fact that at sufficiently low temperature, a 2DEG of high density acquires all the features which underlie the definition of plasma - one of the four fundamental states of matter. In the presence of an external magnetic field (B), plasma waves become a powerful tool to probe the non-local properties of a 2DEG, which to the best knowledge of the author have not yet been systematically investigated in GaN-based systems. The main goal of the following dissertation was therefore to at least partially fill this gap by analysing the influence of the non-local effects on the spectrum of two-dimensional magnetoplasma excitations in GaN/AlGaN heterostructures.

The samples under study were large-area (about 1.6 mm × 1.6 mm) field-effect transistors (FETs) with grating-gate electrodes of different periodicity (L) and width of an individual metallic gate's stripe (W). We have considered four transistor structures with L ranging from $2.0\,\mu\mathrm{m}$ to $4.0\,\mu\mathrm{m}$ and a separation between the adjacent gate's fingers ($S = L - W$) equal either to $0.35\,\mu\mathrm{m}$ or to $0.85\,\mu\mathrm{m}$. A primary role of the gratings was to ensure an optical coupling between the 2DEG magnetoplasmons and the incoming electromagnetic radiation. When electrically polarized, they additionally served to control the concentration of a 2DEG in the FET's channel. We also had at our disposal a reference sample of exactly the same dimensions as grating FETs, but with no gate electrode deposited on its top surface. All the samples were processed on a high-quality GaN/AlGaN heterostructure grown Ga-face up on a sapphire substrate by Migration-Enhanced Metal-Organic Chemical Vapor Deposition technique. Each of them contained a quasi-2DEG of areal density $N_0 \sim 10^{13}\,\mathrm{cm}^{-2}$, originating from both the spontaneous and piezoelectric polarization as well as doping of AlGaN barrier with silicon donors to approximately $2 \times 10^{18}\,\mathrm{cm}^{-3}$.

The electrical-transport properties of our structures were determined from two-terminal measurements of the magnetic-field dependence of the channel resistance, $R(B)$, recorded at 4.3–8 K for a given polarization of the gate electrode ($V_g \leqslant 0$) and the $\boldsymbol{B}$ field up to 10 T applied perpendicularly to the plane of a 2DEG. Both orientations of the magnetic field (parallel and anti-parallel to the heterostructure's growth

direction) were considered in order to correctly extract the diagonal part of the magnetoresistivity tensor from the experimental data. An analysis of the Shubnikov-de Haas oscillations, developing in a high-field part of $R(B)$ traces, enabled us to estimate the 2DEG density (N) as a function of V_g as well as the so-called electron quantum relaxation time, τ_q, for $V_g = 0$. We found out that in FETs with a larger slit between the adjacent grating-gate's fingers, an application of $V_g < 0$ resulted in creating a lateral modulation of N, whereas for a narrower slit, each section of the gate controlled N in the entire period of the structure. A minimal distance, required to observe two populations of carriers with clearly different densities, was initially a bit surprising to us, since it exceeded a typical range resulting from the electric-field-fringing effect and diffusion by almost four times. Following the conclusions from independent experiments performed by other researchers (scanning capacitance microscopy, UV-light-induced persistent photocurrent measurements) we now attribute this phenomenon to charging the surface states on top of the AlGaN barrier (proven to be of acceptor-like type), which can extend the physical dimensions of the source of electrostatic potential by even a 0.5 µm. Such a mechanism was shown to be especially efficient in devices that exhibit substantial gate-leakage currents, what fits very well the structures studied in this dissertation.

A low-magnetic-field part of the properly symmetrized magnetoresistance data helped us to estimate an N-dependent mobility and momentum relaxation time, τ_t. An unexpectedly high $\tau_\mathrm{t}/\tau_\mathrm{q}$ ratio at $V_g = 0$, varying from sample to sample from 25 to almost 40 and partially originating from the inhomogeneity of the 2DEG layer, which is hard to avoid in large-area crystals, also confirmed the presence of surface states occupied by electrons and acting as a source of the long-range scattering potential.

In order to explain the general shape of $R(B)$ curves recorded on the grating-gate structures we propose a model based on the gate-leakage-current-enhanced geometrical magnetoresistance - an effect, which to the best knowledge of the author, has not yet been reported in the literature. We show, that when accurately analysed (with the aid of a conformal mapping description of the current-path distortion), it can give a very deep insight into the measured system, offering, for instance, the possibility of determining the spatial distribution of the gate-leakage current density along the FET's channel. In our case, estimating the shape of this distribution turned out to be very important for understanding a surprisingly weak susceptibility to the gate voltage that was exhibited by magnetoplasmon modes in most of the samples under investigation.

The optical part of our research was based on two complementary magnetotransmission experiments. In the first one, transmission measurements covering the spectral range from 0.6 THz to 15 THz were carried out at 1.8 K with the use of a Fourier transform infrared spectrometer coupled with the magnetic field up to 13 T. Spectra were recorded for different values of B and floating gate potential. In the second experiment, an optically pumped far-infrared laser was utilized to shine a 2.52 THz radiation on a sample kept at 4.3–8 K. Due to the constant energy of excitation, a transmission signal was registered either as a function of B up to 10 T with V_g set to a given value or V_g down to -5 V, but for $B = \text{const}$. As in the case of magneto-transport characterization, also in both optical experiments the $\boldsymbol{B}$ field was directed perpendicularly to the plane of a 2DEG.

Clear evidence of magnetoplasmon resonances were found in transmission spectra collected for all the samples under study. The quality of experimental data improved, if necessary, by means of a numerical transformation known as Fourier Self-Deconvolution, enabled us to construct the B-field dispersion diagrams of the recorded modes of magnetoplasma oscillations. When analysed in such diagrams, the experimental points denoting the minima in respective transmission curves turned out to represent either a so-called upper-hybrid mode (UHM), which originates from plasma waves that exist also for $B = 0$, or the modes discovered on a theoretical basis by I. B. Bernstein, which appear only in magnetized plasmas of frequency- and wave-vector-dependent conductivity. Up to the best knowledge of the author, it is the first time, when observation of these modes is reported for the GaN/AlGaN-based structures. In plasma physics, Bernstein modes (BMs) are recognized as a direct probe of the non-local properties of the medium through which they propagate at frequencies close to the harmonics of the cyclotron resonance frequency. Since the energy of any given BM increases with the magnetic field faster than the energy of the UHM, there are values of B at which these two modes should become degenerate. Such a scenario is not, however, allowed by the symmetry rules and what happens instead is the mode-mixing, which in the B-field dispersion diagram appears as an anti-crossing (or repulsion) between curves corresponding to the UHM and a given BM. Apart from these interaction regions, the amplitudes of BMs are very small, so that extracting them from experimental data becomes a challenging task. Furthermore, the anti-crossings get smaller as the order of BM increases. In consequence, the undeniable traces of only the first two BMs excited in solid state plasmas have been reported so far for high-quality GaAs/AlGaAs samples (concerning the experiments performed as a function of the magnetic field for a given value of the 2DEG density). In spite of much worse parameters of a 2DEG, we have obtained the same results in the GaN/AlGaN structures, what demonstrates their potential for competing with the GaAs-based systems also in the field of basic research in condensed matter physics. Moreover, thanks to rich spectra, composed of many magnetoplasmon modes (up to 10th harmonics of the fundamental frequency corresponding to the longest wave vector allowed by the grating coupler) we were able to examine the existing semi-classical theory of magnetoplasma excitations to the extent, which was unattainable in the previous studies carried on with the help of GaAs/AlGaAs samples.

The organisation of the thesis is the following. It is composed of two parts entitled 'Theoretical considerations' and 'Experimental results'. Each of them contains two chapters. In Chapter 1, we systematically develop the description of two-dimensional magnetoplasma oscillations, starting from the case of a free electron gas and progressively moving towards more and more complex semiconductor structures. In Chapter 2, the fundamentals of relevant magnetotransport phenomena, occurring both at low and high magnetic fields, are briefly reminded with a special emphasis placed on collecting all the expressions used to process and interpret the experimental data presented in the second part of this dissertation. Chapter 3 contains a discussion of general properties of the grating-couplers as well as provides the details of grating-gate GaN/AlGaN transistor structures under investigation. In Chapter 4, the experimental techniques and the results of our magnetotransport and magnetooptical measurements are widely described and interpreted with the aid of theoretical concepts introduced in Chapters 1 and 2. Finally, we briefly summarize the thesis listing once again the most important results it announces.

Conference presentations and publications

The results of investigations discussed in this dissertation gave rise to the following conference presentations:

1. ***Analysis of Bernstein Modes in GaN/AlGaN Heterostructures*** by K. Nogajewski, M. Orlita, A. Witowski, F. Teppe, W. Knap, M. Potemski, M. Shur, and J. Łusakowski presented in an **oral form** (by J. Łusakowski) at the *OTST 2013 International Workshop on Optical Terahertz Science and Technology, April 1-5, 2013, Kyoto Terrsa, Japan*;

2. ***Bernstein modes in grating-coupled two-dimensional electron gas in GaN/AlGaN heterostructures*** by K. Nogajewski, M. Orlita, A. Witowski, F. Teppe, W. Knap, M. Potemski, M. Shur, and J. Łusakowski presented in an **oral form** at the *31st International Conference on the Physics of Semiconductors, July 29 - August 3, 2012, ETH Zurich, Zurich, Switzerland*;

3. ***Photocurrent studies of laterally modulated two-dimensional electron gas in GaN/AlGaN heterostructures*** by K. Nogajewski, K. Karpierz, M. Grynberg, W. Knap, R. Gaska, J. Yang, M. S. Shur, and J. Łusakowski presented as a **poster** (by. K. Karpierz) at the *20th International Conference on "High Magnetic Fields in Semiconductor Physics", July 22 - 27, 2012, Chamonix Mont-Blanc, France*;

4. ***Non-local Properties of Two-Dimensional Electron Gas in GaN/AlGaN Heterostructures*** by K. Nogajewski, M. Orlita, A. Witowski, F. Teppe, W. Knap, M. Potemski, M. Shur, K. Karpierz, M. Grynberg and J. Łusakowski presented in an **oral form** at the *41st "Jaszowiec" International School & Conference on the Physics of Semiconductors, June 8 - 15, 2012, Krynica-Zdrój, Poland*;

5. **invited talk** entitled: ***THz excitations of GaN/AlGaN structures*** by K. Nogajewski, and J. Łusakowski given at the *1st International Symposium on Terahertz Nanoscience and 2nd Workshop of International Terahertz Research Network (GDR-I), November 24 - 29, 2011, Nakanoshima Center, Osaka University, Osaka, Japan*;

6. ***Magnetooptical studies of resonant plasma excitations in grating-gate GaN/AlGaN-based field-effect transistors*** by K. Nogajewski, K. Karpierz, M. Grynberg, W. Knap, R. Gaska, J. Yang, M. S. Shur, and

J. Łusakowski presented in an **oral form** at the *36th International Conference on Infrared, Millimeter, and Terahertz Waves, October 2 - 7, 2011, Hyatt Regency Downtown, Houston, Texas, USA*;

7. ***Magnetotransport properties of grating-gate THz detectors based on high electron mobility GaN/AlGaN heterostructures*** by K. Nogajewski, K. Karpierz, M. Grynberg, W. Knap, R. Gaska, J. Yang, M. S. Shur, and J. Łusakowski presented in an **oral form** at the *36th International Conference on Infrared, Millimeter, and Terahertz Waves, October 2 - 7, 2011, Hyatt Regency Downtown, Houston, Texas, USA*;

8. ***Resonant Terahertz Absorption by Magnetoplasmons in Grating-Gate GaN/AlGaN-based Field-Effect Transistors*** by K. Nogajewski, K. Karpierz, M. Grynberg, W. Knap, R. Gaska, J. Yang, M. S. Shur, and J. Łusakowski presented in an **oral form** at the *40th "Jaszowiec" 2011 International School & Conference on the Physics of Semiconductors, June 25 - July 1, 2011, Krynica-Zdrój, Poland.*

Some of them have also been published in the following papers:

1. K. Nogajewski, J. Łusakowski, W. Knap, V. V. Popov, F. Teppe S. L. Rumyantsev, and M. S. Shur, *"Localized and collective magnetoplasmon excitations in AlGaN/GaN-based grating-gate terahertz modulators"*, *Applied Physics Letters* **99**, 213501 (2011),

2. K. Nogajewski, K. Karpierz, M. Grynberg, W. Knap, R. Gaska, J. Yang, M. S. Shur, and J. Łusakowski, *"Magnetooptical studies of resonant plasma excitations in grating-gate GaN/AlGaN-based field-effect transistors"*, *36th International Conference on Infrared, Millimeter and Terahertz Waves* (*IRMMW-THz 2011, IEEE conference proceedings*), 6105195 (2011),

3. K. Nogajewski, K. Karpierz, M. Grynberg, W. Knap, R. Gaska, J. Yang, M. S. Shur, and J. Łusakowski, *"Magnetotransport properties of grating-gate THz detectors based on high electron mobility GaN/AlGaN heterostructures"*, *36th International Conference on Infrared, Millimeter and Terahertz Waves* (*IRMMW-THz 2011, IEEE conference proceedings*), 6104919 (2011).

Two comprehensive publications concerning the main results of both the magnetooptical and magnetotransport studies are now under preparation and will be submitted soon.

Contents

Part I

Theoretical considerations

Chapter 1

Description of magnetoplasmon excitations

The major goal of this chapter is to find the dispersion relation for the charge density oscillations in a two-dimensional electron gas (2DEG) subject to the external, static magnetic field and a time- and space-dependent electric field. In order to do so, we first derive the relevant magnetoconductivity tensor which is next combined with the solution of Maxwell's equations with appropriate boundary conditions. In our analysis we go beyond the local approximation for the spatial variation of the electric field, what means that we do not assume any particular constraint on its wavelength, except for the requirement that it should be large enough to treat the medium containing an electron gas as homogeneous, but smaller than the size of the sample in order to neglect the boundary effects. The magnetic field is supposed to be applied perpendicularly to the plane of 2DEG and the system is treated as a cold, degenerate plasma composed of non-interacting electrons. Neglecting the electron-electron interaction might seem to be a substantial constriction, but most of salient features of the experiments performed on solid-state plasmas over the last thirty years, have been almost perfectly reproduced by the free-electron model. Moreover, its main results are identical with those obtained within the framework of the so-called random-phase approximation [1, 2], which takes into account the Coulomb interaction between electrons in the form of self-consistent electric field. Initially, the presence of a crystal lattice (dielectric surrounding) is included in our calculations as a dispersionless static dielectric constant, but at the final stage we switch to description based on the full dynamic dielectric function relevant to more complex semiconductor structures. The plasmon-LO phonon coupling, which plays an important role in polar semiconductors, is also discussed and incorporated into the final results.

Although our aim is to describe low-energy excitations of a 2DEG, we first discuss in detail the case of a three-dimensional electron gas (3DEG). There are two important reasons for that. Firstly, the procedures of deriving the three- and two-dimensional magnetoconductivity tensors are almost identical, but the 3D case is more general. Hence, it is natural to develop the description for this case first and then only change the details that are related to dimensionality of the system. Secondly, in the literature on the subject one can find quite recent papers in which, for instance, a theoretical treatment formulated for a 3DEG is incorrectly used to interpret experiments performed on samples containing a 2DEG [3]. Therefore, in order to avoid any ambiguity and misunderstanding, we discuss both cases pointing out all the important differences between them as well as explaining why under certain conditions they provide almost identical, quantitative estimations for the relevant parameters.

Our approach involving a self-consistent solution of Boltzmann's [4] and Maxwell's [5, 6] equations is a semi-classical one. Purely quantum-mechanical effects, which may give rise, for instance, to the oscillating behaviour of the electronic polarizability when the electron gas is subject to the magnetic field [7, 8], are not analysed. When constructing subsequent elements of the model describing the magnetoplasmon excitations, we make several important assumptions. First of all, we restrict ourselves to a linear response of the medium containing an electron gas to the external electromagnetic field. This imposes a significant limitation on the field's strength/magnitude - it has to be small enough to treat the interaction of the field with electrons as a small perturbation. Secondly, in the three-dimensional case we suppose the conduction band to be a single-valley, isotropic and parabolic, what means that it can be characterized by a scalar effective mass. Similar assumptions are also made about the lowest-lying subband in a triangular quantum well, confining the electron gas to the interface between two layers of semiconductors with different energy gaps. As stated earlier, we suppose that only this subband is partially filled with electrons and we neglect any contribution to the electronic polarizability coming from interband transitions. Finally, along with the electron-electron interaction we also disregard in our derivation the exchange and correlation effects between electrons [9] as well as the so-called local field corrections [10, 11], which in general can affect the magnetoplasmon dispersion relation, but their net influence is expected to be small (on the level of a few percent of the resonant energy value).

In the presented analysis we closely follow the procedure given by M. H. Cohen and co-workers [12], which utilizes the method of solving the Boltzmann equation proposed by R. G. Chambers [13, 14]. The same approach was also used in the work of A. V. Chaplik and D. Heitmann [15]. When deriving the dispersion relation for two-dimensional magnetoplasmons, we proceed similarly to K. W. Chiu and J. J. Quinn [8]. Besides recalling the final results, our objective is to demonstrate the intermediate steps of calculation which were omitted in the original papers. Passing through them is very important not only for a deeper understanding of the model itself, but also for its generalization to more complex semiconductor structures.

1.1 The Boltzmann equation

The Boltzmann equation deals with a time evolution of a distribution function $f(\mathbf{r}, \boldsymbol{v}, t)$ describing at a certain time t the density of carriers located in the infinitesimal volume around a given point $\mathbf{r}$ in the real space and moving with velocities contained in the infinitesimal range about $\boldsymbol{v}$. According to Liouville's theorem [16, 17], for the phase space of fixed volume, the total concentration of particles

$$N = \frac{2m^3}{h^3} \int \mathrm{d}\mathbf{r} \int \mathrm{d}\boldsymbol{v} f(\mathbf{r}, \boldsymbol{v}, t) \tag{1.1}$$

remains constant. In the above expression, the prefactor represents the density of states of a three-dimensional Fermi gas, h is the Planck constant, m denotes the particle mass, 2 stands for the number of possible orientations of the particle's spin and the integration extends over the whole phase space under consideration. At a particular point $(\mathbf{r}, \boldsymbol{v})$ the distribution function $f(\mathbf{r}, \boldsymbol{v}, t)$ may change due to various effects. Restricting our analysis to small, linear variations with time and assuming that there is no temperature gradient in the volume of a Fermi gas under study, we can write:

$$\begin{aligned} f(\mathbf{r}, \boldsymbol{v}, t) &= f(\mathbf{r} - \boldsymbol{v}\Delta t, \boldsymbol{v} - \mathbf{a}\Delta t, t - \Delta t), & (1.2) \\ &= f(\mathbf{r}, \boldsymbol{v}, t) - \Delta t\,(\boldsymbol{v} \cdot \nabla_{\mathbf{r}} f) - \Delta t\,(\mathbf{a} \cdot \nabla_{\boldsymbol{v}} f) - \Delta t \frac{\partial f}{\partial t}, & (1.3) \end{aligned}$$

where the second term in Eq. (1.3) indicates the change of the particle density due to diffusion and the third one is related to the external force imparting to the particles an acceleration $\mathbf{a}$. Collisions between particles (in the case of electrons in a crystal lattice also collisions with impurities and interaction with phonons) may alter the distribution function as well. They force a given particle to undergo a transition from the state characterized by the velocity $\boldsymbol{v}$ to unoccupied state of velocity $\boldsymbol{v}'$. Taking into account that this process can also proceed in the opposite direction and assuming microscopic reversibility for the transition probability $\Lambda(\boldsymbol{v}, \boldsymbol{v}')$ between states $|\boldsymbol{v}\rangle$ and $|\boldsymbol{v}'\rangle$, i.e. $\Lambda(\boldsymbol{v}, \boldsymbol{v}') = \Lambda(\boldsymbol{v}', \boldsymbol{v})$, we can express the collision contribution to the time derivative of a distribution function as:

$$\begin{aligned} \left.\frac{\partial f}{\partial t}\right)_{\text{coll.}} &= \int \left[f(\boldsymbol{v}')\,(1 - f(\boldsymbol{v})) - f(\boldsymbol{v})\,(1 - f(\boldsymbol{v}'))\right] \Lambda(\boldsymbol{v}, \boldsymbol{v}')\mathrm{d}\boldsymbol{v}' & (1.4) \\ &= \int \left[f(\boldsymbol{v}') - f(\boldsymbol{v})\right] \Lambda(\boldsymbol{v}, \boldsymbol{v}')\mathrm{d}\boldsymbol{v}' & (1.5) \end{aligned}$$

where for the sake of clarity we have omitted the explicit indication of $\mathbf{r}$- and t-dependence of $f(\mathbf{r}, \boldsymbol{v}, t)$. Combining this equation with a slightly rearranged Eq. (1.3) yields the linearized Boltzmann equation:

$$\frac{\partial f}{\partial t} + \boldsymbol{v} \cdot \nabla_{\mathbf{r}} f + \mathbf{a} \cdot \nabla_{\boldsymbol{v}} f = \left.\frac{\partial f}{\partial t}\right)_{\text{coll.}} . \tag{1.6}$$

Scattering events are usually considered as processes counterbalancing an external perturbation causing the drift of particles. Therefore, the collision term stands on the right-hand side of Eq. (1.6).

1.2 Magnetoconductivity tensor

1.2.1 Three-dimensional electron gas

Our next objective is to solve the Boltzmann equation for a 3DEG subject to an external, static magnetic field $\mathbf{B} = [0, 0, B]$ and a time- and space-dependent electric field $\mathbf{E}(\mathbf{r}, t)$. We want to derive a non-local magnetoconductivity tensor $\hat{\sigma}(\mathbf{r}, \mathbf{r}', t, t', \mathbf{B})$ establishing at a certain time t a relationship between the total electric field $\mathbf{E}(\mathbf{r}, t)$ and the total current density $\mathbf{J}(\mathbf{r}, t, \mathbf{B})$ induced by it at position $\mathbf{r}$:

$$\mathbf{J}(\mathbf{r}, t, \mathbf{B}) = \int\int \hat{\sigma}(\mathbf{r}, \mathbf{r}', t, t', \mathbf{B}) \mathbf{E}(\mathbf{r}', t') \mathrm{d}t' \mathrm{d}\mathbf{r}'. \tag{1.7}$$

'Total' means that we take into account both the external currents (electric fields) and the currents (electric fields) that appear as a response to the external ones [5, 6]. In what follows we will be dealing only with homogeneous media, and thus

$$\hat{\sigma}(\mathbf{r}, \mathbf{r}', t, t', \mathbf{B}) = \hat{\sigma}(\mathbf{r} - \mathbf{r}', t - t', \mathbf{B}).$$

Furthermore, we will assume a spatial and temporal variation of the electric field in the form:

$$\mathbf{E}(\mathbf{r}, t) = \mathbf{E}_0(\mathbf{q}, \omega) \exp\left[i(\mathbf{q} \cdot \mathbf{r} - \omega t)\right], \tag{1.8}$$

where $\mathbf{q}$ and ω are the wave vector and the frequency of a plane wave, respectively. Then, by Fourier transform [18] of Eq. (1.7) it is straightforward to show that

$$\mathbf{J}(\mathbf{q}, \omega, \mathbf{B}) = \hat{\sigma}(\mathbf{q}, \omega, \mathbf{B}) \mathbf{E}(\mathbf{q}, \omega). \tag{1.9}$$

With the aid of Maxwell's equations [6], the magnetoconductivity tensor of a free electron gas can be related to the dielectric tensor $\hat{\varepsilon}(\mathbf{q}, \omega, \mathbf{B})$ and the electronic polarizability tensor $\hat{\chi}(\mathbf{q}, \omega, \mathbf{B})$:

$$\hat{\varepsilon}(\mathbf{q}, \omega, \mathbf{B}) = \mathbb{I} + \frac{i\hat{\sigma}(\mathbf{q}, \omega, \mathbf{B})}{\omega \varepsilon_0} = \mathbb{I} + \frac{1}{\varepsilon_0} \hat{\chi}(\mathbf{q}, \omega, \mathbf{B}), \tag{1.10}$$

where ε_0 is the permittivity of the free space and $\mathbb{I}$ denotes the unit matrix. This means that Eq. (1.9) can equally well be expressed as:

$$\mathbf{J}(\mathbf{q},\omega,\mathbf{B}) = -i\omega\hat{\chi}(\mathbf{q},\omega,\mathbf{B})\mathbf{E}(\mathbf{q},\omega). \tag{1.11}$$

Now we need to return to the Boltzmann equation, which in the simultaneous presence of the magnetic and electric field takes on the form:

$$\frac{\partial f}{\partial t} + \boldsymbol{v}\cdot\nabla_{\mathbf{r}} f - \frac{e}{m}\left(\mathbf{E} + \boldsymbol{v}\times\mathbf{B}\right)\cdot\nabla_{\boldsymbol{v}} f = \left.\frac{\partial f}{\partial t}\right)_{\text{coll.}} \tag{1.12}$$

with m representing the electron mass, $-e$ being the electronic charge and the Lorentz force as a source of electrons' acceleration $\mathbf{a}$. In order to solve it, we make the relaxation time approximation for the collision term standing on the right-hand side:

$$\left.\frac{\partial f}{\partial t}\right)_{\text{coll.}} = -\frac{f - f_0}{\tau}, \tag{1.13}$$

where τ is the momentum relaxation time and f_0 denotes the unperturbed electron distribution function which we take to be the thermal equilibrium Fermi-Dirac function [17]:

$$f_0(E) = \frac{1}{\exp\left(\frac{E-E_F}{k_B T}\right) + 1}. \tag{1.14}$$

In the above expression: E_F, k_B and T represent the Fermi energy, the Boltzmann constant and the temperature, respectively. In the case of a free electron gas, E is simply equal to the kinetic energy: $E = mv^2/2$. The meaning of Eq. (1.13) is that due to collisions $f(\mathbf{r},\boldsymbol{v})/\tau$ electrons are scattered out of a unit volume of the phase space around a given point $(\mathbf{r},\boldsymbol{v})$ in a unit time and $f_0(\mathbf{r},\boldsymbol{v})/\tau$ are scattered in. Next we assume that the electron system under consideration is weakly perturbed by the applied fields, so that distribution functions f and f_0 differ one from the other by only a small value δf. We also make the following observation [13, 14]. Imagine an electron that travels along a given trajectory T_1 in the phase space (see Fig. 1.1) and after reaching an arbitrarily chosen point $(\mathbf{r}',\boldsymbol{v}'')$ at a time t' scatters onto the trajectory T_2 with some probability $\Lambda(\boldsymbol{v}'',\boldsymbol{v}')$ of changing the state from $|\boldsymbol{v}''\rangle$ to $|\boldsymbol{v}'\rangle$. If in the next step this

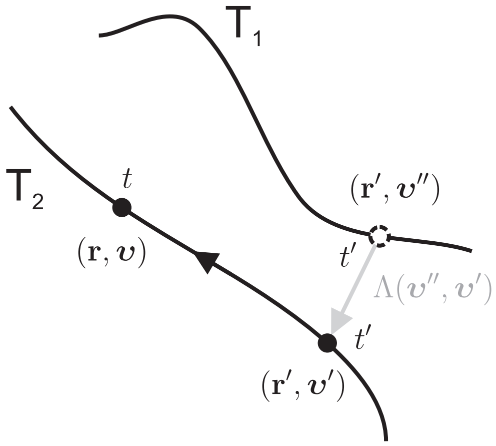

Figure 1.1: Schematic illustration of two trajectories: T_1 and T_2 in the phase space. An electron that has initially been moving along the trajectory T_1 reaches at a certain time t' the point $(\mathbf{r}',\boldsymbol{v}'')$ and scatters onto the trajectory T_2 with some probability $\Lambda(\boldsymbol{v}'',\boldsymbol{v}')$ of changing the state from $|\boldsymbol{v}''\rangle$ to $|\boldsymbol{v}'\rangle$. Next it follows the trajectory T_2 and at a time t arrives without any collision at the point $(\mathbf{r},\boldsymbol{v})$.

electron is supposed to contribute to the distribution function $f(\mathbf{r},\boldsymbol{v},t)$ at a certain point $(\mathbf{r},\boldsymbol{v})$ and time t, it must not leave the trajectory T_2 until arriving at this point after time $t-t'$. According to our assumption about the relaxation time, the probability of such a scenario is equal to $\exp(-(t-t')/\tau)$. Thus, in order to evaluate the distribution function $f(\mathbf{r},\boldsymbol{v},t)$ we have to integrate the number of electrons scattered onto the trajectory passing through the point $(\mathbf{r},\boldsymbol{v})$ at time t (governed by $f_0\mathrm{d}t/\tau$ as discussed on the previous page[1]), taking into account all times earlier than t, the energy $\Delta E(\mathbf{r},\mathbf{r}',\boldsymbol{v},\boldsymbol{v}',t-t')$ acquired by electrons from the applied fields when travelling from $\mathbf{r}'$ to $\mathbf{r}$ and the probability factor mentioned above[2]:

$$f(\mathbf{r},\boldsymbol{v},t)=\int_{-\infty}^{t} f_0(E-\Delta E(\mathbf{r},\mathbf{r}',\boldsymbol{v},\boldsymbol{v}',t-t'))\exp\left(-\frac{t-t'}{\tau}\right)\frac{\mathrm{d}t'}{\tau}. \tag{1.15}$$

With the use of expansion:

$$f_0(E-\Delta E(\mathbf{r},\mathbf{r}',\boldsymbol{v},\boldsymbol{v}',t-t'))=f_0(E)-\Delta E(\mathbf{r},\mathbf{r}',\boldsymbol{v},\boldsymbol{v}',t-t')\frac{\mathrm{d}f_0}{\mathrm{d}E}$$

and integration by parts this expression can be rewritten in the form:

$$\begin{aligned}
f(\mathbf{r},\boldsymbol{v},t)&=\int_{-\infty}^{t}\left[f_0(E)-\Delta E(\mathbf{r},\mathbf{r}',\boldsymbol{v},\boldsymbol{v}',t-t')\frac{\mathrm{d}f_0}{\mathrm{d}E}\right]\exp\left(-\frac{t-t'}{\tau}\right)\frac{\mathrm{d}t'}{\tau}\\
&=f_0(E)-\frac{\mathrm{d}f_0}{\mathrm{d}E}\left[\Delta E(\mathbf{r},\mathbf{r}',\boldsymbol{v},\boldsymbol{v}',t-t')\exp\left(-\frac{t-t'}{\tau}\right)\right]\Bigg|_{-\infty}^{t}\\
&\quad+\frac{\mathrm{d}f_0}{\mathrm{d}E}\int_{-\infty}^{t}\frac{\partial(\Delta E(\mathbf{r},\mathbf{r}',\boldsymbol{v},\boldsymbol{v}',t-t'))}{\partial t'}\exp\left(-\frac{t-t'}{\tau}\right)\mathrm{d}t'\\
&=f_0(E)+\frac{\mathrm{d}f_0}{\mathrm{d}E}\int_{-\infty}^{t}\frac{\partial(\Delta E(\mathbf{r},\mathbf{r}',\boldsymbol{v},\boldsymbol{v}',t-t'))}{\partial t'}\exp\left(-\frac{t-t'}{\tau}\right)\mathrm{d}t',
\end{aligned} \tag{1.16}$$

where marked in blue term vanishes in both limits, since for $t'\to-\infty$ the exponential factor goes to 0 and for $t'=t$ the electron acquires no energy from the applied fields ($\Delta E(\mathbf{r},\boldsymbol{v},0)=0$). Finally, noticing that $\delta f(\mathbf{r},\boldsymbol{v},t)=f(\mathbf{r},\boldsymbol{v},t)-f_0(E)$ we get:

$$\delta f(\mathbf{r},\boldsymbol{v},t)=\frac{\mathrm{d}f_0}{\mathrm{d}E}\int_{-\infty}^{t}\frac{\partial(\Delta E(\mathbf{r},\mathbf{r}',\boldsymbol{v},\boldsymbol{v}',t-t'))}{\partial t'}\exp\left(-\frac{t-t'}{\tau}\right)\mathrm{d}t'. \tag{1.17}$$

If the change of energy of electrons is due to the Lorentz force, it can be expressed as:

$$\Delta E(\mathbf{r},\mathbf{r}',\boldsymbol{v},\boldsymbol{v}',t-t')=-e\int_{t'}^{t}\left[\mathbf{E}(\mathbf{r}'',t'')+\boldsymbol{v}''\times\mathbf{B}\right]\cdot\boldsymbol{v}''\mathrm{d}t''=-e\int_{t'}^{t}\mathbf{E}(\mathbf{r}'',t'')\cdot\boldsymbol{v}''\mathrm{d}t'', \tag{1.18}$$

---

[1] The electrons scattered out of the analysed trajectory before reaching the point $(\mathbf{r},\boldsymbol{v})$ at the time t, which number is governed by $-f\mathrm{d}t/\tau$, are unimportant unless they return onto this trajectory at some time $t'<t$. Then, however, a time-variation of their number will be described once again by $f_0\mathrm{d}t/\tau$ and not by $-f\mathrm{d}t/\tau$. This is the reason for f_0/τ to appear under the integral sign in Eq. (1.15) instead of f/τ, as one would expect without more detailed analysis.

[2] In the following we make an extensive use of the abbreviated notation: $\mathbf{r}'\equiv\mathbf{r}(t')$ and $\boldsymbol{v}'\equiv\boldsymbol{v}(t')$.

what means that according to the Leibniz integral rule [19]:

$$\frac{\partial(\Delta E(\mathbf{r},\mathbf{r}',\boldsymbol{v},\boldsymbol{v}',t-t'))}{\partial t'} = e\mathbf{E}(\mathbf{r}',t')\cdot\boldsymbol{v}', \tag{1.19}$$

and thus, Eq. (1.17) becomes:

$$\delta f(\mathbf{r},\boldsymbol{v},t) = e\left(\frac{\mathrm{d}f_0}{\mathrm{d}E}\right)\int_{-\infty}^{t}\mathbf{E}(\mathbf{r}',t')\cdot\boldsymbol{v}'\exp\left(-\frac{t-t'}{\tau}\right)\mathrm{d}t'. \tag{1.20}$$

Having derived the correction $\delta f(\mathbf{r},\boldsymbol{v},t)$ to the equilibrium distribution function $f_0(E)$,[3] it is a straightforward task to write down the expression for the total current density appearing at a given point $\mathbf{r}$ and at a certain time t in the volume of an electron gas under analysis:

$$\mathbf{J}(\mathbf{r},t) = -\frac{2m^3}{h^3}e\int\boldsymbol{v}\delta f(\mathbf{r},\boldsymbol{v},t)\mathrm{d}\boldsymbol{v}. \tag{1.21}$$

Combining Eqs. (1.20) and (1.21) yields:

$$\mathbf{J}(\mathbf{r},t) = -\frac{2m^3e^2}{h^3}\int\mathrm{d}\boldsymbol{v}\int_{-\infty}^{t}\mathrm{d}t'\boldsymbol{v}\left(\boldsymbol{v}'\cdot\mathbf{E}(\mathbf{r}',t')\right)\exp\left(-\frac{t-t'}{\tau}\right)\left(\frac{\mathrm{d}f_0}{\mathrm{d}E}\right), \tag{1.22}$$

where '·' denotes the scalar product and $\boldsymbol{v}\left(\boldsymbol{v}'\cdot\mathbf{E}(\mathbf{r}',t')\right)$ represents the rescaled vector $\boldsymbol{v}$, whose components are multiplied by a scalar coefficient $\boldsymbol{v}'\cdot\mathbf{E}(\mathbf{r}',t')$. When treated as plane waves characterized by the same wave vector $\mathbf{q}$ and the frequency ω, the electric field vectors $\mathbf{E}(\mathbf{r},t)$ and $\mathbf{E}(\mathbf{r}',t')$ can be related to one another by the following transformation:

$$\mathbf{E}(\mathbf{r}',t') = \exp\left\{i\left[\mathbf{q}\left(\mathbf{r}'-\mathbf{r}\right)-\omega\left(t'-t\right)\right]\right\}\mathbf{E}(\mathbf{r},t). \tag{1.23}$$

By inserting this formula into Eq. (1.22) we get:

$$\begin{aligned}\mathbf{J}(\mathbf{r},t) = -\Bigg[&\frac{2m^3e^2}{h^3}\int\mathrm{d}\boldsymbol{v}\int_{-\infty}^{t}\mathrm{d}t'\left(\boldsymbol{v}\otimes\boldsymbol{v}'\right)\\ &\times\exp\left\{i\left[\mathbf{q}\left(\mathbf{r}'-\mathbf{r}\right)-\omega\left(t'-t\right)\right]-\frac{t-t'}{\tau}\right\}\left(\frac{\mathrm{d}f_0}{\mathrm{d}E}\right)\Bigg]\mathbf{E}(\mathbf{r},t),\end{aligned} \tag{1.24}$$

where we have made use of a dyadic/tensor product of vectors $\boldsymbol{v}$ and $\boldsymbol{v}'$ and introduced a matrix operator $(\boldsymbol{v}\otimes\boldsymbol{v}')$ defined as: $(\boldsymbol{v}\otimes\boldsymbol{v}')_{ij}\equiv v_iv'_j$ with $i,j=\{x,y,z\}$, in order to exclude the electric field vector from the integrand[4]. According to our assumption:

$$\mathbf{J}(\mathbf{r},t) = \mathbf{J}_0(\mathbf{q},\omega)\exp[i(\mathbf{q}\cdot\mathbf{r}-\omega t)]$$

$$\mathbf{E}(\mathbf{r},t) = \mathbf{E}_0(\mathbf{q},\omega)\exp[i(\mathbf{q}\cdot\mathbf{r}-\omega t)]$$

---

[3] In the following analysis we will be regarding $\delta f(\mathbf{r},\boldsymbol{v},t)$ as a first-order perturbation of the equilibrium distribution function $f_0(E)$.

[4] It is easy to check that indeed $\boldsymbol{v}(\boldsymbol{v}'\cdot\mathbf{E}) = (\boldsymbol{v}\otimes\boldsymbol{v}')\mathbf{E}$. For example: $v_x(\boldsymbol{v}'\cdot\mathbf{E}) = v_x(v'_xE_x + v'_yE_y + v'_zE_z) = \sum_j(\boldsymbol{v}\otimes\boldsymbol{v}')_{xj}E_j$.

what in connection with Eqs. (1.24) and (1.9) means that

$$\begin{aligned}\hat{\sigma}(\mathbf{q},\omega,\mathbf{B}) = -\frac{2m^3e^2}{h^3}\int \mathrm{d}\boldsymbol{v}\int_{-\infty}^{t}\mathrm{d}t'(\boldsymbol{v}\otimes\boldsymbol{v}')\\ \times\exp\left\{i\left[\mathbf{q}\left(\mathbf{r}'-\mathbf{r}\right)-\omega\left(t'-t\right)\right]-\frac{t-t'}{\tau}\right\}\left(\frac{\mathrm{d}f_0}{\mathrm{d}E}\right)\end{aligned} \tag{1.25}$$

is the frequency- and wave-vector-dependent magnetoconductivity tensor of a 3DEG that we are looking for. By using an index notation, its components can be written in the form:

$$\begin{aligned}\sigma_{ij}(\mathbf{q},\omega,\mathbf{B}) = -\frac{2m^3e^2}{h^3}\int \mathrm{d}\boldsymbol{v}\int_{-\infty}^{t}\mathrm{d}t' v_i v_j'\\ \times\exp\left\{i\left[\mathbf{q}\left(\mathbf{r}'-\mathbf{r}\right)-\omega\left(t'-t\right)\right]-\frac{t-t'}{\tau}\right\}\left(\frac{\mathrm{d}f_0}{\mathrm{d}E}\right),\end{aligned} \tag{1.26}$$

where as previously, $i, j = \{x, y, z\}$.

There are two comments that should be made on the expressions we have just derived. Firstly, as will be shown later on, the magnetic field enters the magnetoconductivity tensor only implicitly via $\boldsymbol{v}'$ and $\mathbf{r}'$, which depend on the electron cyclotron frequency $\omega_c = eB/m$. Secondly, since at low temperatures

$$\frac{\mathrm{d}f_0(E)}{\mathrm{d}E} = \frac{\mathrm{d}f_0(v)}{\mathrm{d}v}\cdot\left(\frac{\mathrm{d}E}{\mathrm{d}v}\right)^{-1} = -\left(\frac{\mathrm{d}E}{\mathrm{d}v}\right)^{-1}\delta(v-v_F), \tag{1.27}$$

where v_F is the Fermi velocity, $(\mathrm{d}E/\mathrm{d}v) = mv$ in the case of a free electron gas and $\delta(v-v_F)$ denotes the Dirac delta distribution centered around v_F, Eq. (1.26) reads

$$\begin{aligned}\sigma_{ij}(\mathbf{q},\omega,\mathbf{B}) = \frac{2m^2e^2v_F^3}{h^3}\int \mathrm{d}\Omega\int_{-\infty}^{t}\mathrm{d}t' v_i^{\Omega} v'^{\Omega}_j\\ \times\exp\left\{i\left[\mathbf{q}\left(\mathbf{r}'-\mathbf{r}\right)-\omega\left(t'-t\right)\right]-\frac{t-t'}{\tau}\right\}.\end{aligned} \tag{1.28}$$

In the above formula, $\mathrm{d}\Omega$ is the solid angle element and v_i^{Ω} as well as v'^{Ω}_j denote the angular parts of the respective velocities.

Now in order to evaluate the individual components of the magnetoconductivity tensor described by Eq. (1.28), we need first to find a kinematic relationship between vectors $\mathbf{r}$ and $\mathbf{r}'$, what in general means solving an appropriate equation of motion of an electron subject to a static magnetic field and a time- and space-dependent electric field. Proceeding this way would lead us, however, beyond the linear response theory, since at the final stage the unwanted $\mathbf{E}$-field dependence would enter the expression (1.28). Therefore, in what follows we will take into account only the Lorentz force and consider an equation of motion in the form:

$$m\frac{\mathrm{d}\boldsymbol{v}'}{\mathrm{d}t'} = -e\left(\boldsymbol{v}'\times\mathbf{B}\right), \tag{1.29}$$

with the initial conditions:

$$\mathbf{r}'(t'=t) = \mathbf{r},$$
$$\boldsymbol{\upsilon}'(t'=t) = \left(\frac{\mathrm{d}\mathbf{r}'}{\mathrm{d}t'}\right)\Bigg|_{t'=t} = \boldsymbol{\upsilon}.$$

In the preceding paragraphs we have been treating $\mathbf{r}$ and $\boldsymbol{\upsilon}$ as the final position and velocity of an electron at a given time t. In Eq. (1.28), however, the ordering of $\mathbf{r}$ and $\mathbf{r}'$ as well as t and t' is reversed. Therefore it will be more convenient from now on to regard $\mathbf{r}$ and $\boldsymbol{\upsilon}$ as the initial values of the electron's position and velocity and t as the initial time for the problem.

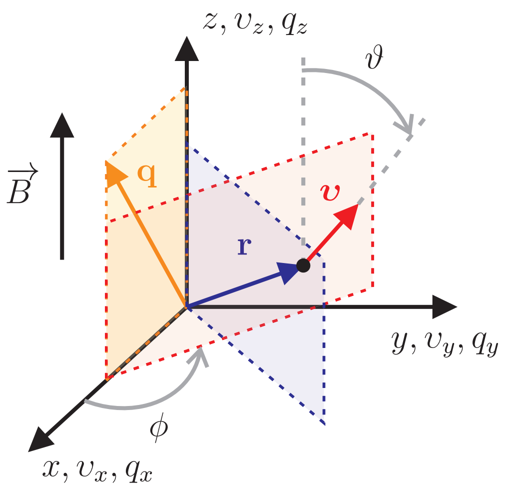

Figure 1.2: Cartesian coordinate system used for evaluation of the individual components of the magnetoconductivity tensor. Vector $\mathbf{r}$ lying in the blue plane points to the initial position (x, y, z) of an electron moving in the presence of both a static magnetic field $\mathbf{B} = [0, 0, B]$ and a time and space dependent electric field $\mathbf{E}(\mathbf{r}, t) = \mathbf{E}_0(\mathbf{q}, \omega) \exp[i(\mathbf{q} \cdot \mathbf{r} - \omega t)]$, where $\mathbf{q}$ is a wave vector lying in the yellow plane. Vector $\boldsymbol{\upsilon}$ lying in the red plane represents the initial velocity of an electron. In spherical coordinates it is fully characterized by the length υ, the polar angle ϑ and the azimuthal angle ϕ.

In Cartesian coordinate system like one shown in Fig. 1.2, Eq. (1.29) can be rewritten in the form:

$$\begin{cases} \dfrac{\mathrm{d}\upsilon'_x}{\mathrm{d}t'} = -\omega_c \upsilon'_y \\ \dfrac{\mathrm{d}\upsilon'_y}{\mathrm{d}t'} = \omega_c \upsilon'_x \\ \dfrac{\mathrm{d}\upsilon'_z}{\mathrm{d}t'} = 0 \end{cases} \tag{1.30}$$

where ω_c is the electron cyclotron frequency defined on the previous page. It is easy to check that the above set of equations is fulfilled by:

$$\begin{aligned} \upsilon'_x &= \upsilon_F \sin\vartheta \cos\left(\omega_c\left(t'-t\right)+\phi\right), \\ \upsilon'_y &= \upsilon_F \sin\vartheta \sin\left(\omega_c\left(t'-t\right)+\phi\right), \\ \upsilon'_z &= \upsilon_z = \upsilon_F \cos\vartheta, \end{aligned} \tag{1.31}$$

and

$$\begin{aligned} x' &= x + \left(\frac{\upsilon_F}{\omega_c}\right) \sin\vartheta \left\{\sin\left(\omega_c\left(t'-t\right)+\phi\right) - \sin\phi\right\}, \\ y' &= y - \left(\frac{\upsilon_F}{\omega_c}\right) \sin\vartheta \left\{\cos\left(\omega_c\left(t'-t\right)+\phi\right) - \cos\phi\right\}, \\ z' &= z + \upsilon_F \cos\vartheta \left(t'-t\right). \end{aligned} \tag{1.32}$$

where the choice of υ_F as the length of $\boldsymbol{\upsilon}'$ results directly from (1.27). Because the problem has a rotational symmetry about the z axis, in the following analysis we can assume without loss of generality that the wave vector $\mathbf{q}$ lies in the x–z plane marked in yellow in Fig. (1.2). Next we introduce a so-called non-local parameter X defined as:

$$X = \frac{q_x v_F}{\omega_c} = q_x R_c, \tag{1.33}$$

where R_c denotes the orbital radius of an electron moving perpendicular to $\mathbf{B}$ with the Fermi velocity v_F. The physical interpretation of this parameter is that it measures the extent to which the cyclotron motion of electrons probes the spatially non-uniform electric field $\mathbf{E}(\mathbf{r}, t)$. With the aid of parameter X and the relations (1.32), the argument of the exponential function in Eq. (1.28) can be rewritten in the form:

$$\begin{aligned} i\left[\mathbf{q}\left(\mathbf{r}' - \mathbf{r}\right) - \omega\left(t' - t\right)\right] - \frac{t - t'}{\tau} &= -iX\sin\vartheta\sin\left(\omega_c s - \phi\right) \\ &- iX\sin\vartheta\sin\phi - i\left(q_z v_F\cos\vartheta\right)s + i\omega s - \frac{s}{\tau}, \end{aligned} \tag{1.34}$$

where we have replaced $t - t'$ by s. By inserting this expression along with formulae (1.31) into Eq. (1.26), we can represent the integral over time t' as

$$\begin{aligned} &\int_{-\infty}^{t} \mathrm{d}t' \boldsymbol{v}'^{\Omega} \exp\left\{ i\left[\mathbf{q}\left(\mathbf{r}' - \mathbf{r}\right) - \omega\left(t' - t\right)\right] - \frac{t - t'}{\tau} \right\} = \\ &= \int_0^{\infty} \mathrm{d}s \begin{pmatrix} \sin\vartheta\cos\left(\omega_c s - \phi\right) \\ -\sin\vartheta\sin\left(\omega_c s - \phi\right) \\ \cos\vartheta \end{pmatrix} \exp\left(-iX\sin\vartheta\sin\phi\right) \\ &\times \exp\left\{ -i\left[X\sin\vartheta\sin\left(\omega_c s - \phi\right) + \left(q_z v_F\cos\vartheta\right)s - \omega s\right] - \frac{s}{\tau} \right\}. \end{aligned} \tag{1.35}$$

Let us now introduce an auxiliary function $G(X, \vartheta, \phi)$:

$$\begin{aligned} G(X, \vartheta, \phi) = \int_0^{\infty} \mathrm{d}s \exp &\left\{ -i\left[X\sin\vartheta\sin\left(\omega_c s - \phi\right)\right.\right. \\ &\left.\left. + \left(q_z v_F\cos\vartheta\right)s - \omega s\right] - \frac{s}{\tau} \right\}. \end{aligned} \tag{1.36}$$

With its help it is possible to perform the following transformation of the integral (1.35):

$$\begin{aligned} &\int_0^{\infty} \mathrm{d}s \sin\vartheta\cos\left(\omega_c s - \phi\right) \\ &\quad \times \exp\left\{ -i\left[X\sin\vartheta\sin\left(\omega_c s - \phi\right) + \left(q_z v_F\cos\vartheta\right)s - \omega s\right] - \frac{s}{\tau} \right\} = \\ &\quad = \int_0^{\infty} \mathrm{d}s \left(-\frac{i}{X}\right) \frac{\partial}{\partial\phi} \exp\left\{ -i\left[X\sin\vartheta\sin\left(\omega_c s - \phi\right) + \left(q_z v_F\cos\vartheta\right)s - \omega s\right] - \frac{s}{\tau} \right\} \\ &\quad = \left(-\frac{i}{X}\right) \frac{\partial}{\partial\phi} G(X, \vartheta, \phi), \end{aligned}$$

$$\begin{aligned}
&\int_0^\infty \mathrm{d}s\left[-\sin\vartheta\sin\left(\omega_c s-\phi\right)\right] \\
&\qquad\times\exp\left\{-i\left[X\sin\vartheta\sin\left(\omega_c s-\phi\right)+\left(q_z v_F\cos\vartheta\right)s-\omega s\right]-\frac{s}{\tau}\right\}= \\
&\qquad=\int_0^\infty \mathrm{d}s\left(-i\frac{\partial}{\partial X}\right)\exp\left\{-i\left[X\sin\vartheta\sin\left(\omega_c s-\phi\right)+\left(q_z v_F\cos\vartheta\right)s-\omega s\right]-\frac{s}{\tau}\right\} \\
&\qquad=-i\frac{\partial}{\partial X}G(X,\vartheta,\phi),
\end{aligned}$$

$$\begin{aligned}
&\int_0^\infty \mathrm{d}s\cos\vartheta\exp\left\{-i\left[X\sin\vartheta\sin\left(\omega_c s-\phi\right)+\left(q_z v_F\cos\vartheta\right)s-\omega s\right]-\frac{s}{\tau}\right\}= \\
&\qquad=\left(\cos\vartheta\right)\cdot G(X,\vartheta,\phi).
\end{aligned}$$

based on the use of differentiation under the integral sign [19, 20]. Taking them into account the magnetoconductivity tensor can now be expressed as

$$\begin{aligned}
\hat{\sigma}(\mathbf{q},\omega,\mathbf{B})=&\frac{2m^2e^2v_F^3}{h^3}\int \mathrm{d}\Omega\exp\left(-iX\sin\vartheta\sin\phi\right) \\
&\times\begin{pmatrix}\sin\vartheta\cos\phi\\ \sin\vartheta\sin\phi\\ \cos\vartheta\end{pmatrix}\otimes\begin{pmatrix}-(i/X)\partial/\partial\phi\\ -i\partial/\partial X\\ \cos\vartheta\end{pmatrix}G(X,\vartheta,\phi).
\end{aligned}\tag{1.37}$$

In the next step we perform the integration over s in the function $G(X,\vartheta,\phi)$, utilizing the following relation [18, 21]:

$$\exp\left(iz\sin\psi\right)=\sum_{n=-\infty}^{\infty}J_n(z)\exp(in\psi),\tag{1.38}$$

which yields

$$\begin{aligned}
\hat{\sigma}(\mathbf{q},\omega,\mathbf{B})=&\frac{2m^2e^2v_F^3\tau}{h^3}\sum_{n=-\infty}^{\infty}\int_0^{2\pi}\mathrm{d}\phi\int_0^{\pi}\sin\vartheta\mathrm{d}\vartheta\begin{pmatrix}\sin\vartheta\cos\phi\\ \sin\vartheta\sin\phi\\ \cos\vartheta\end{pmatrix}\exp\left(-iX\sin\vartheta\sin\phi\right) \\
&\otimes\begin{pmatrix}-(i/X)\partial/\partial\phi\\ -i\partial/\partial X\\ \cos\vartheta\end{pmatrix}\frac{J_n(X\sin\vartheta)\exp(in\phi)}{1+i(n\omega_c+q_z v_F\cos\vartheta-\omega)\tau},
\end{aligned}\tag{1.39}$$

where $J_n(z)$ denotes the Bessel function of the first kind and order n (see Fig. 1.3 showing graphs of the first eight Bessel functions of the non-negative order). To proceed further, let us notice that marked in blue term in the above equation can be rewritten in the form:

$$\begin{pmatrix}\sin\vartheta\cos\phi\\ \sin\vartheta\sin\phi\\ \cos\vartheta\end{pmatrix}\exp\left(-iX\sin\vartheta\sin\phi\right)=\begin{pmatrix}(i/X)\partial/\partial\phi\\ i\partial/\partial X\\ \cos\vartheta\end{pmatrix}\exp\left(-iX\sin\vartheta\sin\phi\right),\tag{1.40}$$

and by means of Eq. (1.38) transformed into:

$$\begin{pmatrix} (i/X)\partial/\partial\phi \\ i\partial/\partial X \\ \cos\vartheta \end{pmatrix} \exp\left(-iX\sin\vartheta\sin\phi\right) = \\ = \sum_{n'=-\infty}^{\infty} \begin{pmatrix} (i/X)\partial/\partial\phi \\ i\partial/\partial X \\ \cos\vartheta \end{pmatrix} J_{n'}(X\sin\vartheta)\exp(-in'\phi). \tag{1.41}$$

Substituting this result into Eq. (1.39) leads to

$$\hat{\sigma}(\mathbf{q},\omega,\mathbf{B}) = \frac{2m^2e^2v_F^3\tau}{h^3}\sum_{n=-\infty}^{\infty}\sum_{n'=\infty}^{\infty}\int_0^{2\pi}\mathrm{d}\phi\exp(i(n-n')\phi)\int_0^{\pi}\sin\vartheta\mathrm{d}\vartheta \\ \times\left\{\begin{pmatrix} n'/X \\ i\partial/\partial X \\ \cos\vartheta \end{pmatrix} J_{n'}(X\sin\vartheta)\right\}\otimes\left\{\begin{pmatrix} n/X \\ -i\partial/\partial X \\ \cos\vartheta \end{pmatrix}\frac{J_n(X\sin\vartheta)}{1+i(n\omega_c+q_zv_F\cos\vartheta-\omega)\tau}\right\}. \tag{1.42}$$

Integral over ϕ that appears in the above formula is nothing else but the Kronecker delta [18, 19]:

$$\delta_{n,n'} = \frac{1}{2\pi}\int_0^{2\pi}\mathrm{d}\phi\exp(i(n-n')\phi),$$

thus

$$\hat{\sigma}(\mathbf{q},\omega,\mathbf{B}) = \frac{4\pi m^2e^2v_F^3\tau}{h^3}\sum_{n=-\infty}^{\infty}\int_0^{\pi}\mathrm{d}\vartheta\sin\vartheta\left\{\begin{pmatrix} n/X \\ i\partial/\partial X \\ \cos\vartheta \end{pmatrix} J_n(X\sin\vartheta)\right\} \\ \otimes\left\{\begin{pmatrix} n/X \\ -i\partial/\partial X \\ \cos\vartheta \end{pmatrix}\frac{J_n(X\sin\vartheta)}{1+i(n\omega_c+q_zv_F\cos\vartheta-\omega)\tau}\right\}. \tag{1.43}$$

In a three-dimensional case, the Fermi velocity v_F of a degenerate electron gas is related to its concentration N by [22–24]:

$$v_F = \frac{\hbar}{m}k_F = \frac{\hbar}{m}\left(3\pi^2N\right)^{1/3}, \tag{1.44}$$

where k_F denotes the Fermi wave vector and $\hbar = h/2\pi$. Knowing this, we can rewrite the prefactor standing in front of expression (1.43) in the following way:

$$\frac{4\pi m^2e^2v_F^3\tau}{h^3} = \frac{3}{2}\frac{Ne^2\tau}{m} = \frac{3}{2}Ne\mu = \frac{3}{2}\sigma_0 \tag{1.45}$$

where we have introduced an electron drift mobility $\mu = e\tau/m$ and a DC conductivity $\sigma_0 = Ne\mu$ of an electron gas under consideration.

In a further analysis we will restrict ourselves to electric perturbations propagating in the electron gas perpendicularly to the applied magnetic field, i.e. to the case

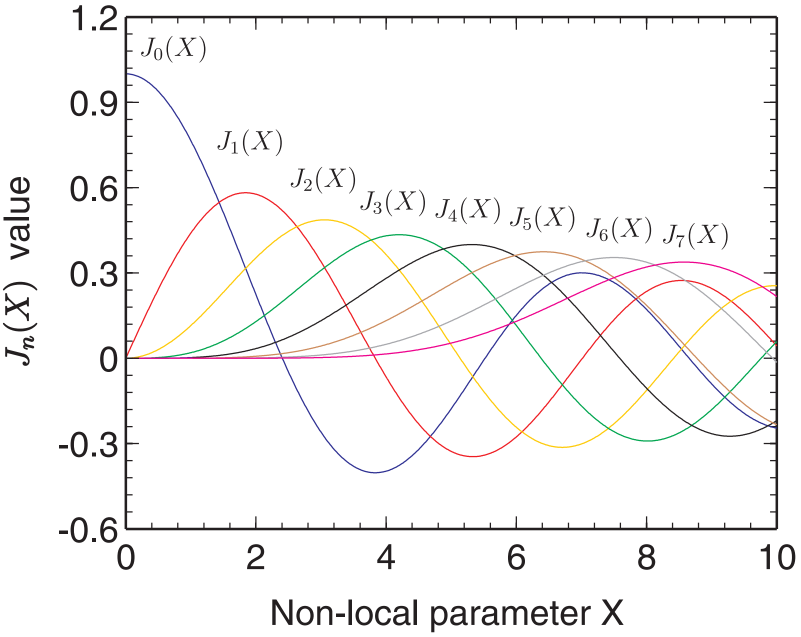

Figure 1.3: Graphs of the first eight Bessel functions of the non-negative order.

$\mathbf{q} \perp \mathbf{B} \Rightarrow q_z \equiv 0$, since it was the experimental configuration for the investigations described in the remaining part of this dissertation. Under such conditions, a careful inspection of Eq. (1.43) leads to immediate conclusion that $\sigma_{xz} = \sigma_{zx} = \sigma_{yz} = \sigma_{zy} = 0$. σ_{xz} and σ_{zx} components of the magnetoconductivity tensor vanish because they comprise the integral

$$\begin{aligned}\int_0^\pi J_n^2(X\sin\vartheta)\sin\vartheta\cos\vartheta \mathrm{d}\vartheta &= \frac{1}{2}\int_0^\pi \mathrm{d}\vartheta J_n^2(X\sin\vartheta)\sin 2\vartheta \\ &= \frac{1}{4}\int_0^{2\pi} \mathrm{d}\alpha J_n^2(X\sin(\alpha/2))\sin(\alpha) = 0,\end{aligned}$$

where $J_n^2(X\sin(\alpha/2))$ and $\sin(\alpha)$ are even and odd periodic functions of α, respectively, what means that their product disappears when integrated over the 2π range. The proof of vanishing of the σ_{yz} and σ_{zy} components is a little bit more complicated. As can be inferred from Eq. (1.43) the angular integral they contain reads

$$\begin{aligned}\pm i\int_0^\pi J_n(X\sin\vartheta)\frac{\partial}{\partial X}J_n(X\sin\vartheta)\cos\vartheta\sin\vartheta \mathrm{d}\vartheta = \\ = \pm i\int_0^\pi J_n(X\sin\vartheta)J_n'(X\sin\vartheta)\sin^2\vartheta\cos\vartheta \mathrm{d}\vartheta,\end{aligned} \tag{1.46}$$

where + and − signs refer to the yz and zy components, respectively, and a prime symbol denotes the derivative with respect to the full argument of the function $J_n(X\sin\vartheta)$. Now let us recall two famous identities for the Bessel functions of the first kind [18, 21]:

$$\frac{2n}{\xi}J_n(\xi) = J_{n-1}(\xi) + J_{n+1}(\xi), \tag{1.47}$$

$$2\frac{\mathrm{d}}{\mathrm{d}\xi}J_n(\xi) = J_{n-1}(\xi) - J_{n+1}(\xi). \tag{1.48}$$

Multiplying them side by side yields

$$J_n(\xi)\frac{\mathrm{d}}{\mathrm{d}\xi}J_n(\xi) = \frac{\xi}{4n}\left(J_{n-1}^2(\xi) - J_{n+1}^2(\xi)\right).$$

With the aid of this relation the integral (1.46) can be rewritten in the form:

$$\begin{aligned}
&\pm i\int_0^{\pi} J_n(X\sin\vartheta)J_n'(X\sin\vartheta)\sin^2\vartheta\cos\vartheta\mathrm{d}\vartheta = \\
&= \pm i\frac{X}{4n}\int_0^{\pi}\left(J_{n-1}^2(X\sin\vartheta) - J_{n+1}^2(X\sin\vartheta)\right)\sin^3\vartheta\cos\vartheta\mathrm{d}\vartheta \\
&= \pm i\frac{X}{16n}\int_0^{2\pi}\mathrm{d}\alpha\left(J_{n-1}^2\left(X\sin(\alpha/2)\right) - J_{n+1}^2\left(X\sin(\alpha/2)\right)\right) \\
&\qquad \times\sin^2(\alpha/2)\sin(\alpha) = 0
\end{aligned}$$

since like previously, a part of the integrand marked in blue represents a periodic and even function of α whereas $\sin(\alpha)$ is an odd function of its argument, so their product vanishes after integration over the 2π range. Another important property displayed by the magnetoconductivity tensor (1.43) is that $\sigma_{xy} = -\sigma_{yx}$. Thus, in order to fully characterize it in the case of propagation perpendicular to the applied magnetic field, $\mathbf{q}\perp\mathbf{B}$, it is sufficient to evaluate only four of its nine, generally non-zero components: $\sigma_{xx}, \sigma_{yy}, \sigma_{zz}$ and σ_{xy}. Taking into account Eqs. (1.43) and (1.45) they can be represented as:

$$\sigma_{xx} = \frac{3\sigma_0}{2X^2}\sum_{n=-\infty}^{\infty} n^2\int_0^{\pi}\frac{J_n^2(X\sin\vartheta)\sin\vartheta}{1+i(n\omega_c-\omega)\tau}\mathrm{d}\vartheta, \tag{1.49}$$

$$\sigma_{xy} = -\sigma_{yx} = -\frac{3i\sigma_0}{2X}\sum_{n=-\infty}^{\infty} n\int_0^{\pi}\frac{J_n(X\sin\vartheta)J_n'(X\sin\vartheta)\sin^2\vartheta}{1+i(n\omega_c-\omega)\tau}\mathrm{d}\vartheta, \tag{1.50}$$

$$\sigma_{yy} = \frac{3\sigma_0}{2}\sum_{n=-\infty}^{\infty}\int_0^{\pi}\frac{\left[J_n'(X\sin\vartheta)\right]^2\sin^3\vartheta}{1+i(n\omega_c-\omega)\tau}\mathrm{d}\vartheta, \tag{1.51}$$

$$\sigma_{zz} = \frac{3\sigma_0}{2}\sum_{n=-\infty}^{\infty}\int_0^{\pi}\frac{J_n^2(X\sin\vartheta)\cos^2\vartheta\sin\vartheta}{1+i(n\omega_c-\omega)\tau}\mathrm{d}\vartheta, \tag{1.52}$$

where as previously, a prime symbol is used for derivative with respect to the full argument of a given function. Finally, we would like to stress that in general, for

$B \neq 0$ and an arbitrary wavelength λ of the applied electric field, $\sigma_{xx} \neq \sigma_{yy}$ since obviously[5]

$$\frac{n^2}{X^2} J_n^2(X \sin\vartheta) \sin\vartheta \neq \left[J_n'(X \sin\vartheta)\right]^2 \sin^3\vartheta.$$

Only in the local limit, when $X \ll 1$ what means that $\lambda \gg R_c$, the above expression becomes an identity, what can be shown by expanding the Bessel functions $J_n(X \sin\vartheta)$ into Taylor series around zero:

$$J_n(\xi) \approx \frac{1}{\Gamma(n+1)} \left(\frac{\xi}{2}\right)^n, \tag{1.53}$$

where $\Gamma(n+1)$ denotes the Euler gamma function [18,21]. Under such conditions, to the lowest, non-vanishing order in n ($n = \{-1, 1\}$ for the σ_{xx}, σ_{xy} and σ_{yy} and $n = 0$ in the case of σ_{zz} component), Eqs. (1.49)-(1.52) read:

$$\sigma_{xx} = \sigma_{yy} = i\frac{Ne^2}{m} \cdot \frac{\omega + i/\tau}{(\omega + i/\tau)^2 - \omega_c^2}, \tag{1.54}$$

$$\sigma_{xy} = -\sigma_{yx} = \frac{Ne^2}{m} \cdot \frac{\omega_c}{(\omega + i/\tau)^2 - \omega_c^2}, \tag{1.55}$$

$$\sigma_{zz} = i\frac{Ne^2}{m} \cdot \frac{\omega - i/\tau}{\omega^2 + 1/\tau^2}, \tag{1.56}$$

and are identical with the results that can be obtained within the simplest generalization of the model of an electron gas that was originally proposed by Drude for zero magnetic field [22,24,25].

1.2.2 Two-dimensional electron gas

As mentioned in the introduction to this chapter, the derivation of the magnetoconductivity tensor of a 2DEG proceeds in an analogous way to the three-dimensional case. The final formulae, however, look different since, as we might have seen, there are certain stages at which direct referring to the dimensionality of the system is required. Thus, all that we have to do in order to obtain a 2D magnetoconductivity tensor, is to find those points and replace the respective expressions valid for a 3DEG with ones that are appropriate for a 2DEG. The list of necessary changes is presented below.

1. Starting with Eq. (1.1), the prefactor in the subsequent integrals representing either the electron concentration or the electron current density should be replaced with $2m^2/h^2$. This results from a difference in the density of states in the

---

[5] A general lack of equivalence between the x- and y-direction originates from the assumption that the electric field wave propagates along only one of them (namely x- in our case).

momentum space, which for a D-dimensional free electron gas can be expressed as [26]:

$$\rho^D(E)\mathrm{d}E = \left(\prod_{i=1}^{D} L_i\right)\left(\frac{2m^D}{h^D}\right)\upsilon^{D-1}\mathrm{d}\upsilon\mathrm{d}\Omega_D, \tag{1.57}$$

where L_i denotes the length of the system in the i-th dimension, υ is the value of the electron velocity, $\mathrm{d}\Omega_D$ stands for the solid angle element in D-dimensional space and both spin orientations have been taken into account.

2. In Eq. (1.28) and its further modifications $\int \mathrm{d}\Omega$ should be interpreted as an integral over the azimuthal angle only, since the motion of electrons is now restricted to the x-y plane. This means, in particular, that the wave vector $\mathbf{q}$, appearing for the first time in Eq. (1.8), has no q_z component not only in the $\mathbf{q} \perp \mathbf{B}$ configuration but in general. Moreover, the prefactor of the integral in Eq. (1.28) and all subsequent expressions derived from it should read: $(2me^2\upsilon_F^2)/h^2$.

3. By definition, in the set of equations (1.30), there should be no differential equation for the υ_z' component of the electron velocity.

4. Beginning with Eqs. (1.31), $\vartheta = \pi/2$ has to be inserted into the formulae derived for the 3D case in order to obtain the results valid for a 2DEG.

Taking into account the remarks stated above, the 2D analogue of Eq. (1.43) can be written as:

$$\begin{aligned}\hat{\sigma}(\mathbf{q},\omega,\mathbf{B}) = \frac{4\pi me^2\upsilon_F^2\tau}{h^2}\sum_{n=-\infty}^{\infty} &\left\{\begin{pmatrix} n/X \\ i\mathrm{d}/\mathrm{d}X \end{pmatrix} J_n(X)\right\} \\ &\otimes\left\{\begin{pmatrix} n/X \\ -i\mathrm{d}/\mathrm{d}X \end{pmatrix}\frac{J_n(X)}{1+i(n\omega_c-\omega)\tau}\right\},\end{aligned} \tag{1.58}$$

where υ_F is now a 2D Fermi velocity related to the concentration N of a 2DEG by

$$\upsilon_F = \frac{\hbar}{m}\left(2\pi N\right)^{1/2}. \tag{1.59}$$

After inserting this formula into Eq. (1.58), the components of the 2D magnetoconductivity tensor acquire the final form:

$$\sigma_{xx} = \frac{2\sigma_0}{X^2}\sum_{n=-\infty}^{\infty}\frac{n^2J_n^2(X)}{1+i(n\omega_c-\omega)\tau} \tag{1.60}$$

$$\sigma_{xy} = -\sigma_{yx} = -i\frac{2\sigma_0}{X}\sum_{n=-\infty}^{\infty}\frac{nJ_n(X)J_n'(X)}{1+i(n\omega_c-\omega)\tau} \tag{1.61}$$

$$\sigma_{yy} = 2\sigma_0\sum_{n=-\infty}^{\infty}\frac{\left[J_n'(X)\right]^2}{1+i(n\omega_c-\omega)\tau}, \tag{1.62}$$

where we have introduced a DC conductivity of a 2DEG: $\sigma_0 = Ne^2\tau/m$, and replaced $\mathrm{d}/\mathrm{d}X$ with a prime symbol. In a full analogy to the three-dimensional case, also here, in general $\sigma_{xx} \neq \sigma_{yy}$. These two components approach each other only in the local limit ($\lambda \gg R_c$). Under such conditions, when the infinite series of non-local corrections to the magnetoconductivity tensor are additionally restricted to the lowest order terms, Eqs. (1.60)-(1.62) become identical with Eqs. (1.54)-(1.55), except for different units of the electron gas concentration.

When comparing the experimental results with the predictions of theoretical models that we are discussing in this chapter, we will be mainly interested in dispersion curves relating the resonant energies of the magnetoplasmon modes to their wave vectors. Therefore, we will frequently use the collisionless ($\tau \to \infty$) form of the expressions (1.60)-(1.62):

$$\sigma_{xx} = i\frac{4Ne^2\omega}{mX^2}\sum_{n=1}^{\infty}\frac{n^2 J_n^2(X)}{\omega^2 - (n\omega_c)^2}, \tag{1.63}$$

$$\sigma_{xy} = -\sigma_{yx} = \frac{4Ne^2\omega_c}{mX}\sum_{n=1}^{\infty}\frac{n^2 J_n(X)J_n'(X)}{\omega^2 - (n\omega_c)^2}, \tag{1.64}$$

$$\sigma_{yy} = i\frac{4Ne^2\omega}{m}\left\{\frac{[J_0'(X)]^2}{2\omega^2} + \sum_{n=1}^{\infty}\frac{[J_n'(X)]^2}{\omega^2 - (n\omega_c)^2}\right\}. \tag{1.65}$$

In order to obtain them, an independent summation over the negative and positive subsets of n should be performed first, followed by taking the $\tau \to \infty$ limit and rewriting the resulting formulae in a more legible and concise way with the use of some algebraic manipulations based on identities (1.47)-(1.48) and the relation [18,21]:

$$J_{-n}(X) = (-1)^n J_n(X). \tag{1.66}$$

1.3 Dispersion relation of two-dimensional magnetoplasmons

1.3.1 Derivation

Having constructed the 2D magnetoconductivity tensor, we are now prepared to derive the dispersion relation of magnetoplasma waves in a 2DEG embedded in a three-dimensional dielectric medium characterized by a static dielectric constant ε_s (see Fig. 1.4). In what follows, we will assume that the electron gas is confined to the x–y plane located at $z = 0$ in the Cartesian coordinate system and subject to the external, static magnetic field $\mathbf{B}_0 = [0, 0, B_0]$. Furthermore, we will consider this layer as strictly two-dimensional, with zero thickness along the z-direction, but no restrictions imposed on its size in the x-y plane. Similarly, the dielectric surrounding of a 2DEG will be treated as an infinite medium in all directions in order to minimize the influence of finite size effects on the dispersion relation we are going to derive.

To begin with, let us denote by $\mathbf{E}(\mathbf{r},t)$ and $\mathbf{B}(\mathbf{r},t)$ the electric and the magnetic field associated with the plasma oscillations propagating in the plane of a 2DEG. Because the system under investigation displays a rotational symmetry about the z-axis, we can suppose that the magnetoplasmon wave vector $\mathbf{q}$ has only one non-zero component, namely q_x, and as a result, the spatial and temporal variation of $\mathbf{E}(\mathbf{r},t)$ and $\mathbf{B}(\mathbf{r},t)$ fields is described by $\exp[i(q_x x - \omega t)]$. In the latter expression, ω represents the angular frequency of the magnetoplsmon mode. The electric and magnetic fields have to satisfy the Maxwell equations:

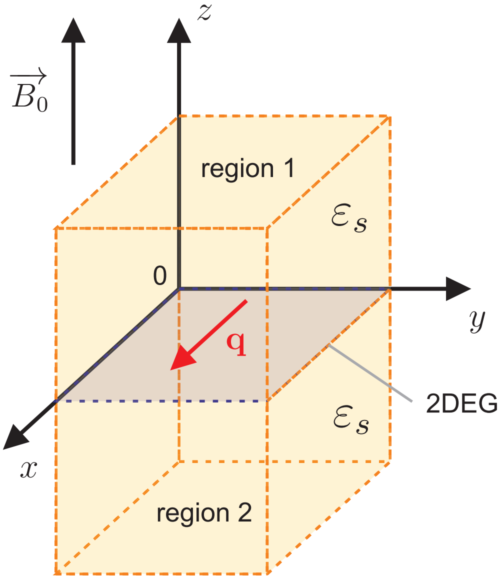

Figure 1.4: Schematic representation of a 2DEG layer occupying the x-y plane at $z = 0$ and subject to an external, static magnetic field $\mathbf{B}_0$ pointing in the z-direction. Space surrounding the 2DEG is filled in with dielectric medium characterized by a static dielectric constant ε_s. For convenience of calculations, it is divided into two regions: *region 1* for $z > 0$ and *region 2* for $z < 0$. Red arrow depicts the wave vector $\mathbf{q} = q_x\hat{x}$ of a magnetoplasma wave propagating in the x-direction.

$$\nabla \times \mathbf{E}(\mathbf{r},t) = -\frac{\partial \mathbf{B}(\mathbf{r},t)}{\partial t}, \tag{1.67}$$

$$\nabla \times \mathbf{B}(\mathbf{r},t) = \mu_0\varepsilon_0\varepsilon_s\frac{\partial \mathbf{E}(\mathbf{r},t)}{\partial t} + \mu_0\mathbf{j}(x,y,t)\delta(z), \tag{1.68}$$

where μ_0 and ε_0 are the magnetic susceptibility and the dielectric permeability of the free space and $\mathbf{j}(x,y,t)\delta(z)$ denotes the surface current induced in the 2DEG layer by the self-consistent field with $\delta(z)$ standing for the Dirac delta distribution at $z = 0$. It is easy to check that everywhere except the $z = 0$ plane, the above equations are fulfilled by

$$\mathbf{E}(x,y,z,t) = \mathbf{E}_0 \exp\left[i\left(q_x x - \omega t \pm q_z z\right)\right] \tag{1.69}$$

with the relations:

$$q_z^2 + q_x^2 = \mu_0\varepsilon_0\varepsilon_s\omega^2, \tag{1.70}$$

$$\mp q_z E_z(x,y,z,t) = q_x E_x(x,y,z,t), \tag{1.71}$$

where we have introduced the $\exp(\pm iq_z z)$ factor to account for the fact, that far away from the conducting plane, the electromagnetic wave of a longitudinal character has to vanish, since in the free space and isotropic dielectrics, only transverse waves can be sustained [5, 6]. In its general form, the $\exp(\pm iq_z z)$ term can represent both the vanishing and non-vanishing modes as well as waves with either exponentially growing or exponentially decaying amplitude. In order to meet the requirement of waves disappearing away from the conducting plane, we have to impose on it the following restrictions:

$$q_z^2 < 0 \Rightarrow \beta^2 = q_x^2 - \mu_0\varepsilon_0\varepsilon_s\omega^2 > 0, \tag{1.72}$$

and

$$\mathbf{E}_1(\mathbf{r}, t) = \mathbf{E}_{01}\exp(-|\beta|z)\exp\left[i\left(q_x x - \omega t\right)\right] \qquad \text{for } z > 0, \tag{1.73}$$

$$\mathbf{E}_2(\mathbf{r}, t) = \mathbf{E}_{02}\exp(|\beta|z)\exp\left[i\left(q_x x - \omega t\right)\right] \qquad \text{for } z < 0, \tag{1.74}$$

where for convenience in further calculations, we have divided the dielectric surrounding of a 2DEG into two regions, in which the relevant quantities will be labelled with subscripts: 1 for $z > 0$ and 2 for $z < 0$. Then, by inserting formulae (1.73)-(1.74) into Eq. (1.68) with $\nabla \times \mathbf{B}(\mathbf{r}, t)$ term expressed via Eq. (1.67), it is straightforward to demonstrate that:

$$\mathbf{E}_{1,2}(\mathbf{r}, t) = \begin{pmatrix} E_x \\ E_y \\ \pm i\dfrac{q_x}{|\beta|}E_x \end{pmatrix} \exp\left(\mp|\beta|z\right)\exp\left[i\left(q_x x - \omega t\right)\right], \tag{1.75}$$

where the upper signs in ± and ∓ symbols refer to the region 1 whereas the bottom ones to the region 2 and E_x as well as E_y can be chosen arbitrarily, represent a solution to Maxwell's equations (1.67)-(1.68) everywhere except for the $z = 0$ plane. As can be inferred from the above result, the derivatives of E_x and E_y with respect to z and E_z components of the electric fields $\mathbf{E}_{1,2}(\mathbf{r}, t)$ are discontinuous at this plane. This means that $\partial^2 E_x/\partial z^2$, $\partial^2 E_y/\partial z^2$ and $\partial E_z/\partial z$ have δ-function singularities at $z = 0$, what can formally be expressed as:

$$\frac{\partial^2 E_x}{\partial z^2} = \beta^2 E_x - 2|\beta|E_x(z = 0)\delta(z), \tag{1.76}$$

$$\frac{\partial^2 E_y}{\partial z^2} = \beta^2 E_y - 2|\beta|E_y(z = 0)\delta(z), \tag{1.77}$$

$$\frac{\partial E_z}{\partial z} = \mp|\beta|E_z + 2i\frac{q_x}{|\beta|}E_x(z = 0^+)\delta(z), \tag{1.78}$$

where $z = 0^+$ denotes approaching the $z = 0$ plane from the region 1 side and the explicit indication of dependence of the electric field components on x, y and t variables have been omitted for clarity. Now, we are well prepared for solving Eq. (1.68) with substituted Eq. (1.67) also for the $z = 0$ plane occupied by a 2DEG. After collecting terms that contain a δ-function, the solution takes on the form:

$$2\begin{pmatrix} -\mu_0\varepsilon_0\varepsilon_s\omega^2 E_x/|\beta| \\ |\beta|E_y \end{pmatrix} = i\omega\mu_0 \begin{pmatrix} j_x \\ j_y \end{pmatrix}. \tag{1.79}$$

On the other hand we know that due to Ohm's law: $\mathbf{j} = \hat{\sigma}\mathbf{E}$, where $\hat{\sigma}$ stands for the non-local magnetoconductivity tensor of a 2DEG that we have previously derived in this chapter (refer to Eqs. (1.58)-(1.62) for relevant expressions). This means that Eq. (1.79) can be rewritten in the following way:

$$-i\frac{2}{\omega\mu_0}\begin{pmatrix} -\mu_0\varepsilon_0\varepsilon_s\omega^2 E_x/|\beta| \\ |\beta|E_y \end{pmatrix} = \begin{pmatrix} \sigma_{xx} & \sigma_{xy} \\ -\sigma_{xy} & \sigma_{yy} \end{pmatrix}\begin{pmatrix} E_x \\ E_y \end{pmatrix} \tag{1.80}$$

and hence

$$\begin{pmatrix} i\dfrac{2\varepsilon_0\varepsilon_s\omega}{|\beta|} - \sigma_{xx} & -\sigma_{xy} \\ \sigma_{xy} & -i\dfrac{2|\beta|}{\omega\mu_0} - \sigma_{yy} \end{pmatrix}\begin{pmatrix} E_x \\ E_y \end{pmatrix} = 0. \tag{1.81}$$

The general form of dispersion relation of magnetoplasmon excitations is then readily obtained by setting the determinant of the above matrix to be equal to 0:

$$\left(\frac{2\varepsilon_0\varepsilon_s\omega}{|\beta|} + i\sigma_{xx}\right)\left(\frac{2|\beta|}{\omega\mu_0} - i\sigma_{yy}\right) + \sigma_{xy}^2 = 0. \tag{1.82}$$

It should be emphasized here that in the formula we have just derived, each component of the magnetoconductivity tensor as well as β represent the functions of both the frequency ω and the wave vector $\mathbf{q}$ characterizing the magnetoplasma oscillations.

As can be seen, Eq. (1.82) is quite complex. However, under many experimental conditions, the general form of dispersion relation can be significantly simplified. This is actually the case of research being the subject of this dissertation. In order to see that, let us first work a little bit more on the function $|\beta|$. From (1.72) we know that:

$$|\beta| = \left(q^2 - \mu_0\varepsilon_0\varepsilon_s\omega^2\right)^{1/2} = q\left(1 - \frac{\mu_0\varepsilon_0\varepsilon_s\omega^2}{q^2}\right)^{1/2}, \tag{1.83}$$

where we have dropped the x subscript in q_x since there is no other component of the magnetoplasmon wave vector. In the case of typical intrasubband magnetoplasmon excitations that can be observed in doped semiconductors: $\varepsilon_s \sim 10$, $q \sim 10^6$–$10^7\,\mathrm{m}^{-1}$ and $\omega \sim 10^{13}\,\mathrm{rad/s}$. By substituting these values into the right-hand side of Eq. (1.83), we get the following estimation for the order of magnitude of the second term in parentheses:

$$\frac{\mu_0\varepsilon_0\varepsilon_s\omega^2}{q^2} \sim 10^{-4}\text{–}10^{-2} \ll 1,$$

what means that under the above conditions we can safely assume that $|\beta| \simeq q$.

In order to further simplify the general form of Eq. (1.82), let us numerically solve it for the case, when all the series appearing in expressions for the components of the magnetoconductivity tensor are limited to the lowest order terms with $n = \{0, 1\}$. If we additionally restrict our analysis to the colisionless limit (i.e. $\tau \to \infty$), then according to Eqs. (1.63)-(1.65), the dispersion relation (1.82) reads:

$$\left(\frac{2\varepsilon_0\varepsilon_s\omega}{q} - \frac{\alpha\omega}{X^2}\frac{J_1^2(X)}{\omega^2-\omega_c^2}\right)\left(\frac{2q}{\omega\mu_0} + \alpha\omega\left\{\frac{[J_0'(X)]^2}{2\omega^2} + \frac{[J_1'(X)]^2}{\omega^2-\omega_c^2}\right\}\right) + \\ + \frac{\alpha^2\omega_c^2}{X^2}\frac{[J_1(X)J_1'(X)]^2}{\left(\omega^2-\omega_c^2\right)^2} = 0, \tag{1.84}$$

where $\alpha = 4Ne^2/m$. After some straightforward algebraic manipulations and reducing to a common denominator, the above equation can be rewritten in the following form:

$$C_4\omega^4 + C_2\omega^2 + C_0 = 0, \tag{1.85}$$

where:

$$C_4 = -\varepsilon_0\varepsilon_s\left\{\frac{4}{\mu_0} + \frac{\alpha}{q}\left([J_0'(X)]^2 + 2\,[J_1'(X)]^2\right)\right\}, \tag{1.86}$$

$$C_2 = \frac{\alpha q J_1^2(X)}{2X^2}\left\{\frac{4}{\mu_0} + \frac{\alpha}{q}\left([J_0'(X)]^2 + 2\,[J_1'(X)]^2\right)\right\} + \\ + 2\varepsilon_0\varepsilon_s\omega_c^2\left\{\frac{4}{\mu_0} + \frac{\alpha}{q}\left([J_0'(X)]^2 + [J_1'(X)]^2\right)\right\}, \tag{1.87}$$

$$C_0 = -\frac{\alpha q\omega_c^2 J_1^2(X)}{2X^2}\left\{\frac{4}{\mu_0} + \frac{\alpha}{q}\left([J_0'(X)]^2 + 2\,[J_1'(X)]^2\right)\right\} + \\ - \varepsilon_0\varepsilon_s\omega_c^4\left\{\frac{4}{\mu_0} + \frac{\alpha}{q}\,[J_0'(X)]^2\right\} \tag{1.88}$$

and ω can take any value except for 0 and ω_c (the cyclotron frequency). An example of numerical results that can obtained with the help of these formulae for typical values of material parameters corresponding to GaN (2DEG concentration $N = 10^{17}\,\mathrm{m}^{-2}$, the cyclotron resonance effective mass of electrons $m = m^* = 0.22\,m_0$ [27–33], and the static dielectric constant $\varepsilon_s = 9.28$ [34]) is shown with open circles in Fig. 1.5 for three lengths of the magnetoplasmon wave vector: $q = 10^5\,\mathrm{m}^{-1}$, $10^6\,\mathrm{m}^{-1}$, and $10^7\,\mathrm{m}^{-1}$. For convenience of readers that are more used to other units, we would like to remind

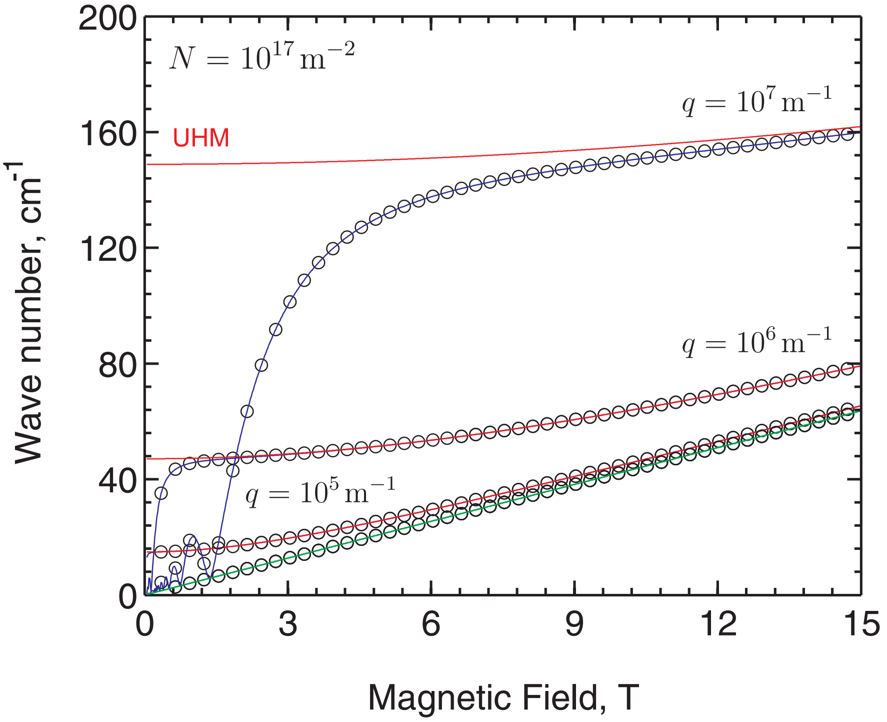

Figure 1.5: Magnetic-field dependence of the characteristic energy of magnetoplasma oscillations, calculated with the aid of: 1) (open circles) the general form of dispersion relation limited to the lowest-order terms with $n = \{0, 1\}$ (refer to Eqs. (1.84) and (1.90)), 2) (solid blue curves) an approximated form of expression (1.90) given by Eq. (1.91), and 3) (solid red curves) an asymptotic form of Eq. (1.91) describing the so-called upper hybrid mode (UHM) and valid for $X \ll 1$, i.e. in the local limit. Solid green line represents the cyclotron frequency. Oscillations that occur in the low-magnetic-field results of calculations carried out with the use of non-local formulae (i.e. for arbitrary X) originate from the shape of Bessel functions. Dips/valleys are due to limiting the infinite series of non-local corrections to the magnetoconductivity tensor to the lowest-order terms.

that the angular frequency ω expressed in rad/s and the wave number $1/\lambda$ expressed in cm^{-1} are related to one another by: $1/\lambda = \omega/(200\pi c)$, where c denotes the speed of light expressed in m/s. As expected from its polynomial form, Eq. (1.85) have four roots at each magnetic field. Since it contains only the even-power terms, these roots can be written as $\pm\Omega_1$ and $\pm\Omega_2$. It can easily be verified that, let say, Ω_1^2 is strictly equal to square of the cyclotron frequency. As a result, $\pm\Omega_1$ cannot represent a good solution to the approximated dispersion relation described by Eq. (1.84), since for $\omega = \omega_c$ it becomes indefinite. In order to obtain an analytical expression for the remaining roots, $\pm\Omega_2$, let us first note that Eq. (1.85) can equally well be displayed in the form:

$$C_4\left(\omega^2 - \Omega_1^2\right)\left(\omega^2 - \Omega_2^2\right) = C_4\left(\omega^2 - \omega_c^2\right)\left(\omega^2 - \Omega_2^2\right) = 0. \tag{1.89}$$

Then, by comparing the coefficients standing in front of the corresponding terms in

Eqs. (1.85) and (1.89), it is straightforward to show that $\Omega_2^2 = C_0/\omega_c^2 C_4$, what after making use of Eqs. (1.86) and (1.88) as well as the definition of α leads to the following formula:

$$\Omega_2^2 = \frac{2Ne^2 J_1^2(X)}{\varepsilon_0 \varepsilon_s m X^2} q + \omega_c^2 \left\{ 1 - \frac{2\left[J_1'(X)\right]^2}{qm/N\mu_0 e^2 + \left[J_0'(X)\right]^2 + 2\left[J_1'(X)\right]^2} \right\}. \tag{1.90}$$

For $m = 0.22m_0$, $m/\mu_0 e^2 \approx 6.2 \times 10^{12}\,\mathrm{m}^{-1}$. Furthermore, from Eqs. (1.48) and (1.66) and Fig. 1.3 it is clear that $[J_0'(X)]^2 < 1$ and $[J_1'(X)]^2 < 1$. In consequence, for $q/N > 10^{-11}\,\mathrm{m}$ the expression enclosed in (1.90) by braces differs from 1 by less than 3%. In the magnetospectroscopic experiments discussed in the subsequent chapters of this dissertation, the above requirement was always satisfied, since the probed range of q extended from $10^6\,\mathrm{m}^{-1}$ to $10^8\,\mathrm{m}^{-1}$ and the 2DEG density, N, was never lower than $10^{15}\,\mathrm{m}^{-2}$. Therefore in what follows we will be always assuming that:

$$\Omega_2^2 \simeq \frac{2Ne^2 J_1^2(X)}{\varepsilon_0 \varepsilon_s m X^2} q + \omega_c^2. \tag{1.91}$$

The solid blue curves in Fig. 1.5 demonstrate the accuracy of this approximation for the mentioned range of q and $N = 10^{17}\,\mathrm{m}^{-2}$. As can be seen, they nicely reproduce the strict results given by (1.90).

Careful inspection of Eq. (1.84) leads to conclusion that (1.91) represents one of two possible solutions to the equation:

$$\frac{2\varepsilon_0 \varepsilon_s \omega}{q} - \frac{\alpha\omega}{X^2} \frac{J_1^2(X)}{\omega^2 - \omega_c^2} = 0 \tag{1.92}$$

which can be obtained by equating with 0 the terms surrounded in (1.84) by the first pair of parentheses ($\omega = 0$ is the second solution). This fact suggests that under the above-mentioned conditions

$$\frac{2\varepsilon_0 \varepsilon_s \omega}{q} + i\sigma_{xx} = 0 \tag{1.93}$$

is a good approximation to the general form of dispersion relation described by (1.82). In plasma physics such an approximation is usually called *quasi-static* or *quasi-electrostatic* since, as will be discussed in the next subsection, it completely neglects the transverse (electromagnetic) component of the field associated with magnetoplasma oscillations [9]. It is also worth noticing that if we replace the $J_1(X)$ Bessel function in (1.91) with its asymptotic expansion: $J_1(X) \simeq X/2$ (refer to Eq. (1.53)), valid for $X \ll 1$ (i.e. in the so-called local limit), we will get:

$$\Omega_2^2 \simeq \frac{Ne^2 q}{2m\varepsilon_0 \varepsilon_s} + \omega_c^2 = \omega_p^2 + \omega_c^2, \tag{1.94}$$

where we have introduced a two-dimensional plasma frequency:

$$\omega_p = \left(\frac{Ne^2q}{2m\varepsilon_0\varepsilon_s}\right)^{1/2}, \tag{1.95}$$

derived for the first time by F. Stern [35]. The magnetoplasmon mode described by Eq. (1.94) is known in the literature as the upper hybrid mode (UHM). Its frequency is higher than the frequency of plasma oscillations propagating in the absence of a magnetic field, since on a macroscopic level, the Lorentz force acting on carriers that form a plasma can be simply regarded as an additional restoring force [9]. Model curves that result from Eq. (1.94) are drawn in Fig. 1.5 in red. They approach the results given by Eqs. (1.90) and (1.91) at high magnetic fields, since only then the requirement $X \ll 1$ can be satisfied, as it is clear from the definition of the non-local parameter X (see Eq. (1.33)).

It should be emphasized here that relations (1.93) and (1.94) are correct only in the case of magnetoplasma waves propagating perpendicularly to the applied magnetic field, as we have assumed when deriving the final form of the magnetoconductivity tensors for the three- and two-dimensional electron gas. In magnetooptics, such conditions are usually referred to as the Voigt configuration. A comprehensive discussion on two other common configurations (the Faraday configuration and the so-called oblique one) can be found, for instance, in the canonical paper by E. D. Palik and J. K. Furdyna [36].

Since in the remaining part of this dissertation, we will consider Eq. (1.93) as a basis for magnetospectroscopic data analysis, in the next subsection we would like to discuss in more detail its physical interpretation and the most important effects it predicts.

1.3.2 Physical interpretation

In the absence of an external magnetic field, plasma waves are purely longitudinal oscillations of a charge density [6, 37]. This means, in particular, that they have exclusively electrostatic nature. In other words, the knowledge of the electrostatic potential is enough to fully characterize them. Furthermore, since by definition, the rotation of a longitudinal electric field is identically equal to 0, it results from Maxwell's equations that there is no propagating magnetic field associated with the electrostatic plasma waves. For non-zero magnetic field, the above statements are no longer true. In such a case, expression (1.82) has to be used when searching for possible magnetoplasmon modes. However, as we have seen in the preceding subsection, under quite typical experimental conditions, the spectrum of magnetoplasma excitations that can be obtained with the help of (1.82) is practically the same as the one resulting from Eq. (1.93). We mentioned that the quasi-static approximation it represents, relies on disregarding the transverse (electromagnetic) component of the field associated with a magnetoplasma wave. Now we would like to justify this statement. In order to do that, let us first denote by $\hat{D}$ the matrix operator that acts on the electric-field vector in Eq. (1.81). With its help Eq. (1.93) can be written as $\mathbf{q} \cdot (\hat{D}\mathbf{q})/|\,\mathbf{q}\,|^2 = 0$, where $\mathbf{q} = q\hat{x}$ stands for the magnetoplasmon wave vector and '$\cdot$' should be understood as a scalar product. Thus in fact, all the information stored in (1.93) concerns only the longitudinal (purely electrostatic) component of the field associated with magnetoplasma oscillations. Since from the viewpoint of Maxwell's equations, 'electrostatic' and 'longitudinal' means the same, Eq. (1.93) can equally well be called the longitudinal-wave approximation, but this name is rather rarely met in the literature of the subject.

Having explained the use of Eq. (1.93) instead of a full dispersion relation given by (1.82), we can now analyse in detail its properties. In order to do so, let us first numerically solve it for the case, when the infinite series of non-local corrections to the magnetoconductivity tensor of a 2DEG is limited to the first three terms[6], i.e.:

$$1 - 4\frac{\omega_p^2}{X^2}\sum_{n=1}^{3}\frac{n^2 J_n^2(X)}{\omega^2 - (n\omega_c)^2} = 0, \tag{1.96}$$

where as so far, we have utilized the collisionless form of expression for σ_{xx}. By means of straightforward algebraic manipulations, the above equation can be rewritten as:

$$C_6\omega^6 + C_4\omega^4 + C_2\omega^2 + C_0 = 0,$$

where:

$$\begin{aligned}
C_6 &= 1,\\
C_4 &= -14\omega_c^2 - 4\frac{\omega_p^2}{X^2}\left\{J_1^2(X) + 4J_2^2(X) + 9J_3^2(X)\right\},\\
C_2 &= 49\omega_c^4 + 4\frac{\omega_p^2\omega_c^2}{X^2}\left\{13J_1^2(X) + 40J_2^2(X) + 45J_3^2(X)\right\},\\
C_0 &= -36\omega_c^6 - 144\frac{\omega_p^2\omega_c^4}{X^2}\left\{J_1^2(X) + J_2^2(X) + J_3^2(X)\right\},
\end{aligned}$$

and the range of ω excludes: ω_c, $2\omega_c$ and $3\omega_c$. Solutions of Eq. (1.96) are depicted in Fig. 1.6 with open circles. They were obtained for $q = 10^7\,\mathrm{m}^{-1}$, $N = 10^{17}\,\mathrm{m}^{-2}$, and material parameters corresponding to GaN: $\varepsilon_s = 9.28$ and $m = m^* = 0.22m_0$. Solid red curve represents the magnetic field dependence of the UHM calculated in the local limit, i.e. for $X \ll 1$, and described by Eq. (1.94). Solid blue lines labelled:

---

[6] Keeping the first three terms of the non-local correction series is enough to display all the important features related to $\mathbf{q}$-dependence of the magnetoconductivity tensor that affect the spectrum of magnetoplasma excitations.

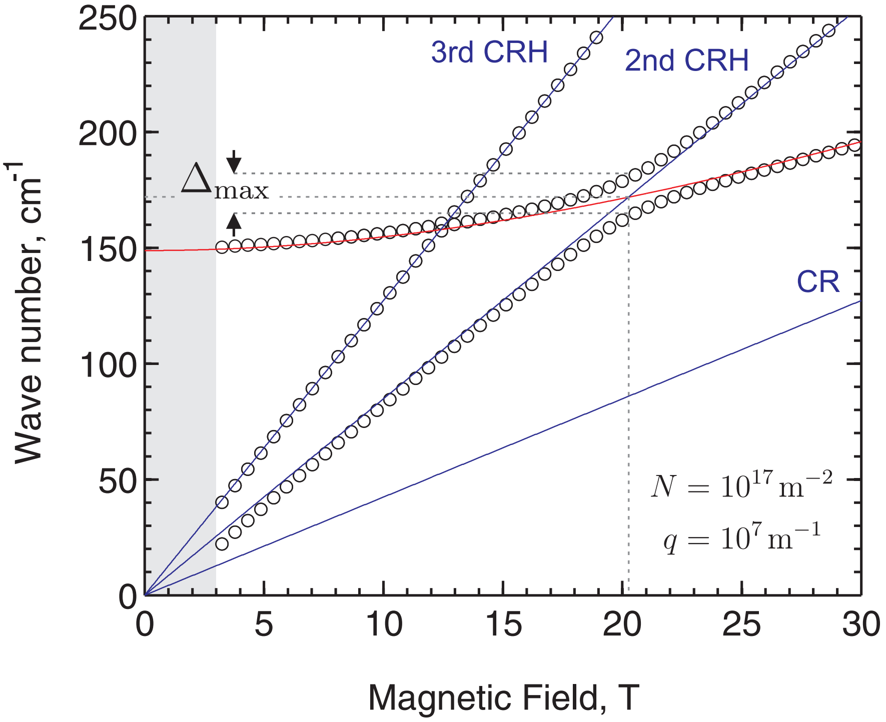

Figure 1.6: Solutions of the non-local dispersion relation in the quasi-static approximation (open circles) plotted as a function of magnetic field for $q = 10^7\,\text{m}^{-1}$, $N = 10^{17}\,\text{m}^{-2}$ and the series of non-local corrections to the magnetoconductivity tensor of a 2DEG limited to the first three terms (refer to Eq. (1.96)). The area marked in grey denotes the magnetic-field range for which (1.96) becomes insufficient approximation to the general form of dispersion relation given by Eq. (1.82). Solid red curve represents the magnetic field dependence of the upper hybrid mode in the local limit. Solid blue lines labelled: 'CR', '2nd CRH' and '3rd CRH' show the magnetic field dependence of the cyclotron frequency and its two first harmonics.

'CR', '2nd CRH' and '3rd CRH' show the magnetic field dependence of the cyclotron frequency and its first two harmonics - the second and third, respectively. Finally, the area marked in grey denotes the range of magnetic field for which Eq. (1.96) becomes insufficient approximation to the general form of dispersion relation given by (1.82). The breakdown of its validity results from too small number of terms of the non-local correction series it contains. The way of translating this number into the critical magnetic field, below which equations similar to (1.96) cannot be used, will be discussed at the end of the present chapter.

There are two important results displayed in Fig. 1.6: the appearance of well developed splittings of the UHM in the vicinity of points at which it crosses the harmonics of the cyclotron resonance (CR) in the local limit[7] and the presence of additional

---

[7] The splitting at 20.18 T denoted by Δ_{max} is indisputable. Similar, but much weaker one appears at 12.43 T, close to the point at which the local UHM crosses the third harmonic of the CR. It becomes clear upon sufficient magnification of the graph.

solutions to the dispersion relation, which closely follow the CR harmonics everywhere except for the splitting regions mentioned above. Their frequencies, however, remain different from $2\omega_c$ and $3\omega_c$ in the whole range of magnetic field, as can easily be verified by directly substituting these two values into the polynomial equation derived from (1.96). These solutions represent the electrostatic waves that, like the UHM, propagate in a magnetized plasma across the magnetic field. It should not be surprising since such modes are the only ones we can investigate with the help of Eq. (1.93). Their propagation is generally limited to narrow passbands around the cyclotron harmonic frequencies and can occur only with wavelengths that are short in comparison with a Thomas-Fermi length (or a Debye length in the case of gaseous plasmas). From the physical point of view they are very similar to 'standard' magnetoplasma oscillations. The only difference is that a restoring force which drives them mostly originates from the Lorentz force. Therefore, unlike the UHM, they disappear in the $B \to 0$ limit, as clearly shown in Fig. 1.6. It is also worth mentioning that except for the splitting regions discussed above, their amplitudes are very small [38]. Because of this fact, it is really challenging to extract the traces of their excitation from the spectra recorded at frequencies which are far from the frequency of the UHM. Such waves are known as Bernstein modes (BMs), named after I. B. Bernstein who was the first to describe them mathematically [39]. Since his pioneer work, BMs have attracted much attention from both the theoretical and the experimental point of view. In particular, they have been extensively studied in classical gaseous plasmas (see [40–44] for a review). In the case of a solid state plasma, both the semi-classical [12, 15, 45, 46] and the quantum-mechanical [8, 38, 47–51] treatment of their occurrence and propagation has been developed and the majority of predicted effects have been confirmed experimentally [3, 52–68], but exclusively for high-quality GaAs-based semiconductor structures. Up to the best knowledge of the author, the results that will be presented later on in this dissertation are the first report on the observation of BMs in GaN/AlGaN heterostructures.

Knowing that beside the UHM, also the BMs can be excited in an electron gas under consideration, the splitting regions shown in Fig. 1.6 might be equivalently viewed as resulting from the interaction between the UHM and the respective BMs. In order to understand the origin of this interaction we shall return to the derivation of the magnetoconductivity tensor of a 3DEG and an auxiliary function $G(X, \vartheta, \phi)$ that we introduced at the intermediate stage of calculation to reduce the complexity of subsequent expressions (see Eq. 1.36). In the case of a 2DEG, this function acquires a simpler form:

$$G(X, \phi) = \int_0^\infty \mathrm{d}s \exp\left\{-i\left[X \sin\left(\omega_c s - \phi\right) - \omega s\right] - \frac{s}{\tau}\right\}, \tag{1.97}$$

which, by making use of relation (1.38), can further be transformed into:

$$G(X,\phi)=\sum_{n=-\infty}^{\infty}J_n(X)\exp\left(in\phi\right)\int_0^{\infty}\mathrm{d}s\exp\left\{-i(n\omega_c-\omega)s-\frac{s}{\tau}\right\}. \tag{1.98}$$

Disregarding for a while the integration over all possible periods of time denoted by s, the interpretation of the above formula is the following: it represents a spectral decomposition of a damped harmonic wave propagating at a frequency ω and with a wave vector q (hidden in the non-local parameter X) into a series of damped harmonic waves propagating with the same wave vector as the original wave, but at frequencies equal to the integer multiples of the cyclotron frequency. Each of these waves is additionally weighted by $J_n(X)\exp(in\phi)$. As displayed by Eq. (1.24), the original wave subjected to decomposition is directly related to the electric field associated with the electromagnetic radiation exciting the magnetoplasma waves in an electron gas under consideration. Let us assume the frequency of this radiation to be always close to the frequency of the UHM. Now, if look at a magnetic-field range for which the UHM approaches an l-th harmonic of the CR, we will immediately see that the l-th component of the above series becomes predominant, what from the viewpoint of Eq. (1.58) indicates a resonant transfer of energy between the UHM and the l-th Bernstein mode and vice versa.[8] It is realized via the electrostatic interaction whose strength is governed by the $J_l(X)$ function and for small l, $q<10^8\,\mathrm{m}^{-1}$ and $N\leqslant 10^{17}\,\mathrm{m}^{-2}$ decreases with l, as clearly shown in Fig. 1.7. Since under such circumstances the UHM and the BM can be regarded as coupled harmonic oscillators, the modes that characterize them in the non-interaction conditions are no longer the eigenmodes of the system and, as

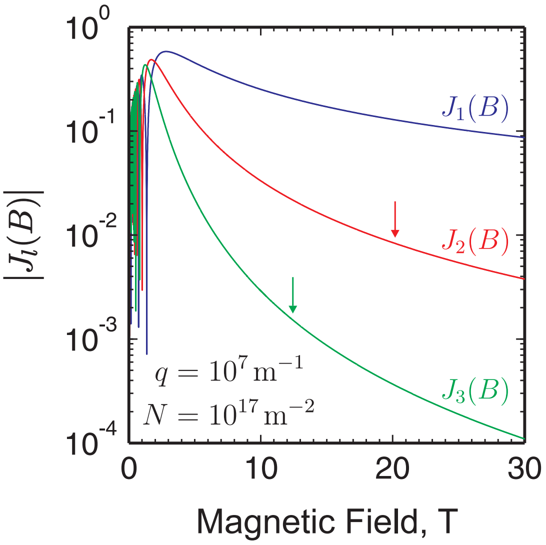

Figure 1.7: Absolute value of the Bessel functions relevant to analysis of the interaction's strength between the UHM and the first two BMs, plotted versus magnetic field for $N = 10^{17}\,\mathrm{m}^{-2}$, $q = 10^7\,\mathrm{m}^{-1}$ and the non-local parameter X given by Eq. (1.33) with the Fermi velocity computed on the basis of Eq. (1.59). Vertical arrows denote the magnetic field values at which the strongest interaction between the UHM and respective BMs occur for the parameters used in calculations (refer to Fig. 1.6).

---

[8] Alternatively, one can also consider this process as sharing the energy of incoming radiation between the UHM and the l-th Bernstein mode, which are being simultaneously excited under the resonant conditions.

a result, the anti-crossing behaviour of the respective dispersion curves occur. On a quantum-mechanical ground, the interaction between the UHM and the BM can be explained by the fact that they are both excitations of the same symmetry (longitudinal magnetoplasma oscillations propagating across the magnetic field), and as such satisfy the Wigner-von Neumann non-crossing rule for the potential curves [69], to the group of which the dispersion curves like those shown in Fig. 1.6 can also be classified (very instructive and clearly presented discussion on the Wigner-von Neumann theorem and its various proofs can be found in [70]).

So far in this section we have mainly examined the importance of the frequency matching in bringing the UHM and a given BM into interaction. Now, we would like to discuss in more detail the role played by their wave vectors or, equivalently, the characteristic scales of their space variation. As a representative example, let us consider the interaction of the UHM with the BM propagating in an electron gas at the frequency close to $2\omega_c$. According to the conclusions from the preceding paragraph, the strength of this interaction is determined by $J_2(X)$ Bessel function. From its graph depicted in Fig. 1.3 we expect the strongest effect to occur for $X \approx 3.1$, an argument corresponding to the first maximum of $J_2(X)$. Recalling that $X = qR_c = 2\pi R_c/\lambda$, where q (λ) denotes the wave vector (wavelength) of the UHM and R_c the cyclotron radius being a typical length-scale for the spatial extent of the BM, we may write:

$$3.1 \approx \frac{2\pi}{\lambda} R_c \Rightarrow \lambda \approx 2R_c. \tag{1.99}$$

It means that in order to observe a strong anti-crossing between the UHM and a given BM, the wavelength of the former should be approximately equal to the cyclotron-orbit diameter. Under such conditions, an individual electron gyrating around the magnetic field lines indeed experiences the strongest influence from the electric field associated with the magnetoplasma oscillations. This effect is very nicely reproduced by a simple modification of Eq. (1.29):

$$\frac{\mathrm{d}^2}{\mathrm{d}t^2}\begin{pmatrix} x \\ y \end{pmatrix} = \omega_c \begin{pmatrix} -\left(e\Sigma_0/m\omega_c\right)\exp\left\{i\left(kx-\omega t\right)\right\} - \mathrm{d}y/\mathrm{d}t \\ \mathrm{d}x/\mathrm{d}t \end{pmatrix}, \tag{1.100}$$

where in addition to the Lorentz force, the motion of an electron is disturbed by the electric field of a harmonic wave propagating across the magnetic field at a frequency ω and with a wave vector k. In the above set of equations Σ_0 denotes the amplitude of an electrostatic wave and the magnetic field is supposed to be directed along the z-axis. Numerical solutions to this problem are presented in Fig. 1.8 for different values of the parameter γ relating the wavelength λ of the electric field to the cyclotron radius:

$$\lambda = \gamma R_c = \frac{2\pi}{X} R_c.$$

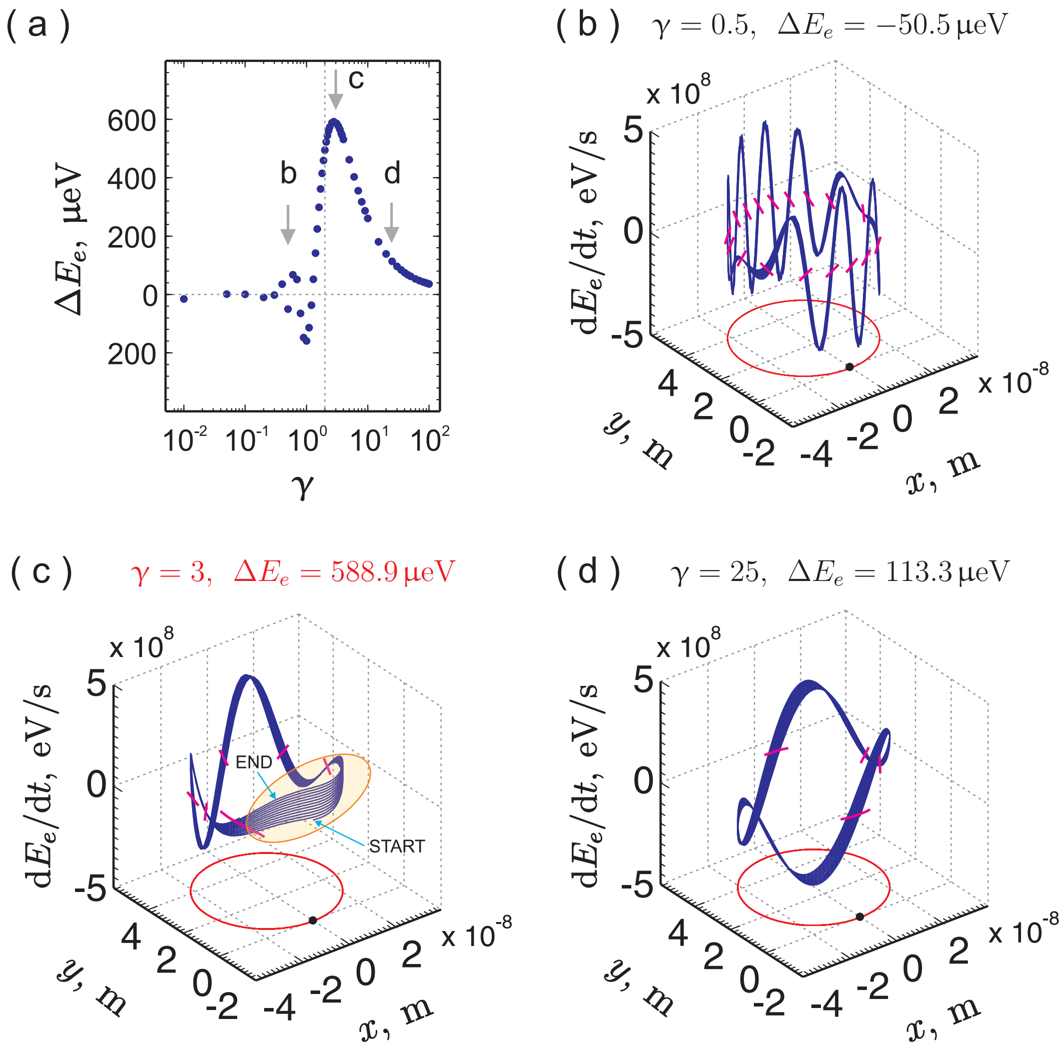

Figure 1.8: (a): Energy acquired during 10 ps by an electron gyrating around the magnetic field lines directed along the z-axis, and subject to an electrostatic wave propagating across the magnetic field (in the x direction), plotted as a function of the parameter γ relating the wavelength of the electric field to the cyclotron radius. Subplots (b), (c) and (d): Trajectory of an electron (red points forming a circle in the x–y plane) and the position-dependent rate of its energy gain/loss (solid blue curves) drawn for three different values of γ corresponding to the left arm, the maximum and the right arm of a bell-shaped curve from the diagram (a), respectively. Black spot on the electrons' trajectory indicates its initial position. Markers drawn in magenta show the points at which the sign of $\mathrm{d}E_e/\mathrm{d}t$ changes.

They were obtained in MATLAB 7.10.0 (R2010a) with the aid of the `ode45` routine for solving ordinary differential equations, based on a hybrid Runge-Kutta algorithm [71,72]. In our simulations we have assumed that: $\Sigma_0 = 10^3\,\mathrm{V/m}$, $m = 0.22m_0$, $B = 20.18\,\mathrm{T}$,[9] and the frequency ω is given by Eq. (1.94) with $q = 10^7\,\mathrm{m}^{-1}$ and $N = 10^{17}\,\mathrm{m}^{-2}$ in order to keep consistency with our previous considerations. The

---

[9] This strength of magnetic field corresponds to the strongest interaction between the UHM and the first BM in Fig. 1.6.

integration of the equations of motion was performed over time ranging from 0 to 10 ps and the initial conditions applied were: $x(0) = y(0) = v_y(0) = 0$ and $v_x(0) = 4.2 \times 10^5\,\mathrm{m/s}$.[10] In Fig. 1.8(a) an energy ΔE_e acquired by an electron from the electrostatic wave during the integration time is plotted versus γ in a semi-logarithmic scale. In accordance with our previous analysis, the functional dependence of ΔE_e on γ has the form of a bell-shaped curve peaked at $\gamma \simeq 3$ (not far away from the condition (1.99)). Figs. 1.8(b), (c) and (d) depict the trajectory of an electron (red points forming a circle in the x–y plane) as well as the position-dependent rate of its energy gain/loss,[11] $\mathrm{d}E_e/\mathrm{d}t$ expressed in eV/s (solid blue curves), in three different cases marked in Fig. 1.8(a) by arrows labelled with appropriate letters. Black spot on the electron's trajectory indicates its initial position. Markers drawn in magenta show the points at which the sign of $\mathrm{d}E_e/\mathrm{d}t$ changes. As can be seen, even though the radius of an electron's orbit and the value of its velocity remain practically unaltered (we have checked that after 10 ps they differ from their initial values by at most 0.25%), the rate of electron's energy gain/loss undergoes a significant qualitative transformation with variation of γ. If $\gamma < 1$, what means that $\lambda < R_c$, an electron accelerates and decelerates many times before completing each turn in the magnetic field. As a result ΔE_e becomes a quickly varying function of time, but of relatively small amplitude. This is exactly the explanation of 'disorder' in the set of points forming a part of the left arm of a bell-shaped curve in Fig. 1.8(a). When we are passing through the resonance ($\lambda \sim 2R_c$), an electron stays almost in-phase with the electric field over a substantial part of its trajectory (see marked in yellow region in Fig. 1.8(c)). Under such conditions, $\mathrm{d}E_e/\mathrm{d}t$ becomes a positive function of time. Moreover, its value increases with each turn completed by an electron gyrating around the magnetic field line, what is schematically denoted in the graph by two arrows labelled with 'START' and 'END'. This phenomenon underlies the interaction between the UHM and the BMs. Finally, apart from the resonance where $\gamma > 3$, the electron's energy gain/loss rate tends towards slowly-varying function of anti-symmetric shape with respect to the position measured along the electron's trajectory. Furthermore, its amplitude continuously decreases with γ. In consequence, ΔE_e approaches progressively 0 and no net effect of the electrostatic wave on the cyclotron motion performed by an electron remains.

In order to summarize our considerations in this section, we would like to present

---

[10] Since throughout this dissertation we will be only dealing with electrons moving at velocities that are small compared to the speed of light, we will completely neglect the emission of electromagnetic radiation, which can in general accompany their motion, but plays an important role only for relativistic particles [73].

[11] From the course of general physics it is known that $\mathrm{d}E/\mathrm{d}t = \mathbf{F} \cdot \boldsymbol{v}$, where $\mathbf{F}$ denotes the force acting on a body and $\boldsymbol{v}$ its velocity. Thus, in our case: $\mathrm{d}E_e/\mathrm{d}t = e\Sigma(x,t)v_x$.

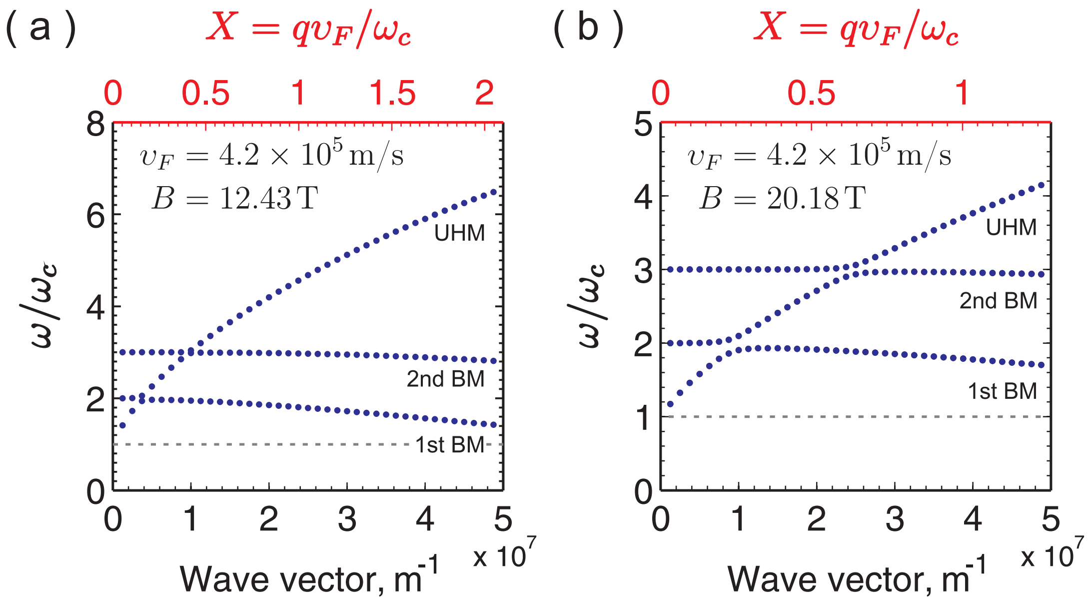

Figure 1.9: Solutions of the non-local dispersion relation in the quasi-static approximation (solid blue circles) plotted as a function of wave vector for a given magnetic field strength and the series of non-local corrections to the magnetoconductivity tensor of a 2DEG limited to the first three terms (refer to Eq. (1.96)). The chosen values of the magnetic field correspond to anti-crossings between the upper-hybrid mode (UHM) and the first two Bernstein modes (BMs) that appear in Fig. 1.6. Diagrams (a) and (b) refer to the interaction of the UHM with the second and the first BM, respectively. Dashed lines drawn in grey represent the cyclotron frequency. Material parameters used in calculations correspond to GaN and are exactly the same as in previous figures.

two more figures showing how different parameters and quantities having relevance for description of the magnetoplasma waves depend on each other. Figure 1.9, which can be regarded as complementary to Fig. 1.6, demonstrates dispersion curves of the UHM and the first two BMs propagating at frequencies close to $2\omega_c$ and $3\omega_c$, plotted in the standard representation relating the characteristic frequency of a given excitation (here expressed in cyclotron frequency units) to its wave vector. Parts (a) and (b) of the figure correspond to the magnetic field values at which the strongest interaction of the UHM with the second and the first BM, respectively, occur in Fig. 1.6. Solid blue circles are numerical solutions of Eq. (1.96) obtained for material parameters corresponding to GaN, which have been quoted several times up to now (the same holds for the Fermi velocity calculated with the aid of Eq. (1.59)). Dashed lines drawn in grey locate the CR on the respective diagrams.

One of the most pronounced features displayed in Fig. 1.9 is the square-root-like dependence of the UHM on its wave vector. Moreover, we can see that for the same range of wave vector variation, changes in the energy of the UHM are significantly greater than in the case of BMs. In accordance with Fig. 1.6, the anti-crossings discussed in the preceding paragraphs occur for $q = 10^7\,\mathrm{m}^{-1}$ at appropriate magnetic field values.

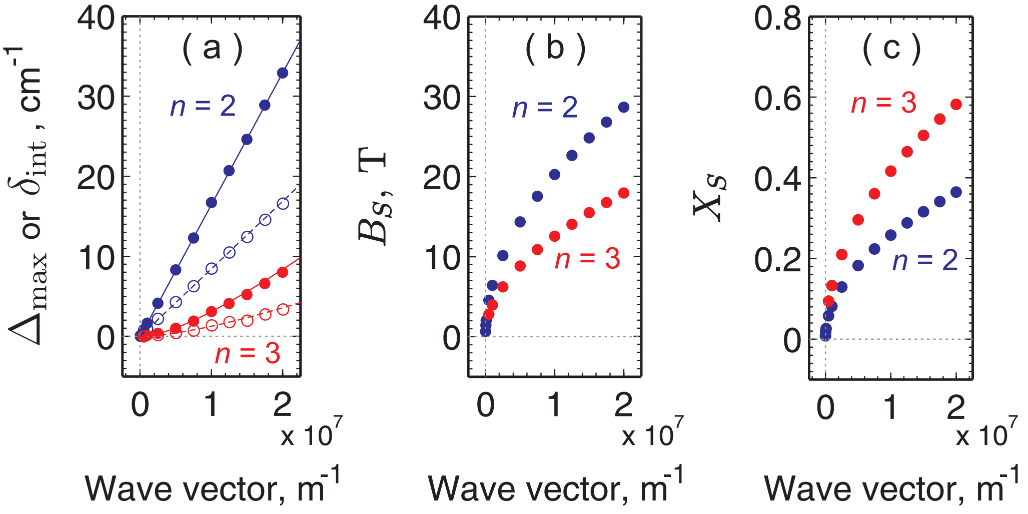

Figure 1.10: Wave-vector dependences of: (a, solid circles) - the maximal splitting of the UHM ($\Delta_{\max}$) due to its interaction with BMs propagating at frequencies close to $2\omega_c$ (blue symbols) and $3\omega_c$ (red symbols); (a, open circles) - the frequency δ_{int} characterizing the energy of interaction between the UHM and the respective BMs; (b) the magnetic field B_S at which the strongest interaction of the UHM with the first BM (solid blue circles) and the second BM (solid red circles) occur; (c) the non-local parameter X_S corresponding to the strongest anti-crossings between the UHM and the first two BMs: the lower-energy one marked in blue and the higher-energy one depicted in red.

Fig. 1.10 shows the wave-vector dependence of various parameters describing the strength of the interaction between the UHM and the BMs as well as the magnetic field range for which it can occur. $\Delta_{\max}$ has been introduced in Fig. 1.6. Here it denotes the maximal splitting of the UHM due to interaction with both the first and the second BM and in diagram (a) is depicted with solid blue and red circles, respectively. Each of these points was derived directly from graphs similar to Fig. 1.6, but plotted for an appropriate wave vector q. δ_{int} characterizes the energy of the strongest interaction between the UHM and the BMs, expressed in cm^{-1} (we would like to remind that $1\,\text{cm}^{-1} \simeq 0.188\,\text{THz} \sim 0.124\,\text{meV}$). In order to calculate it, we have made a standard assumption that under mode-mixing conditions, a Hamiltonian $\mathcal{H}$ describing the system of two coupled excitations (the UHM and the given BM in our case) can be written in the form:

$$\mathcal{H} = \hbar \begin{pmatrix} \omega_{\text{UHM}} & \delta_{\text{int}} \\ \delta_{\text{int}} & \omega_{\text{BM}} \end{pmatrix}, \tag{1.101}$$

where ω_{UHM} and ω_{BM} denote the frequencies of the UHM and the BM, respectively, and δ_{int} is supposed to be a real number. On one hand, the eigenenergies of $\mathcal{H}$: $\hbar\omega_+$ and $\hbar\omega_-$ can be obtained by solving a secular equation associated with (1.101). On the other hand, they might be directly red from a graph similar to Fig. 1.6. At magnetic field B_S corresponding to the strongest interaction between the UHM and the BM, ω_+ and ω_- satisfy the relation:

$$\hbar(\omega_+ - \omega_-) = \hbar\Delta_{\mathrm{max}}.$$

With its help the frequency δ_{int} may be expressed as:

$$\delta_{\mathrm{int}} = \frac{1}{2}\Big\{\Delta_{\mathrm{max}}^2 - \left[\omega_{\mathrm{UHM}}(q, B_S) - n\omega_c(B_S)\right]^2\Big\}^{1/2}, \tag{1.102}$$

where we have replaced ω_{BM} with $n\omega_c$ and explicitly indicated that B_S should be used in calculation of both frequencies. The wave-vector dependence of δ_{int} is depicted in Fig. 1.10(a) with open blue and red circles that are related to the interaction of the UHM with the first ($n = 2$) and the second ($n = 3$) BM, respectively. As can be seen, in the first case both Δ_{max} and δ_{int} vary linearly with q belonging to the range of interest for this dissertation. On the other hand, a power-law shape of the q-dependence, slightly faster than the linear increase, occurs for Δ_{max} and δ_{int} in the second case. Moreover, in contrast to the strongest anti-crossing observed for the UHM interacting with the first BM, B_S for the analogical anti-crossing corresponding to the second BM does not exactly match the magnetic field at which the local magnetoplasmon dispersion curve crosses the second harmonic of the CR. It becomes clear upon sufficient magnification of the data presented in Fig. 1.6. Figs. 1.10(b) and (c) display the variation with q of the magnetic field B_S and the non-local parameter X_S. Since by definition of the latter:

$$B_S(q)X_s(q) \sim q,$$

both $B_S(q)$ and $X_S(q)$ must be functions of the power-law type, characterized by exponents a and b that satisfy the relation $a + b = 1$. By combining them with the results presented in Fig. 1.8(a), a progressive increase in Δ_{max} and δ_{int} shown in Fig. 1.10(a) can be explained as originating from tuning the system composed of the UHM and a given BM towards resonance conditions from the long-wavelength (large γ) side.

1.4 Magnetoplasma oscillations in real semiconductor structures

When deriving the magnetoconductivity tensor of a 3DEG and 2DEG, we considered electrons as suspended in vacuum or immersed in a jelly of positive charge ensuring the system an electrical neutrality. Next, in the discussion on the dispersion relation of two-dimensional magnetoplasmons, we introduced a static dielectric constant characterizing the long-wavelength polarizability of the medium surrounding the 2DEG layer. We did not specify, however, the microscopic structure of this medium and did not raise the question about its influence on the optical as well as magneto-transport properties of an electron system under analysis. Finally, in most of the numerical examples presented so far, we replaced the free-electron mass m_0 with the mass $m^* = 0.22m_0$ corresponding to epitaxial GaN, but we did not comment on the validity of such a substitution. Now, we would like to clarify and systematize these issues.

1.4.1 The role of band-structure effects

Charge carriers in crystalline solids are subject to periodic electrostatic potential of ions forming a crystal lattice, which depending on the material may exhibit a short- or long-range ordering. This potential modifies their wavefunctions and the spectrum of allowed energy states organized into bands instead of discrete set of levels as in the case of isolated atoms. In condensed matter physics, these effects are usually described within the framework of the band theory [74]. It provides many powerful tools for dealing with the crystalline surrounding of an electronic system under analysis. One of them is the effective-mass approximation, which enables to encode the band structure details into a mass m^* replacing the free-electron mass in all expressions it appears in [75]. The effective mass has in general a tensor form which reduces to a single scalar value only in the case of carriers occupying an isotropic band of parabolic symmetry, for which the relationship between the carrier's energy E and momentum $\hbar\mathbf{k}$ reads: $E(\mathbf{k}) = \hbar^2 k^2/2m^*$. Although being a crude approximation to the complex band structure, using a scalar effective mass instead of its complete tensor representation works surprisingly well for numerous semiconductor structures. In particular, it provides a very good description of many optical and transport phenomena in GaN of the hexagonal symmetry, for which precise measurements [27–33] have shown that the cyclotron resonance effective mass of the conduction band electrons is close to $0.22m_0$ and practically does not change with a dimensionality of the electron gas, i.e. is almost the same for bulk samples, epitaxial layers, hetero- and quantum-well structures. It may vary, however, with the electron gas concentration and in the case of doped samples based on the GaN/AlGaN heterostructure, in which the areal number of electrons can be an order of magnitude higher than in samples containing a 2DEG that originates exclusively from the spontaneous and piezoelectric polarization [76–79], this effect should definitely be taken into account [31]. Thus, whenever the mass of electrons will be called in the remaining part of this dissertation, it should be understood as the effective mass of the conduction band electrons in GaN, equal to or higher than $0.22m_0$ - the value determined from the cyclotron resonance measurements performed on 2DEGs of low and moderate density.

1.4.2 Dielectric function of multilayer semiconductor structures

In the discussion on the magnetoconductivity tensor of a 2DEG and derivation of the dispersion relation of 2D magnetoplasma oscillations, we have silently assumed that the 2DEG layer simply exists and is surrounded by a dielectric medium, which long-wavelength polarizabilty is characterized by a static dielectric constant ε_s. Real systems are, however, much more complicated. A quasi-two-dimensional electron gas can only be formed in quantum wells or heterostructures [80,81]. Since all the samples investigated within this thesis belonged to the latter group, we will entirely focus on it in the remaining part of the text.

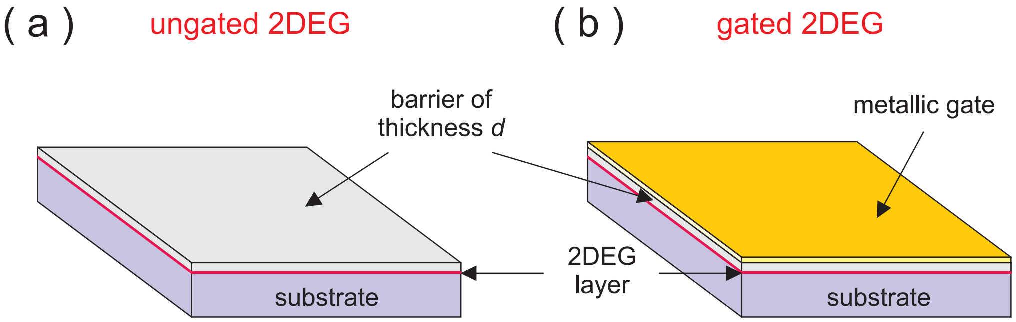

Figure 1.11: A scheme of a typical heterostructure: (a) not providing an electrical control over the 2DEG density, and (b) equipped with a metallic gate that allows to change the concentration of a 2DEG by applying an external voltage. The substrate and barrier layers should be understood as layers made out of semiconductors with smaller and larger energy gap, respectively.

A diagram showing the layout of a typical heterostructure is presented in Fig. 1.11(a). It consists of a relatively thick substrate layer made out of semiconductor with smaller energy gap (e.g., GaN) and a barrier layer being a thin film of semiconductor with larger energy gap (e.g., $\mathrm{Al_{0.2}Ga_{0.8}N}$). The first layer should not be confused with the substrate on which the growth of real heterostructures is carried out in a reaction/deposition chamber.[12] A 2DEG marked in magenta is confined to the interface between the substrate and barrier layers. Except for methods based on the illumination with light of the above-band-gap energy, application of pressure or variation of temperature, the heterostructure in Fig. 1.11(a) does not provide any convenient way of changing the concentration of a 2DEG. This is an important disadvantage in many practical applications. Therefore, heterostructures similar to the one depicted in Fig. 1.11(b) are often preferred. As can be seen, they contain an additional layer deposited on top of a barrier and made out of a highly conductive metal.

---

[12] The growth of GaN/AlGaN heterostructures is usually performed on sapphire or silicon substrates.

When electrically polarized, such a layer, usually referred to as the gate, allows to control the concentration of the 2DEG in a fairly wide range, which typically covers one or two orders of magnitude [22, 82, 83].

The task of deriving the rigorous dispersion relation for 2D plasma oscillations in a three-layer system that can be used to model both types of heterostructures from Fig. 1.11, was undertaken for the first time by M. Nakayama [84]. After performing an electrodynamic analysis being a more general version of our considerations presented in paragraph 1.3.1, he obtained the following formula:

$$\frac{\left(\varepsilon_{\mathrm{g}(0)}/\beta_{\mathrm{g}(0)}+\varepsilon_{\mathrm{b}}/\beta_{\mathrm{b}}\right)\left(\varepsilon_{\mathrm{sub.}}/\beta_{\mathrm{sub.}}+\varepsilon_{\mathrm{b}}/\beta_{\mathrm{b}}-\sigma/i\varepsilon_0\omega\right)}{\left(\varepsilon_{\mathrm{g}(0)}/\beta_{\mathrm{g}(0)}-\varepsilon_{\mathrm{b}}/\beta_{\mathrm{b}}\right)\left(\varepsilon_{\mathrm{sub.}}/\beta_{\mathrm{sub.}}-\varepsilon_{\mathrm{b}}/\beta_{\mathrm{b}}-\sigma/i\varepsilon_0\omega\right)}=\exp\left(-2\beta_{\mathrm{b}}d\right), \tag{1.103}$$

where the subscripts $\alpha = \{\mathrm{sub.}, \mathrm{b}, \mathrm{g}(0)\}$ refer to the substrate layer, the barrier layer of thickness d and the metallic gate (or vacuum in the case of ungated heterostructure), respectively, ε_α denotes the static dielectric constant of a given layer, β_α is defined by Eq. (1.83), ω has the usual meaning and σ stands for the DC conductivity of a 2DEG (or the respective component of a conductivity tensor in problems involving an anisotropy of the conduction band or the presence of a magnetic field). By making use of analogical approximations as discussed by us when deriving the dispersion relation of 2D magnetoplasmons, it can be shown that the above equation yields the following expression for the characteristic frequency of 2D plasma oscillations [85–87]:

$$\omega_p^2(d;q)=\frac{Ne^2q}{2m^*\varepsilon_0\varepsilon_{\mathrm{eff}}(qd)}, \tag{1.104}$$

where the effective dielectric function $\varepsilon_{\mathrm{eff}}(qd)$ reads:

$$\varepsilon_{\mathrm{eff}}(qd)\equiv\varepsilon_{\mathrm{ug}}(qd)=\frac{\varepsilon_{\mathrm{sub.}}}{2}+\frac{\varepsilon_{\mathrm{b}}}{2}\cdot\frac{1+\varepsilon_{\mathrm{b}}\tanh(qd)}{\varepsilon_{\mathrm{b}}+\tanh(qd)} \tag{1.105}$$

for the ungated 2DEG and:

$$\varepsilon_{\mathrm{eff}}(qd)\equiv\varepsilon_{\mathrm{g}}(qd)=\frac{\varepsilon_{\mathrm{sub.}}+\varepsilon_{\mathrm{b}}\coth(qd)}{2} \tag{1.106}$$

in the case of gated 2DEG. For most of the semiconductor heterostructures $\varepsilon_{\mathrm{b}} \approx \varepsilon_{\mathrm{sub.}} \sim 10$. Taking this into account and assuming that $\varepsilon_{\mathrm{sub.,b}} \gg 1$ (which obviously represents a very crude approximation) allows one to rewrite Eqs. (1.105) and (1.106) in the symmetrical form:

$$\varepsilon_{\mathrm{ug}}(qd)\simeq\frac{\varepsilon_{\mathrm{b}}}{2}\left(1+\tanh(qd)\right),$$

$$\varepsilon_{\mathrm{g}}(qd)\simeq\frac{\varepsilon_{\mathrm{b}}}{2}\left(1+\coth(qd)\right),$$

frequently found in the literature of the subject. Less controversial and much more important from the application point of view is the long-wavelength approximation

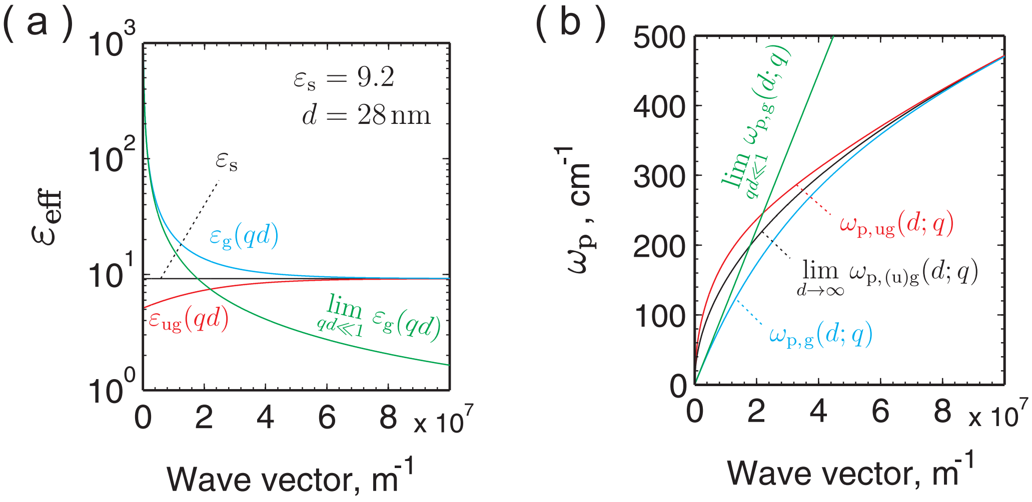

Figure 1.12: (a) Wave-vector dependence of the effective dielectric function of the unagted (red curve labelled with '$\varepsilon_{\rm ug}(qd)$') and gated 2DEG (cyan curve labelled with '$\varepsilon_{\rm g}(qd)$') and the long-wavelength approximation to the latter one (green curve labelled with '$\lim_{qd\ll 1} \varepsilon_{\rm g}(qd)$'). Black line represents the static dielectric constant $\varepsilon_{\rm s}$ of the substrate layer. (b) Dispersion curves calculated with the use of the effective dielectric functions displayed in diagram (a). Black curve labelled with '$\lim_{d\to\infty} \omega_{\rm p,(u)g}(d;q)$' refers to $\varepsilon_{\rm s}$.

to the function $\varepsilon_{\rm g}(qd)$. If $qd \ll 1$, by making use of Taylor expansion, $\coth(qd)$ can be expressed as: $\coth(qd) \approx 1/qd$. With the aid of this formula, Eq. (1.106) becomes: $\varepsilon_{\rm g}(qd) \approx \varepsilon_{\rm b}/2qd$, since under the above conditions $\varepsilon_{\rm b}/qd \gg \varepsilon_{\rm sub.}$. Finally, when inserted into (1.104), the latter result leads to:

$$\omega_p^2(d;q) \approx \frac{Ne^2dq^2}{m^*\varepsilon_0\varepsilon_{\rm b}} \quad \Rightarrow \quad \omega_p(d;q) \approx \sqrt{\frac{Ne^2d}{m^*\varepsilon_0\varepsilon_{\rm b}}}q, \tag{1.107}$$

what means that in the long-wavelength limit, the 2D plasma oscillations are essentially the same as acoustic waves, described by a linear dispersion relation. Moreover, as clearly displayed by Eq. (1.107), the phase velocity of 2D plasmons in gated heterostructures, can easily be tuned by the electric potential $V_{\rm g}$ applied to the gate electrode, since in accordance with our previous discussion $N = N(V_{\rm g})$. This creates the possibility of fabricating resonant detectors, emitters and modulators of THz and sub-THz radiation[13], which has already been demonstrated on many semiconductor systems including GaN-based devices [88–97].

In Fig. 1.12 we graphically summarize our considerations presented so far in this paragraph. Diagram (a) shows the wave-vector dependence of the effective dielectric function of the unagted (red curve labelled with '$\varepsilon_{\rm ug}(qd)$') and gated 2DEG (cyan

---

[13] According to the scale of frequency axes in the graphs presented by far in this dissertation, the energy of plasma oscillations in 2D semiconductor structures corresponds to the THz range of electromagnetic radiation.

curve labelled with '$\varepsilon_\mathrm{g}(qd)$') as well as the long-wavelength approximation to the latter one (green curve labelled with '$\lim_{qd\ll 1}\varepsilon_\mathrm{g}(qd)$'). For the sake of completeness, with the black line labelled ε_s, we have also drawn the static dielectric constant of the substrate (supposed to be made of GaN). When preparing the graph, we assumed that $\varepsilon_\mathrm{sub.}\approx\varepsilon_\mathrm{b}$ and arbitrarily set the thickness of the barrier, d, to be equal to 28 nm. Fig. 1.12(b) presents the dispersion curves calculated with the use of the effective dielectric functions displayed in Fig. 1.12(a) and the same material parameters as utilized several times in this chapter ($N = 10^{17}\,\mathrm{m}^{-2}$ and $m^* = 0.22m_0$). The color code and the labelling format are almost the same for both parts of Fig. 1.12. The only difference lays in '$\lim_{d\to\infty}\omega_{\mathrm{p,(u)g}}(d;q)$' used to denote the dispersion curve calculated for the static dielectric constant ε_s.

As can be seen, for any given wave vector, the frequency of plasma oscillations in 2DEG surrounded by uniform medium extending infinitely in all directions, falls in-between the corresponding frequency in the ungated 2DEG and the frequency of plasma oscillations in gated 2DEG. All three frequencies go to 0 when $q\to 0$ and become identical in the $(q\to\infty)|_{d=\mathrm{const}}$ and $(d\to\infty)|_{q=const}$ limits, since q and d enter the effective dielectric function on equal rights. Finally, for the range of parameters used in calculations, which is quite representative for many semiconductor structures, the long-wavelength approximation to the function $\varepsilon_\mathrm{g}(qd)$ gives satisfactory results for plasma waves characterized by $q\leqslant 6\times 10^6\,\mathrm{m}^{-1}$ ($\lambda\geqslant 1\,\mu\mathrm{m}$).

Having generalised the description of plasma oscillations to the case of 2DEG embedded in a three-layer semiconductor structure, we would like now to analyse the influence of more complex crystalline surrounding on the dispersion relation of 2D magnetoplasma waves. In a simplified version (2DEG sandwiched between two subspaces of different static dielectric constants), this problem was solved for the first time by K. W. Chiu and J. J. Quinn in a way being a straightforward extension of the approach presented by us in paragraph 1.3.1 [8]. They have shown that under the above conditions, Eq. (1.93) takes the form:

$$\frac{2\varepsilon_0\omega}{q}\cdot\frac{\varepsilon_\mathrm{sub.}+\varepsilon_\mathrm{b}}{2}+i\sigma_{xx}=0, \tag{1.108}$$

where marked in blue term replacing ε_s in the original expression is nothing else, but the formula resulting from taking the $d\to\infty$ limit in Eq. (1.105). Hence, in order to obtain a correct description of magnetoplasma oscillations propagating in a 2DEG contained either in a gated or in an ungated heterostructure, we should write:

$$\frac{2\varepsilon_0\varepsilon_\mathrm{eff}(qd)\omega}{q}+i\sigma_{xx}=0. \tag{1.109}$$

Combined with Eq. (1.63), the above relation eventually leads to:

$$1 - \frac{2Ne^2q}{m^*\varepsilon_0\varepsilon_{\text{eff}}(qd)X^2}\sum_{n=1}^{\infty}\frac{n^2J_n^2(X)}{\omega^2-(n\omega_c)^2} = 0, \tag{1.110}$$

or

$$1 - \frac{\omega_{\text{p}}^2(d;q)}{X^2}\sum_{n=1}^{\infty}\frac{4n^2J_n^2(X)}{\omega^2-(n\omega_c)^2} = 0, \tag{1.111}$$

if we make use of Eq. (1.104).

Before moving to the next paragraph, we would like to address one more issue which is directly related to the usefulness of the formulae we have just derived in experimental data analysis. It is clear that there is no possibility of maintaining the infinite series that appears in Eqs. (1.110) and (1.111). It has to be cut at some term and the question arises about the best way of determining that point. As we have seen in Figs. 1.5 and 1.6, the problem with converging to the correct frequency appears for the UHM at low magnetic field and becomes more and more pronounced as the length of the magnetoplasmon wave vector increases. When the magnetic field tends to 0, the relation $\omega \simeq \omega_p(d;q) \gg n\omega_c$ holds for the UHM, and allows to rewrite Eq. (1.111) in the simplified form:

$$\sum_{n=1}^{\infty}\frac{4n^2J_n^2(X)}{X^2} \approx 1.$$

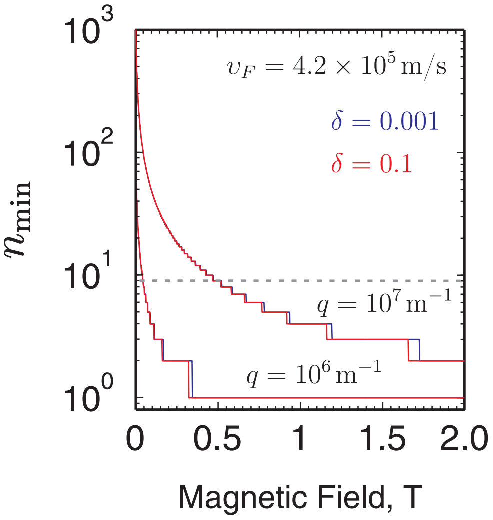

Figure 1.13: Magnetic-field dependence of the minimal number of terms of the non-local correction series that have to be retained in order to reproduce the dispersion curves of 2D magnetoplasma waves, characterized by a wave vector q, with accuracy given by δ.

Thus, for a particular value of the non-local parameter X containing information on both the magnetic field and the wave vector of magnetoplasma oscillations, the task we want to accomplish is equivalent to determining the minimal n that satisfies the above equation with accuracy given by δ:

$$\sum_{n=1}^{n_{\text{min}}}\frac{4n^2J_n^2(X)}{X^2} \geqslant 1-\delta.$$

Fig. 1.13 demonstrates the results of such an analysis performed for two lengths of the magnetoplasmon wave vector ($q = 10^6\,\text{m}^{-1}$ and $q = 10^7\,\text{m}^{-1}$ corresponding to the limits of range accessible in our experiments described in subsequent chapters) and two levels of accuracy: $\delta = 0.001$ (blue curves) and $\delta = 0.001$ (red curves). As can be seen, $n_{\mathrm{min}}(B)$ is a quickly decreasing function of magnetic field, which exhibits very small sensitivity to the accuracy parameter δ but undergoes significant changes with the variation in q. Its staircase shape is, of course, a direct consequence of a discrete nature of Eqs. (1.110) and (1.111). Dashed line drawn in grey depicts in Fig. 1.13 the number of terms of the non-local correction series that we have used when interpreting the results of magnetospectroscopic measurements. The reason for setting n_{min} to be equal to 9 was purely numerical. When programming the routines for automatic data treatment in MATLAB 7.10.0 (R2010a), we realized that for $n_{\mathrm{min}} > 9$, the complexity of polynomial coefficients used to calculate the dispersion curves of 2D magnetoplasma waves leads to instability in execution of the function `roots`, which played a central role in our algorithm [72]. Since overcoming that problem would required a significant interference in part of the native MATLAB's code and had almost no scientific importance, we decided to keep $n_{\mathrm{min}} = 9$ in all final runs of our software. In connection with Fig. 1.13 (see dashed line drawn in grey), it means that for the range of wave vectors probed in our experiments, the numerical predictions of the model we developed in this chapter can safely be applied to magnetic fields as low as $0.5\,\mathrm{T}$ but definitely not lower than $0.05\,\mathrm{T}$.

1.4.3 Plasmon–LO phonon coupling

It is well-known that in polar semiconductors like GaAs or GaN, the propagation of plasma waves is affected by the crystal lattice in a much stronger way than in other materials [23, 98–103]. This state of affairs originates from the coupling between the plasma oscillations and the LO phonons (the longitudinal-optical mode of lattice vibrations). In GaAs, the characteristic energies of these excitations are relatively close to one another. As a result, the plasmon-LO phonon coupling significantly modifies the dispersion relation of plasma and magnetoplasma oscillations. In GaN, the situation looks a little bit different, since the energy separation between the plasma oscillations and the longitudinal vibrations of a crystal lattice is much greater than in the case of GaAs. Nevertheless, the interaction of plasmons or magnetoplasmons with LO phonons should still be taken into account in order to obtain more realistic and complete description of the former ones.

Incorporation of dynamic properties of a crystal lattice into the model of magnetoplasma waves that we have developed so far is quite an easy task, especially for bulk semiconductors, which, like GaAs, crystallize in a zinc-blenede structure (see Fig. 1.14(a)). In such a case, we simply have to replace the static dielectric constant ε_{s} that was introduced in paragraph 1.3.1 with a frequency-dependent dielectric function:

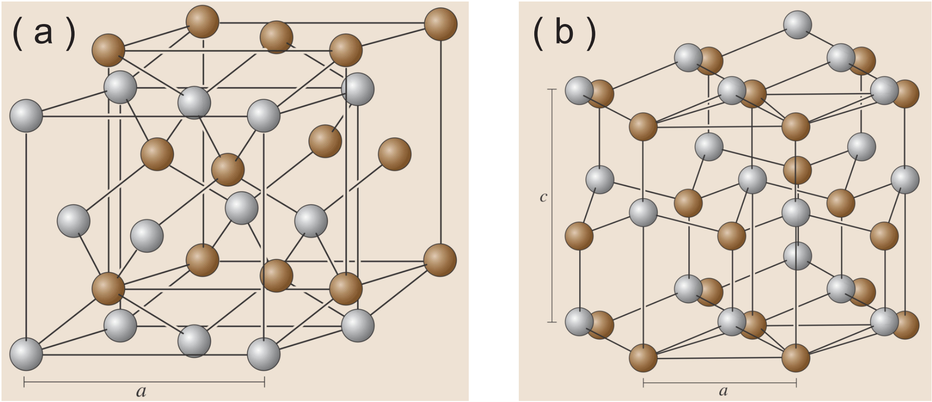

Figure 1.14: Schematic representation of the zinc-blende (a) and hexagonal würzite (b) lattices. Letters a and c denote the respective lattice parameters. Both pictures are taken from [104].

$$\varepsilon(\omega) = \varepsilon_\infty \frac{\omega^2 - \omega_{\mathrm{LO}}^2}{\omega^2 - \omega_{\mathrm{TO}}^2}, \tag{1.112}$$

where ω_{LO} and ω_{TO} denote the frequency of the longitudinal-optical and the transverse-optical mode of lattice vibrations, respectively, and ε_∞ is the high-frequency dielectric constant connected with ε_{s} by the well-known Lyddane-Sachs-Teller relation: $\omega_{\mathrm{LO}} = \sqrt{\varepsilon_{\mathrm{s}}/\varepsilon_\infty}\,\omega_{\mathrm{TO}}$. As can be seen, in the long-wavelength/low-frequency limit, the above expression reduces to ε_{s}. Unlike GaAs, GaN rarely occurs in a zinc-blende structure. Much more naturally for it is to crystallize in a hexagonal würzite structure, which exhibits a uniaxial symmetry (see Fig. 1.14(b)). Under such conditions, the frequency-dependent dielectric function acquires a tensor form:

$$\hat{\varepsilon}(\omega) = \begin{pmatrix} \varepsilon_\perp(\omega) & 0 & 0 \\ 0 & \varepsilon_\perp(\omega) & 0 \\ 0 & 0 & \varepsilon_\parallel(\omega) \end{pmatrix}, \tag{1.113}$$

where $\varepsilon_\perp(\omega)$ and $\varepsilon_\parallel$ refer to directions that are, respectively, perpendicular and parallel to the symmetry axis, usually labelled with c and oriented along the z-direction. By analogy with Eq. (1.112), $\varepsilon_\perp(\omega)$ and $\varepsilon_\parallel(\omega)$ can be expressed as:

$$\varepsilon_\perp(\omega) = \varepsilon_{\infty,\perp} \frac{\omega^2 - \omega_{\mathrm{LO},\perp}^2}{\omega^2 - \omega_{\mathrm{TO},\perp}^2}, \tag{1.114}$$

$$\varepsilon_\parallel(\omega) = \varepsilon_{\infty,\parallel} \frac{\omega^2 - \omega_{\mathrm{LO},\parallel}^2}{\omega^2 - \omega_{\mathrm{TO},\parallel}^2} \tag{1.115}$$

where for GaN: $\varepsilon_{\infty,\perp} = 5.29$, $\varepsilon_{\infty,\parallel} = 5.31$, $\omega_{\mathrm{LO},\perp} = 743\,\mathrm{cm}^{-1}$, $\omega_{\mathrm{TO},\perp} = 561\,\mathrm{cm}^{-1}$, $\omega_{\mathrm{LO},\parallel} = 735\,\mathrm{cm}^{-1}$, and $\omega_{\mathrm{TO},\parallel} = 533\,\mathrm{cm}^{-1}$ [34, 105, 106]. It is worth to mention that 'perpendicular' frequencies listed above are associated with the so-called E_1(LO) and E_1(TO) modes of lattice vibrations, whereas 'parallel' frequencies refer to the modes known as $\mathrm{A_1(LO)}$ and $\mathrm{A_1(TO)}$. Both $\mathrm{E_1(LO,TO)}$ and $\mathrm{A_1(LO,TO)}$ modes are infrared-active in III-V nitrides.

The situation gets further complicated in low-dimensional structures (like GaN/AlGaN heterostructure, for example) due to spatial confinement of the phonon modes [99]. In many cases, however, these effects can be neglected because the relevant phenomena take place along directions which are not affected by any dimensional constrictions. It is particularly true for the samples that have been investigated within the framework of this PhD thesis. As will become clear in the next chapter, the plasma and magnetoplasma waves can propagate in our structures only in the plane perpendicular to the direction of layer stacking which, in additional, coincides with the c-axis orientation in the substrate and barrier layers (made out of GaN and AlGaN of hexagonal würzite structure, respectively). Because of this property, in the remaining part of this dissertation we will be taking into account the coupling of magnetoplasma oscillations with only the $\mathrm{E_1(LO)}$ mode of lattice vibrations in GaN and $\mathrm{Al}_x\mathrm{Ga}_{1-x}\mathrm{N}$ layers. Furthermore, we will assume that due to a relatively low aluminum content in the barrier ($x = 0.2$), its frequency-dependent dielectric function, valid for directions perpendicular to the c-axis, is practically identical with the respective dielectric function of the GaN substrate. This means that, in order to include the plasmon-LO phonon coupling in dispersion relation given by Eq. (1.109), we have to replace the static dielectric constants of the substrate and barrier layers (hidden in the expression for $\varepsilon_{\mathrm{eff}}(qd)$) with dynamic dielectric function described by Eq. (1.114) and calculated for material parameters listed above. Performing so provides the following new versions of Eqs. (1.110) and (1.111):

$$\frac{\omega^2-\omega^2_{\mathrm{LO},\perp}}{\omega^2-\omega^2_{\mathrm{TO},\perp}}-\frac{2Ne^2q}{m^*\varepsilon_0\varepsilon^{\infty,\perp}_{\mathrm{eff}}(qd)X^2}\sum_{n=1}^{\infty}\frac{n^2J_n^2(X)}{\omega^2-(n\omega_c)^2}=0, \tag{1.116}$$

$$\frac{\omega^2-\omega^2_{\mathrm{LO},\perp}}{\omega^2-\omega^2_{\mathrm{TO},\perp}}-\frac{\omega^2_{\mathrm{p},\infty}(d;q)}{X^2}\sum_{n=1}^{\infty}\frac{4n^2J_n^2(X)}{\omega^2-(n\omega_c)^2}=0, \tag{1.117}$$

where

$$\omega^2_{\mathrm{p},\infty}(d;q)=\frac{Ne^2q}{2m^*\varepsilon_0\varepsilon^{\infty,\perp}_{\mathrm{eff}}(qd)} \tag{1.118}$$

and

$$\varepsilon^{\infty,\perp}_{\mathrm{eff}}(qd)=\begin{cases}\dfrac{\varepsilon_{\infty,\perp}}{2}\left(1+\coth(qd)\right), & \text{for gated heterostructures,}\\[2ex] \dfrac{\varepsilon_{\infty,\perp}(\varepsilon_{\infty,\perp}+1)}{2}\cdot\dfrac{1+\tanh(qd)}{\varepsilon_{\infty,\perp}+\tanh(qd)}, & \text{for ungated heterostructures.}\end{cases} \tag{1.119}$$

The last three expressions with the infinite series of non-local corrections to the magnetoconductivity tensor of a 2DEG restricted to the first nine terms will be extensively used in the subsequent chapters to model the experimental data collected in magnetospectroscopic measurements. It is worth to mention that plasma waves described by the frequency $\omega_{\mathrm{p},\infty}(d;q)$ they contain, are known in the literature as the 'high-frequency' ones [9], in contrast to plasma oscillations defined by Eq. (1.104), which do not have any particular nickname.

Chapter 2

Magnetotransport at low and high magnetic fields

In the preceding chapter we have constructed the formal description of magnetoplasmon excitations starting from derivation of the frequency- and wave-vector-dependent magnetoconductivity tensor of an electron gas. Now we would like to take a closer look at static properties of this tensor and discuss how transport parameters it contains (the momentum relaxation time and the density of carriers) can be determined from magnetoresistance measurements. The knowledge about their values will be very important for the comparison between the magnetoplasma dispersion curves we have obtained so far on a theoretical basis, and the results of magnetooptical experiments presented in the remaining part of this dissertation. As it is frequently done in textbooks on condensed matter physics, we will divide our analysis into two parts: the first one referring to the low-magnetic-field range in which the Landau quantization of electrons' motion [22–25] can be neglected, and the second one focused on the high-magnetic-field range in which it plays a predominant role, giving rise to emergence of various effects [107], out of which we will discuss only the Shubnikov-de Haas (SdH) oscillations since they are especially useful for determining the carrier concentration and a so-called quantum relaxation time.

2.1 Low magnetic fields: physical and geometrical magnetoresistance

Let us return to Eqs. (1.60)–(1.62) describing components of the magnetoconductivity tensor, $\hat{\sigma}$, of a 2DEG located in the x–y plane of the Cartesian coordinate system, and subject to an external, time-independent magnetic field oriented along the z-axis, i.e. $\mathbf{B} = B\hat{z}$. In the local approximation followed by taking the static limit ($\omega = 0$) and leaving an assumption about the energy-independence of the momentum relaxation time, they can be expressed as:

$$\sigma_{xx} = \sigma_{yy} = \frac{Ne^2}{m^*}\left\langle \frac{\tau}{1+\omega_c^2\tau^2} \right\rangle, \tag{2.1}$$

$$\sigma_{xy} = -\sigma_{yx} = -\frac{Ne^2}{m^*}\left\langle \frac{\omega_c\tau^2}{1+\omega_c^2\tau^2} \right\rangle, \tag{2.2}$$

where the angular brackets denote an average over energy. Since as stated in the title of this section, our present aim is to derive the formulae for various types of low-field magnetoresistance, it would be more convenient from now on to operate with a magnetoresistivity tensor $\hat{\rho}$ instead of $\hat{\sigma}$. It is well known from elementary electrodynamics [5, 6], that $\hat{\rho} = \hat{\sigma}^{-1}$, what in connection with a prescription for inverting a 2×2 matrix:

$$A = \begin{pmatrix} a & b \\ c & d \end{pmatrix} \quad \Rightarrow \quad A^{-1} = \frac{1}{\det A}\begin{pmatrix} d & -b \\ -c & a \end{pmatrix},$$

where $\det A$ stands for a determinant of A, means that:

$$\hat{\rho} = \begin{pmatrix} \rho_{xx} & \rho_{xy} \\ \rho_{yx} & \rho_{yy} \end{pmatrix} = \frac{1}{\sigma_{xx}\sigma_{yy} - \sigma_{xy}\sigma_{yx}}\begin{pmatrix} \sigma_{yy} & -\sigma_{xy} \\ -\sigma_{yx} & \sigma_{xx} \end{pmatrix}. \tag{2.3}$$

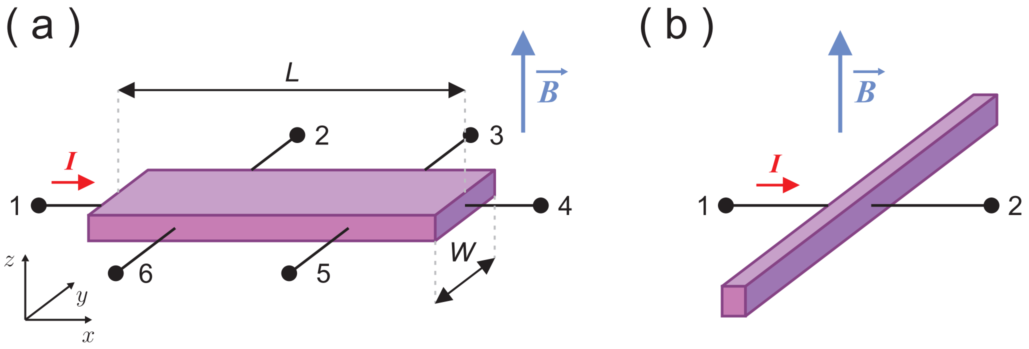

Figure 2.1: Typical geometries of semiconductor samples used in studies of magnetotransport phenomena: (a) a 6-terminal Hall-bar sample with length L that significantly exceeds the width W, (b) a so-called matchstick-sample with $L \ll W$, serving as a building-block for simple magnetic field sensors [108] due to the geometrical magnetoresistance it exhibits.

In order to proceed further, we have next to take into account the geometry of a sample containing a 2DEG. For the sake of simplicity we will consider only a rectangular shape defined by the length L and the width W, and following a standard practice, we will divide our analysis into three steps referring to the case of $L \gg W$ (a so-called Hall-bar sample), $L \ll W$ (a so-called matchstick sample) and $L \sim W$, respectively (a detailed review of other possible geometries can be found, for instance, in [109]). The first two of the aforementioned configurations are schematically depicted in Fig. 2.1. If the current is passed through a Hall-bar sample using terminals 1 and 4 (panel (a)), the boundary condition which holds in a steady-state is that the current density along the y-direction vanishes, $J_y = 0$, since all the other terminals serve only as voltage probes. By inserting this requirement into a DC form of Eq. (1.9) rewritten in terms of resistivity tensor

$$\begin{pmatrix} E_x \\ E_y \end{pmatrix} = \begin{pmatrix} \rho_{xx} & \rho_{xy} \\ \rho_{yx} & \rho_{yy} \end{pmatrix} \begin{pmatrix} J_x \\ J_y \end{pmatrix} \tag{2.4}$$

we get: $E_x = \rho_{xx} J_x$ and $E_y = \rho_{yx} J_x$. Then, by going through expansion of expressions (2.1) and (2.2) for low magnetic fields or, equivalently, for $\omega_c \tau \ll 1$, it can be shown that [110]:

$$\rho_{xx}(B) = \rho_{yy}(B) \simeq \left\{ \left(\frac{Ne^2}{m^*}\right) \langle\tau\rangle \left[1 - \left(\frac{eB}{m^*}\right)^2 \langle\tau\rangle^2 \cdot \frac{\langle\tau^2\rangle^2}{\langle\tau\rangle^4} \cdot \left(\frac{\langle\tau^3\rangle\langle\tau\rangle}{\langle\tau^2\rangle^2} - 1 \right) \right] \right\}^{-1}, \tag{2.5}$$

$$\rho_{yx}(B) = -\rho_{xy}(B) \simeq -\frac{1}{Ne} \frac{\langle\tau^2\rangle}{\langle\tau\rangle^2} B, \tag{2.6}$$

where we have utilized Eq. (2.3) and the definition of the cyclotron frequency given in the preceding chapter. The form of the above formulae can be greatly simplified by introducing the following quantities: the diffusive transport mobility $\mu_{\mathrm{con}} = e\langle\tau\rangle/m^*$, the Hall factor $r = \langle\tau^2\rangle/\langle\tau\rangle^2$ and the magnetoresistance coefficient $\xi = (\langle\tau^3\rangle\langle\tau\rangle/\langle\tau^2\rangle^2) - 1$. With their help Eqs. (2.5) and (2.6) read:

$$\rho_{xx}(B) = \rho_{yy}(B) \simeq \frac{1}{Ne\mu_{\mathrm{con}}} \cdot \frac{1}{1 - \mu_{\mathrm{con}}^2 r^2 \xi B^2} = \frac{1}{Ne\mu_{\mathrm{con}}} \cdot \frac{1}{1 - \mu_{\mathrm{PMR}}^2 B^2}, \tag{2.7}$$

$$\rho_{yx}(B) = -\rho_{xy}(B) \simeq -\frac{r}{Ne} B = RB, \tag{2.8}$$

where $\mu_{\mathrm{PMR}} = r\xi^{1/2}\mu_{\mathrm{con}}$ stands for the physical magnetoresistance coefficient and R denotes the famous Hall coefficient. In the low-magnetic-field range, (2.7) can further be expanded as: $\rho_{xx}(B) = \rho_{yy}(B) \simeq (1/Ne\mu_{\mathrm{con}})(1 + \mu_{\mathrm{PMR}}^2 B^2)$, what means that a quadratic increase with B of the transverse[1] resistivity of a 2DEG is expected, provided that $\tau(E) \neq \mathrm{const}$. For degenerate electron gases, however, the momentum relaxation time is nearly independent of the energy and in consequence $\xi \approx 0 \Rightarrow \mu_{\mathrm{PMR}} \approx 0$.

In the case of a matchstick-sample illustrated in Fig. 2.1(b), which often serves as a building-block for simple magnetic field sensors [108], the boundary condition for a steady-state current flow is zeroing of the transverse[2] electric field, i.e. $E_y = 0$. It results from shorting the Hall voltage by the closely spaced source and drain

---

[1] Throughout the rest of this thesis we will be using the terms: 'transverse resistivity' and 'Hall resistivity' for the $\rho_{xx} = \rho_{yy}$ and $\rho_{xy} = -\rho_{yx}$ components of the magnetoresistivity tensor, respectively.

[2] With respect to the direction of an external electric field.

electrodes assumed to be made of perfectly conductive metals. When inserted into the expression (2.4), this requirements gives two equations: $E_x = (\rho_{xx} - \rho_{xy}\rho_{yx}/\rho_{yy})J_x$ and $J_y = -(\rho_{yx}/\rho_{yy})J_x$, which after performing an identical analysis as described above yield the following formula for the diagonal components of the resistivity tensor:

$$\rho_{xx}(B) = \rho_{yy}(B) \simeq \frac{1}{Ne\mu_{\mathrm{con}}} \cdot \frac{1}{1 - r^2(\xi+1)\mu_{\mathrm{con}}^2 B^2} = \frac{1}{Ne\mu_{\mathrm{con}}} \cdot \frac{1}{1 - \mu_{\mathrm{GMR}}^2 B^2}, \qquad (2.9)$$

The off-diagonal components remain the same as derived for the Hall geometry. The factor $\mu_{\mathrm{GMR}} = r(\xi+1)^{1/2}\mu_{\mathrm{con}}$ that appears in Eq. (2.9) is known as a geometrical magnetoresistance coefficient. In contrast to μ_{PMR} it does not vanish for $\xi = 0$, what means that geometry-related increase with B of the transverse resistivity of an electron gas can be observed even when $\tau(E) = \mathrm{const.}$ In the low-magnetic field range, an approximated form of (2.9): $\rho_{xx}(B) = \rho_{yy}(B) \approx (1/Ne\mu_{\mathrm{con}})(1 + \mu_{\mathrm{GMR}}^2 B^2)$ can be successfully used for determining the mobility of a degenerate 2DEG, since for an energy-independent momentum relaxation time $\mu_{\mathrm{GMR}} \approx \mu_{\mathrm{con}}$.
It is worth mentioning here that in both configurations discussed so far, the mutual orientation of the total current and the total electric field in every single part of the 2DEG layer apart from the electrodes is exactly the same: they are angled at $\vartheta = \arctan(\mu_{\mathrm{con}}B) = \arctan(\omega_c\tau)$ with respect to each other. If $L \sim W$ such a statement is, however, no longer true as displayed by Fig. 2.2(a) showing the results of numerical simulations [111, 112] of the electric potential (color scale) and current (black arrows with the size corresponding to the magnitude of the local current) distributions inside a square-shaped conductor characterized by a mobility μ and subject to an external bias voltage of 1 V applied between the left and right edges, as well as a perpendicular magnetic field of the strength $B = 30/\mu$. As can be seen, the current is most strongly perturbed in the vicinity of the electrodes, but deep within the conductor becomes uniformly spread and yields no magnetoresistance in the $L, W \to \infty$ limit. A remarkable observation is also that the majority of the current enters the conductor at the top left corner and leaves at the bottom right corner, what directly reflects the fact that $\vartheta \sim 90^\circ$ and no current is allowed to flow across the top and bottom edges of the sample, as was assumed by the authors when performing the simulations.

It is clear from the quoted example that a theoretical treatment of the $L \sim W$ case is much more complicated as compared to description of the magnetoresistivity tensor in the $L \gg W$ and $L \ll W$ limits. For simple shapes (like the rectangular one), a method known as the conformal mapping approach [113–117] turned out to be very successful in solving the Maxwell equations for a conductor subject to an external static magnetic field. Although very instructive, discussing the details of this technique lies beyond the scope of the present thesis. Therefore in what follows

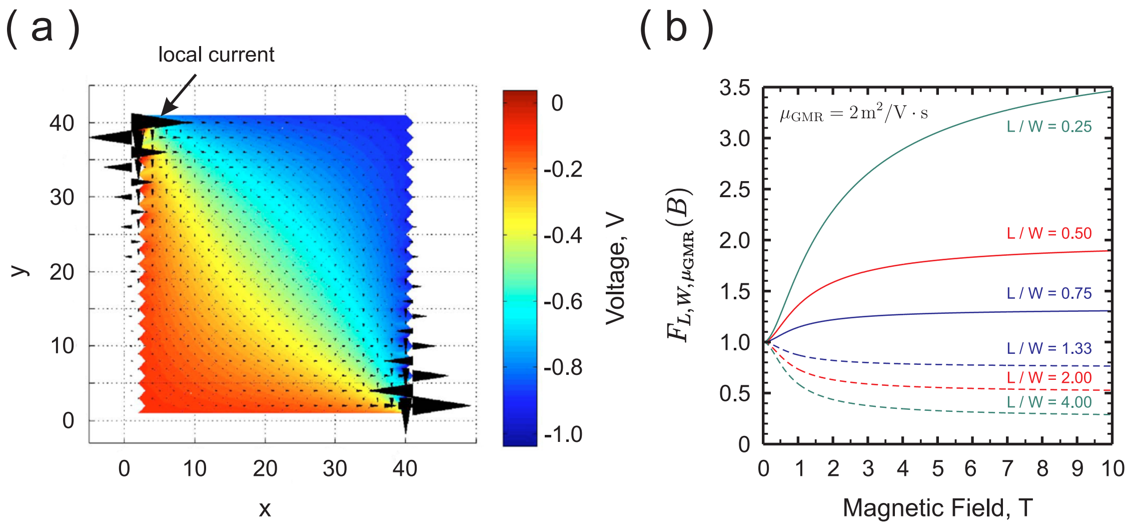

Figure 2.2: (a) Distributions of the electric potential (color scale) and current (black arrows with the size corresponding to the magnitude of the local current), obtained numerically for a square-shaped conductor at $\mu B = 30$ (the Hall angle equal to 88°) and 1 V of bias voltage applied between the left and right edges (after [112]). (b) Geometrical factor (refer to Eqs. (2.11)–(2.12)) resulting from the conformal mapping approach to description of the transverse magnetoresistance exhibited by a rectangular sample of $L \sim W$ (L - length, W - width), plotted as a function of the magnetic field for the geometrical magnetoresistance coefficient $\mu_{\rm GMR} = 2\,{\rm m}^2/{\rm Vs}$ and six values of the aspect ratio L/W. Note that curves drawn in the same color but with different line styles correspond to exchanging the positions of L and W in the respective formulae.

we will give only the final formulae for the $\rho_{xx}(B)$ component of the magnetoresistivity tensor, which we will then use in analysis and interpretation of the experimental data presented in the section of Chapter 4 devoted to magnetotransport measurements. For a rectangular specimen of an arbitrary L/W ratio, the magnetic-field induced changes in the transverse resistivity are described by [112]:

$$\rho_{xx}(B) = \rho_0\sqrt{1+\mu_{\rm GMR}^2 B^2}\cdot F_{L,W,\mu_{\rm GMR}}(B), \tag{2.10}$$

where ρ_0 denotes the zero-field resistivity, the square-root term corresponds to the $L = W$ case and the function $F_{L,W,\mu_{\rm GMR}}(B)$ expressed as:

$$F_{L,W,\mu_{\rm GMR}}(B) = \frac{\displaystyle\int_0^1 dx\cos\left(\Theta_{WL}(B;x)\right)}{\displaystyle\int_0^1 dx\cos\left(\Theta_{LW}(B;x)\right)} \tag{2.11}$$

with

$$\Theta_{WL}(B;x) = \sum_{n\,({\rm odd})} \frac{4{\rm arctan}\left(\mu_{\rm GMR}B\right)}{n\pi}\,\frac{\sin(n\pi x)}{\cosh\left(\frac{n\pi}{2}\frac{W}{L}\right)} \tag{2.12}$$

accounts for deviations from the square shape. Fig. 2.2(b) demonstrates the plots of this function obtained by numerical means for six L/W ratios, $\mu_{\rm GMR} = 2\,{\rm m}^2/{\rm Vs}$ and the principally infinite series in (2.12) limited to the first 325 terms, which turned out to be sufficient for getting a stable value of $\Theta_{WL}(B;x)$ for $B \leqslant 10$T. As can be seen, each of the curves tends to saturate at a constant level in the high-magnetic field range. On the other hand, the square-root term in expression (2.10) prevents the $\rho_{xx}(B)$ from saturating and gives rise to a nearly linear magnetoresistance in the $B \to \infty$. But the question arises whether using Eqs. (2.10)–(2.12) for $\omega_c\tau > 1$ is justified? Certainly, when the Landau quantization of the electrons' motion in the plane perpendicular to the direction of a magnetic field starts to play a predominant role, the only appropriate description of the carrier dynamics is the quantum-mechanical one (see for example [118,119]). The geometrical magnetoresistance can, however, survive in the above-mentioned form up to relatively high magnetic fields (of the strength of 10 T or more), provided that the Landau levels are significantly broadened by the scattering processes. Under such conditions, $\omega_c\tau$ with τ representing a momentum relaxation time can become substantially larger than 1, but the system will still behave as essentially classical one with at most a small onset of quantum-mechanical effects. This means that $\omega_c\tau > 1$ is not always a good criterion for distinguishing between the low- and high-magnetic-field regimes. Indeed, as we will see in the next section, a so-called quantum relaxation time has to be considered in order to estimate the range of validity of the classical description of magnetransport phenomena in a much more accurate way.

2.2 High magnetic fields: Shubnikov-de Haas oscillations

In accordance with our discussion from the previous section, by high magnetic fields we will understand the fields at which the separation between the Landau levels (LLs) becomes larger than their width resulting from various scattering processes. When such a condition is satisfied, a variety of new phenomena emerges [107]. They all rely on the singularities that appear in a density of states, $D(E)$, of the electron gas subject to a quantizing magnetic field. When $B = 0$, $D(E)$ of a 2DEG is a staircase function with steps corresponding to different subbands in the quantum well [22–24, 98]. At high magnetic field, this continuous function splits into a series of Dirac delta-like peaks, each associated with a single particle state of the energy $E_{j,n,s}(B)$, which in the case of isotropic semiconductors with simple, spherical and parabolic profiles of the conduction and valence bands can be expressed as [22]:

$$E_{j,n,s}(B) = E_j + \left(n + \frac{1}{2}\right)\hbar\omega_c + sg\mu_{\mathrm{B}}B \tag{2.13}$$

where E_j denotes the energy of the bottom of the j-th subband, $n = 0, 1, 2, ...$ labels the LLs, μ_B is the Bohr magneton, g stands for the Landé factor of the electron and s represents the spin quantum number. The degeneracy of all LLs is exactly the same and for a given B equals to $N_L = eB/h$. This means that a Landau level with an energy smaller than the Fermi energy, E_F, is occupied with N_L electrons per unit area. In consequence, a 2DEG of density N fills in

$$\nu = \frac{Nh}{eB} \tag{2.14}$$

LLs, provided that E_F is located below the bottom of the second subband in the quantum well. This parameter is known in the literature as the filling factor. The energies of the LLs, as well as their degeneracy and the inter-level spacing linearly increase with B. As a result, when sweeping the magnetic field, the LLs with energies that were initially smaller than E_F progressively pass through the Fermi level and empty of electrons, which transfer to the directly next lower LLs. Each time it happens, the diagonal components of the magnetocoductivity tensor sharply increase whereas maxima or minima in the transverse resistivity occur, depending on the geometry of the sample as well as the material it is made of [107]. In the case of dense 2DEGs occupying a large number of LLs up to relatively high magnetic fields, the appearance of each maximum/minimum of these so-called Shubnikov-de Haas (SdH) oscillations is associated with a decrease in ν by 2, since in accordance with (2.13), for $n \gg 1$ the spin-splitting of LLs is practically unresolvable under standard experimental conditions. When written down mathematically, this observation yields:

$$\frac{2e}{h}\left(\Delta\left(\frac{1}{B}\right)\right)^{-1} = \frac{2e}{h}f = N, \tag{2.15}$$

where $\Delta(1/B)$ and f denote the period and the frequency of the SdH oscillations when treated as a function of the reciprocal magnetic field. As can be seen, Eq. (2.15) provides a direct way to estimating the density of a 2DEG.

In order to get a complete description of the SdH oscillations as well as the other galvanomagnetic effects related to the formation of LLs, a fully quantum-mechanical approach is required [118, 119]. Since this subject is extensively discussed in various textbooks on condensed matter physics (see for example [98, 107]), in what follows we will only recall the final formulae, which we have utilized when treating the results of magnetotransport measurements presented in Chapter 4. As shown in [120–123], an oscillatory correction to the density of states of a degenerate 2DEG subject to an external magnetic field and kept at the non-zero temperature, T, can be expressed in the form:

$$\frac{\Delta D(E_F)}{D_0} = 2\sum_{r=1}^{\infty} \exp\left(-\frac{\pi m^*}{e\tau_\mathrm{q}}\frac{r}{B}\right)\frac{A(T)r/B}{\sinh\left(A(T)r/B\right)}\cos\left(\pi\frac{Nh}{e}\frac{r}{B} - r\pi\right), \tag{2.16}$$

where $A(T) = 4\pi^3 k_\mathrm{B} T m^*/he$, k_B is the Boltzmann constant, D_0 represents the density of states at $B = 0$ and τ_q denotes the so-called quantum relaxation time. With the aid of the above equation, the modified components of the magnetoresistivity tensor read:

$$\rho_{xx}(B) = \rho_0 \left(1 + 2\frac{\Delta D(E_F)}{D_0}\right), \tag{2.17}$$

$$\rho_{xy}(B) = \rho_0 \omega_c \tau_\mathrm{t} \left(1 - \frac{1}{\omega_c^2 \tau_\mathrm{t}^2}\frac{\Delta D(E_F)}{D_0}\right), \tag{2.18}$$

where ρ_0 stands for the zero-field resistivity and τ_t is exactly the same momentum relaxation time as discussed previously, but with a subscript 't' added to avoid confusing it with τ_q. If the SdH oscillations are extracted from the transverse magnetoresistivity traces that exhibit any contribution coming from the geometrical magnetoresistance, ρ_0 in expression (2.17) should be replaced with (2.10). This becomes clear upon analysing the components of the magnetoconductivity tensor that lead to Eqs. (2.17)–(2.18). Furthermore, because of strong damping by exponential factors, it is usually sufficient to take into account only the first term of the infinite series that appears in (2.16). As a result, the formula which describes the transverse magnetoresistance up to magnetic fields at which both the classical and quantum effects start to coexist, but the former ones play a predominant role, takes on the form:

$$\begin{aligned}\rho_{xx}(B) =& \rho_0 \sqrt{1 + \mu_\mathrm{GMR}^2 B^2} \cdot F_{L,W,\mu_\mathrm{GMR}}(B) \times \\ & \times \left\{1 - \frac{4A(T)/B}{\sinh(A(T)/B)} \exp\left(-\frac{\pi m^*}{e\tau_\mathrm{q}}\frac{1}{B}\right) \cos\left(2\pi\left(\frac{Nh}{2e}\right)\frac{1}{B}\right)\right\}.\end{aligned} \tag{2.19}$$

We will make an extensive use of it when interpreting the results of magnetotrasport measurements presented in one of the sections of Chapter 4. However, before moving to the experimental part of this thesis, we would like to discuss in more detail the physical meaning of the quantum relaxation time. In accordance with [124], both τ_t and τ_q refer to the angle-dependent scattering rate, $P(\vartheta)$, but whereas the latter one reflects the total scattering rate, i.e.[3]

$$\frac{1}{\tau_\mathrm{q}} = \int P(\vartheta)\mathrm{d}\vartheta, \tag{2.20}$$

the low-angle scattering events are strongly suppressed in the formula for τ_t, since they do not result in any significant deflection of a current-path:

$$\frac{1}{\tau_\mathrm{t}} = \int P(\vartheta)(1 - \cos\vartheta)\mathrm{d}\vartheta. \tag{2.21}$$

---

[3] Since we are only interested in the case of a degenerate 2DEG, an energy average in Eqs. (2.20) and (2.21) is not necessary.

As a result, the ratio $\tau_{\mathrm{t}}/\tau_{\mathrm{q}} \geqslant 1$ provides a convenient measure of the dominant angle of scattering processes that occur in a 2DEG, what in turn helps to identify them. Considering typical semiconductor heterostructures, the large-ϑ (or, equivalently, short-range) scatterings are mainly due to the interface roughness, dislocations or impurities in the 2DEG layer. On the other hand, the small-ϑ (or long-range) ones mostly originate from the remote impurities, like rechargeable surface states or donors/acceptors located in a heterostructure's barrier. In the case of the first group $\tau_{\mathrm{t}}/\tau_{\mathrm{q}} \simeq 1$ should be expected, whereas for the second one $\tau_{\mathrm{t}}/\tau_{\mathrm{q}} \gg 1$.
The value of τ_{t} can be estimated on the basis of low-magnetic field portion of the transverse magnetoresistance data given by Eq. (2.19). Since for a highly degenerated 2DEG, the quantum effects becomes unimportant as $B \to 0$ and also $F_{L,W,,\mu_{\mathrm{GMR}}}(B) \to 1$ (refer to Fig. 2.2(b)) in this limit, the $\rho_{xx}(B)$ component of the magnetoresistivity tensor can be approximated by:

$$\frac{\rho_{xx}(B)}{\rho_0} \approx 1 + \frac{1}{2}\mu_{\mathrm{GMR}}^2 B^2 \simeq 1 + \left(\frac{e\tau_{\mathrm{t}}}{m^*}\right)^2 B^2. \tag{2.22}$$

In contrast, the evaluation of τ_{q} relies on the high-magnetic-field part of the $\rho_{xx}(B)$ measurements carried out at the constant temperature, T, and is customarily done within a framework of the so-called Dingle plot [125], i.e. a semi-logarithmic graph displaying the normalized amplitude of the SdH as a function of $1/B$. When transformed into such a representation, Eq. (2.19) reads:

$$\ln\left(\left|\frac{\rho_{xx}(B) - \rho_{\mathrm{GMR}}(B)}{\rho_{\mathrm{GMR}}(B)} \cdot \frac{\sinh(A(T)/B)}{4A(T)/B}\right|\right) = -\frac{\pi m^*}{e\tau_{\mathrm{q}}}\frac{1}{B}, \tag{2.23}$$

where ln(...) stands for the natural logarithm and $\rho_{\mathrm{GMR}}(B) = \rho_0\sqrt{1 + \mu_{\mathrm{GMR}}^2 B^2} \cdot F_{L,W,\mu_{\mathrm{GMR}}}(B)$. As can be seen, in the above form, it reduces to just a straight line with zero intercept and slope that is inversely proportional to τ_{q}.

Part II

Experimental results

Chapter 3

GaN/AlGaN structures under investigation

This chapter is mainly focused on the presentation of GaN/AlGaN transistor structures that have been investigated by the author in the course of his PhD research. We provide a comprehensive description of their layout, geometry and chemical composition. The most important features of the fabrication process are also discussed along with the material parameters that are relevant to interpretation of the experimental results presented in Chapter 3. Furthermore, we address all the approximations and assumptions mentioned in the preceding part of this dissertation and by careful evaluation of the quantities they refer to, we examine their validity and applicability to our structures. Finally, we also present the results of the first optical measurements performed by means of the Fourier Transform Infrared Spectroscopy (FTIR) on the samples that were very similar to our ones [94]. Those experiments, carried out in the absence of a magnetic field, revealed a series of nicely developed plasma resonances of a 2DEG in the GaN/AlGaN transistor structures under investigation. The authors also demonstrated the possibility of tuning the plasma frequency by an electrical potential applied to the gate electrode. Their results motivated us to extend the research they have initiated to magnetoplasma waves, which except for a few attempts [126–132], have not yet been systematically studied in the GaN-based systems.

Before addressing all the issues listed above, we need, however, to discuss one more subject of a general meaning, namely, the methods of coupling the electromagnetic radiation with 2D plasma/magnetoplasma oscillations. As is well known [36,133], free plasmons in both three and two dimensions are non-radiative eigenmodes as long as the electron gas which supports them represents a homogeneous medium of infinite size. It results from the fact, that for any given wave vector's length, their phase and group velocities remain smaller than the speed of light. In consequence, bringing a plasmon and a photon into interaction requires a special treatment. Although there are various techniques of establishing such a coupling, we will restrict ourselves to the one that has been the most extensively used in a solid-state-plasma research over the last three decades, i.e. to the method based on diffraction gratings.

3.1 Grating couplers

The above-mentioned problem of mismatch in the momentum space between a photon and a 2D plasmon we want to excite by optical means is illustrated in Fig. 3.1(a). As can be seen, in the whole range of the wave-vector variation, the solid red line visualizing the dispersion relation of the electromagnetic radiation in a medium characterized by a refractive index n (we have assumed in our calculations that $n \equiv n_{\mathrm{GaN}} \simeq \sqrt{\varepsilon_{\mathrm{s}}}$), and described by $\omega_{\mathrm{ph}}(q) = (c/n)q$, where c stands for the speed of light in the free space, goes above the solid blue curve corresponding to plasma oscillations of a 2DEG in a gated heterostructure.[1] Thus, in order to bring the plasmon and the photon into interaction, the wave vector's length of the latter has to be increased by Δq. In practice, due to the fact that $q_{\mathrm{photon}} \ll q_{\mathrm{plasmon}}$, $\Delta q \simeq q_{\mathrm{plasmon}}$. Unfortunately, this is not the only mismatch that has to be overcome. In accordance with our discussion from the previous chapter, plasmons are longitudinal oscillations of a charge density. This means, that they can only be excited by longitudinal electric waves. However, from

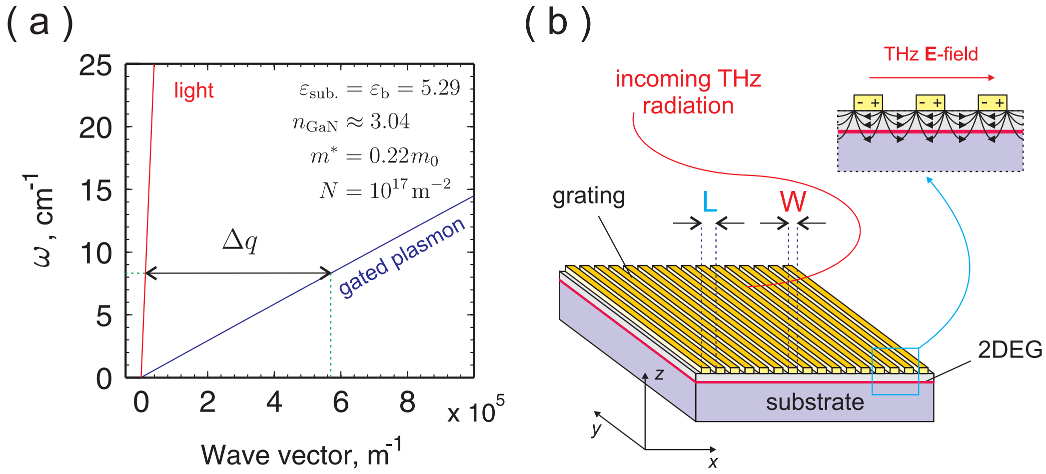

Figure 3.1: (a) Low-frequency dispersion relations of light propagating in GaN (solid red line) and gated 2D plasma oscillations in GaN/AlGaN heterostructure (solid blue curve), calculated with the use of material parameters listed in the upper-right corner of the diagram. (b) Schematic illustration of a heterostructure sample equipped with a grating coupler of period L and an individual metallic strip's width W. The inset demonstrates a distribution of the local electric fields beneath the grating, induced by the electromagnetic field of THz frequency that impinges on the sample along its surface normal.

---

[1] This statement is true in general, for any system containing a 2D plasma (not only for gated heterostructures chosen as an example).

Maxwell's equations, the propagation of such waves is forbidden in non-conducting media like standard dielectrics without a high anisotropy or any particular patterning of their structure (typical for photonic crystals) - only the transverse modes can pass through them [5, 6]. This fact rises an important question about the way of converting at least a part of transverse electromagnetic radiation impinging onto the sample that contains a 2DEG, into the longitudinal electric waves propagating in the plane of 2DEG with wave vectors that are matched to dispersion relation of 2D plasma oscillations.

As mentioned in the introduction to this chapter, the easiest and the most reliable method of solving the above problem in the case of a solid-state-plasma research is by depositing a diffraction grating on top of a sample under study. Such a technique has been successfully used in many milestone experiments on the resonant plasmon and magnetoplasmon excitations in 2D semiconductor structures that have been carried out over the last thirty years [134–138].[2]

In Fig. 3.1(b) we demonstrate a diagram of a heterostructure sample equipped with a grating coupler. As can be seen, the grating's geometry is fully determined by two parameters: the period L and the width of an individual metallic strip W. In the literature, these parameters are frequently combined to give $r = W/L$ - the so-called mark fraction or duty cycle of the grating. In order to efficiently couple the incident photons with the plasmons, a condition $L \sim \lambda_{\text{plasmon}}$ has to be satisfied. It is worth mentioning that the form of the grating coupler depicted in Fig. 3.1(b) is the most typical one. Other common realizations rely on introducing an additional, thin metallic layer just beneath the grating (a uniform gate electrode that is semi-transparent to the far-infrared radiation) or periodical patterning of a barrier layer (or layer of highly resistive dielectric, if present), which is then covered with a continuous film of metal. In spite of technical differences, the physical foundations of the grating operation are exactly the same in all the above-cases, i.e. the central role is played by diffraction of the electromagnetic radiation that impinges on the sample's surface.[3] First of all, however, the grating from Fig. 3.1(b) acts as a simple wire-polarizer passing through only the light that is polarized across the metallic strips. Unlike the standard case in which the slit $S = L - W$ between adjacent metallic strips approximately equals to the wavelength of the electromagnetic radiation being diffracted, here $S \ll \lambda_{\text{photon}}$, since in accordance with our previous discussion $q_{\text{photon}} \ll q_{\text{plasmon}} \Rightarrow \lambda_{\text{photon}} \gg \lambda_{\text{plasmon}} > S$. Therefore, a major part of the light allowed by the grating is then further transmitted through the sample as a so-called

---

[2] See also the references given when discussing the physical interpretation of a dispersion relation of 2D magnetoplasma waves in subsection 1.3.2.

[3] In what follows we will be always assuming the incident radiation to be moving along the surface normal.

zeroth-order beam. The remaining fraction interacts with electrons in the strips giving rise to excitation of local electric fields that exist only in the close proximity of the grating and the 2DEG. As shown in the inset to Fig. 3.1(b), these fields are oriented mostly parallel to the sample's surface, and their spatial variation in the x-direction has the same periodicity as the grating coupler. In consequence, they can equally well be viewed as a standing longitudinal electric wave composed of harmonic waves that counter-propagate along the x-axis with the wave vectors given by:

$$k_{x,n} = nG, \quad G = \frac{2\pi}{L}, \quad n = 1, 2, 3, ..., \tag{3.1}$$

where G denotes the reciprocal grating vector. Under resonance conditions, these waves directly couple with the plasma oscillations, since contrary to the incident electromagnetic radiation they have an appropriate symmetry and a plasmon-matched spatial variation. However, as we have seen in subsection 1.3.1, they cannot propagate away from the conducting layers. That is why they appear only in the close vicinity of the grating and the layer of 2DEG. Outside this region their amplitudes exponentially decay along the sample's surface normal (z-direction in Fig. 3.1(b)). A typical length-scale for this process equals to $1/k_{x,n} \sim \lambda_{\text{plasmon}}/10n$ (refer to Eq. (1.75)). Therefore, if $\lambda_{\text{plasmon}} \sim 1\,\mu\text{m}$ in the electron system under investigation and we would like to excite up to $n = 10$ plasmon resonances, the separation between the grating coupler and the 2DEG shall not be significantly greater than 10 nm.

Partial conversion of the incident electromagnetic radiation into the longitudinal electric waves that we have just discussed, influences the zeroth-order beam regardless of whether the resonance conditions for plasmon excitation are satisfied or not, since the currents induced in the grating coupler and the 2DEG layer always dissipate some energy as a heat. In the former case, however, the net effect is bigger due to an additional resonant absorption of energy by plasma oscillations. This fact underlies the possibility of extracting the traces of plasmon resonances from transmission spectra, i.e. the intensity of the zeroth-order beam recorded as a function of the frequency of the incident electromagnetic radiation, the magnetic field applied to the sample or the density of a 2DEG. Modelling of such spectra can be done either by analytical methods [135, 139–141] or in a fully numerical approach [142].

It should be emphasized that diffraction grating deposited on top of a heterostructure containing a 2DEG, not only brings the incident photons and the plasmons into interaction, but also significantly modifies the dispersion relation of the latter. This state of affairs results from the fact that screening of plasma oscillations by image charges depends on the extent to which the surface above a 2DEG layer is covered with a metal [143]. According to our analysis from subsection 1.4.2, the effective dielectric function of a heterostructure equipped with a grating coupler, $\varepsilon_{\text{eff}}^{\text{grat.}}(qd)$, should fall in between the dielectric functions corresponding to the ungated and gated heterostructures, respectively. Mathematically, this observation can be expressed as:

$$\varepsilon_{\text{eff}}^{\text{grat.}}(qd) = \alpha(d;q)\varepsilon_{\text{g}}(qd) + [1-\alpha(d;q)]\,\varepsilon_{\text{ug}}(qd), \tag{3.2}$$

where as previously, d stands for the thickness of the barrier layer, separating now the 2DEG from the grating, and $\alpha(d;q)$ represents an interpolation function. We shall see later on that to a good approximation $\alpha(d;q) \simeq r = W/L$.

The geometry of a grating coupler, determined in the simplest case by L and W, also influences the strength of the local electric fields that are directly responsible for exciting the plasma waves. It is well known that observation of higher-order plasmon resonances becomes possible only in the structures equipped with narrow-slit gratings of a relatively large period [87, 144]. When tuning L and W towards such conditions, the resulting distribution of a longitudinal electric field beneath the grating changes from the sinusoidal into the comb-like one. From elementary Fourier analysis it is clear that reproducing the latter shape from the series of harmonic waves requires their spectrum to be much richer than in the case of the former one. This in turn increases the probability of exciting the higher-order modes of plasma oscillations.

The situation further complicates when an electrical potential is applied to the grating coupler. Indeed, when only the quality of the structure under investigation allows for it, a grating covering the sample's surface may serve both to excite the plasma waves in the layer of 2DEG and to control its concentration under the metallic strips. Because of the grating's geometry, the resulting spatial modulation of a 2DEG density has a periodic character and influences the motion of electrons in a similar way as the electrostatic potential of a crystal lattice (superlattice effect). This in turn leads to opening of the minigaps in the plasmon dispersion curve, appearing at integer multiples of π/L - the wave vectors corresponding to the Brillouin zone boundaries [139, 145, 146]. They can be observed especially for low-frequency modes of plasma oscillations, since their size decreases with q.

Even more important consequence of the electrical polarization of a grating coupler is, however, the modification it makes to the spectrum of plasmon resonances [63, 87, 146, 147]. In order to analyse this phenomenon it is convenient to define a so-called density modulation factor: $\alpha_m = (N_{\text{ug}} - N_{\text{g}})/(N_{\text{ug}} + N_{\text{g}})$, where N_{g} and N_{ug} denote the equilibrium concentrations of a 2DEG under the grating-gate fingers and openings, respectively. For unmodulated and weakly modulated 2DEG ($\alpha_m < 0.1$), the plasma waves being excited extend over the whole unit cell of a structure (the whole period of a grating). In principle, they can propagate with any given q, however, due to a particular spectrum of the longitudinal electric field produced by the grating, the only observable modes are described by:

$$q_j = \frac{2\pi}{L} j, \quad j = 1, 2, 3, ... \tag{3.3}$$

Under such conditions, the effect of screening the plasma oscillations by an overlaid grating coupler is the best modelled by (3.2). As α_m increases, the unit cell breaks into quite well resolved gated and ungated sections. In consequence, two branches of plasma waves appear: almost totally screened that extend over the gated part of a unit cell and almost totally unscreened, whose propagation range is restricted to the ungated portion of a unit cell. The adverb 'almost' refers to the boundary region between the two sections, where due to interaction between waves belonging to different branches, characterizing them exclusively by[4] $\varepsilon_{\mathrm{g}}(qd)$ or $\varepsilon_{\mathrm{gu}}(qd)$ is not strictly correct. Because of confinement, the set of wave vectors allowed for the plasma waves in each branch is discrete. It can be shown that for symmetric boundary conditions at the ends of the gated and ungated parts, the plasmon wave vectors in the first one are given by:

$$q_j = (2j-1)\frac{\pi}{W}, \quad j = 1, 2, 3, ..., \tag{3.4}$$

whereas in the second one:

$$q_j = (2j-1)\frac{\pi}{S}, \quad j = 1, 2, 3, ... \tag{3.5}$$

In accordance with our previous analysis summarized in Fig. 1.12(b), in the frequency range below the first ungated resonance, only the gated plasma oscillations can be observed. Finally, as α_m approaches 1, the plasma waves under the grating-gate fingers progressively disappear, leaving behind only that in the openings. In such a case, it is more appropriate to treat the electron system under investigation as composed of nearly independent one-dimensional quantum wires rather than forming a continuous 2D film [63].

3.2 Grating-gate GaN/AlGaN transistor structures under study

GaN is undeniably one of the most important semiconductor materials, especially from the point of view of high-temperature and high-frequency applications in the fields of high-speed electronics, optoelectronics and the blue, violet and ultra-violet optics. There are numerous excellent books and reviews that confirm this thesis by describing in details the properties of GaN itself and the GaN-based devices, as well as

---

[4] See Eq. (1.105) and (1.106) describing the respective dielectric functions for gated and ungated heterostructures.

systematizing more than twenty years of their intensive development and progressive improvement [148–161]. For basic research, however, focused on the fundamental phenomena that can be accessed in III-V semiconductor structures, GaN still stays in the background of GaAs-based systems. As we have seen in the preceding chapter, it is particularly true for studies of 2D plasma and magnetoplasma excitations. We hope that our work described in the remaining part of the text will take at least a little step towards changing the above-mentioned situation.

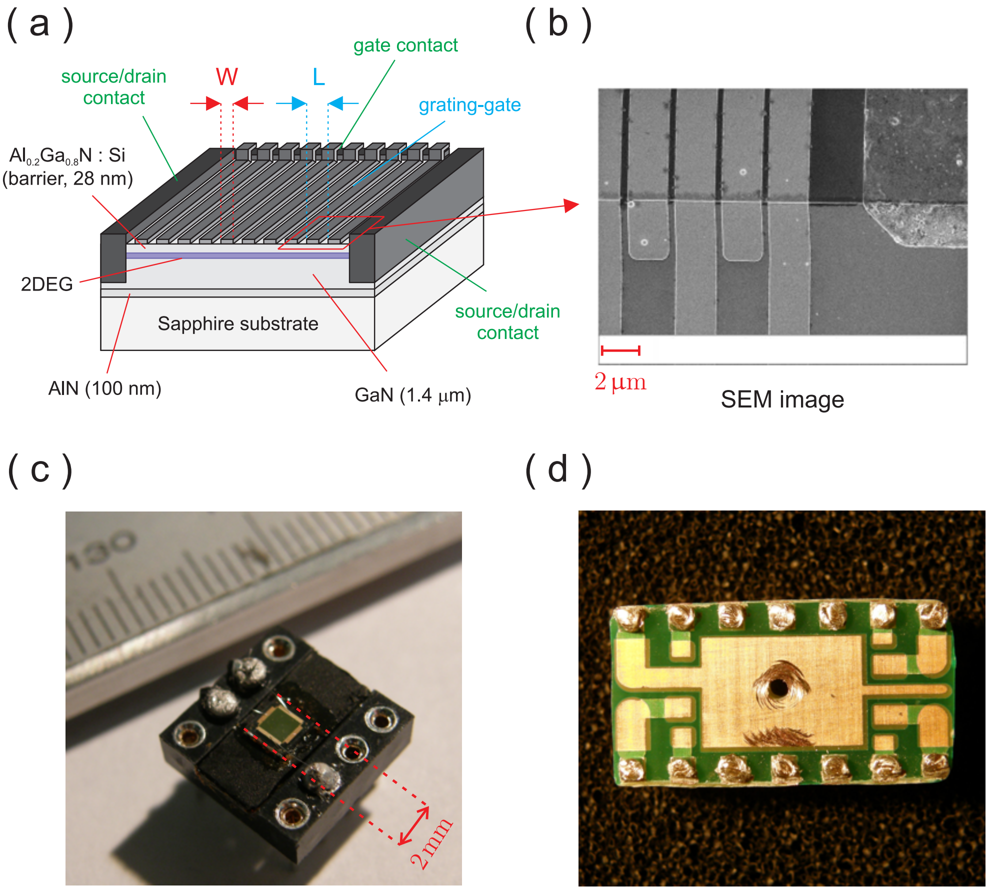

Figure 3.2: (a) Schematic illustration of the internal layout of a representative GaN/AlGaN sample under investigation. L and W denote the period of the grating-gate covering the sample's surface and the width of an individual metallic gate finger, respectively. (b) Scanning Electron Microscope (SEM) image of the region enclosed in diagram (a) by the parallelogram drawn in red (after [92]). (c) Image of one of the samples prepared for magnetotransmission measurements in the FTIR set-up. (d) Image of a sample holder used in magnetooptical experiments carried out with the aid of an optically pumped, far-infrared molecular laser operating on CH_3OH.

The internal layout of the GaN/AlGaN transistor structures that have been investigated within the framework of this PhD thesis is depicted in Fig. 3.2(a). The GaN/$Al_{0.2}Ga_{0.8}$N heterostructure used to fabricate our samples was grown on a (0001) sapphire substrate by conventional MOCVD [160] and Migration-Enhanced Metal-Organic Chemical Vapor Deposition (MEMOCVD$^{®}$) [162] techniques. The first one was applied to obtain a 1.4 μm-thick layer of undoped GaN. The remaining two layers: 100 nm-thick buffer layer made out of AlN and (28 ± 2) nm-thick $Al_{0.2}Ga_{0.8}N$ barrier layer, doped with Si to approximately $2 \times 10^{18}\,\mathrm{cm}^{-3}$, were deposited by means of the latter one. Both the GaN and $Al_{0.2}Ga_{0.8}N$ layers were grown Ga-face up in order to achieve the highest possible concentration of a 2DEG induced at the GaN/AlGaN interface by spontaneous and piezoelectric polarization [77–79]. We checked out their structures to be würizte with normal hexagonal orientation.

It is worth mentioning here that MEMOCVD® method has several important advantages over the widely-used MOCVD technique and is particularly well-suited for manufacturing devices with high aluminum content. The key difference between these two technologies lies in the way the source gases are introduced into the reaction chamber. In MEMOCVD® approach, a so-called step-flow mode of optimized waveforms and overlaps is utilized to separate ammonia and metalorganic molecules, what in turn reduces the likelihood of unwanted gas-phase reactions, which take place right above the substrate. As a result, the migration of gallium and aluminum adatoms on the substrate's surface becomes easier, what has a direct impact on the probability of their incorporation into the energy-favourable sites. The quality of the surface and the growth rate also increase (up to three times as compared to standard MOCVD method). The most important benefit is, however, a significantly reduced density of screw dislocations in thin nitride layers deposited by MEMOCVD® technique, which in the case of AlN can be even two orders of magnitude lower than in analogous films grown by MOCVD.

After completing the growth of the GaN/AlGaN wafer described above, $1.6 \times 1.6\,\mathrm{mm}^2$ mesas were defined on its top and the contacts for the source/drain and gate electrodes were fabricated using e-beam evaporated Ti/Al/Ti/Au and Ni/Au metal stacks, respectively. The choice of large dimensions as compared to other modern semiconductor structures, resulted from our intention to avoid equipping the final devices with additional antennas to collect the power of external electromagnetic field needed to excite the plasma waves. In the last but one step, the surface of each sample was covered with a gold grating of about 100 nm thickness and geometry characterized by the period L and an individual metallic finger's width W. According to our discussion from the beginning of this chapter, such a grating served both as a coupler between the plasmons and the incident electromagnetic radiation as well as a gate electrodes controlling the 2DEG density under the metallized sections. A Scanning Electron Microscope (SEM) image of a part of an example grating-gate is presented in Fig. 3.2(b). Finally, the processed wafer was cut into $2 \times 2\,\mathrm{mm}^2$ units ready for mounting on sockets shown in Figs. 3.2(c) and (d). The first one was used in magnetotransmission measurements performed with the aid of a Fourier-Transform Infrared

(FTIR) spectrometer whereas the second one was utilized in magnetotransport experiments and magnetooptical studies carried out in the set-up based on an optically pumped, far-infrared molecular laser operating on CH_3OH.

Both the growth of the GaN/AlGaN heterostruture and the fabrication of the grating-gate transistor structures were done at Sensor Electronic Technology, Inc. in Columbia, South Carolina, in the United States of America. In the following table we summarized the most important parameters of the samples that we had at our disposal, when conducting the research presented in the remaining part of this dissertation. Structure T0, not equipped with a grating-coupler, served us as a reference sample and was mainly used to normalize the magnetooptical spectra. As will be shown in the second part of the text, the role it played in the magnetotransport studies was also very important.

Name	L, µm	W, µm	S, µm	r	$N(V_\mathrm{g} = 0)$, cm^{-2}	$\mu(V_\mathrm{g} = 0)$, $\mathrm{cm}^2/\mathrm{Vs}$
T0	–	–	–	–	1.15×10^{13}	11700
T1	4.0	3.15	0.85	0.79	0.97×10^{13}	17000
T2	3.0	2.15	0.85	0.72	1.10×10^{13}	15400
T3	3.5	3.15	0.35	0.90	1.15×10^{13}	12200
T4	2.5	2.15	0.35	0.86	1.07×10^{13}	16100

Table 3.1: Geometrical parameters of the gratings and selected transport parameters of a 2DEG in the GaN/AlGaN structures under investigation. The values of 2DEG density ($N(V_\mathrm{g} = 0)$) and mobility ($\mu(V_\mathrm{g} = 0)$), extracted from magnetoresistance measurements performed at zero gate-voltage and described in the second part of the thesis, are given with relative uncertainty better than 5%.

Having described all technological issues related to the GaN/AlGaN structures that have been investigated by the author in the course of his PhD research, we would like now to discuss their physical properties. From electrical point of view, each of our samples except for T0, can be regarded as composed of connected in series single-gate field-effect transistors (FETs), similar to the one, whose cross-section is schematically presented in Fig. 3.3(a), prepared on the basis of illustration from p. 477 in [22]. It should be noticed, however, that the source and drain contacts in the form indicated in that diagram exist only for the first and the last transistor in a chain, respectively. For any intermediate section ascribed to a particular grating-gate finger they are just hypothetical boundaries used to distinguish this section from the neighbouring ones.

The principle of operation of a FET is explained on the band schemes depicted in Figs. 3.3(b) and (c). At thermal equilibrium, when no voltage is applied to the

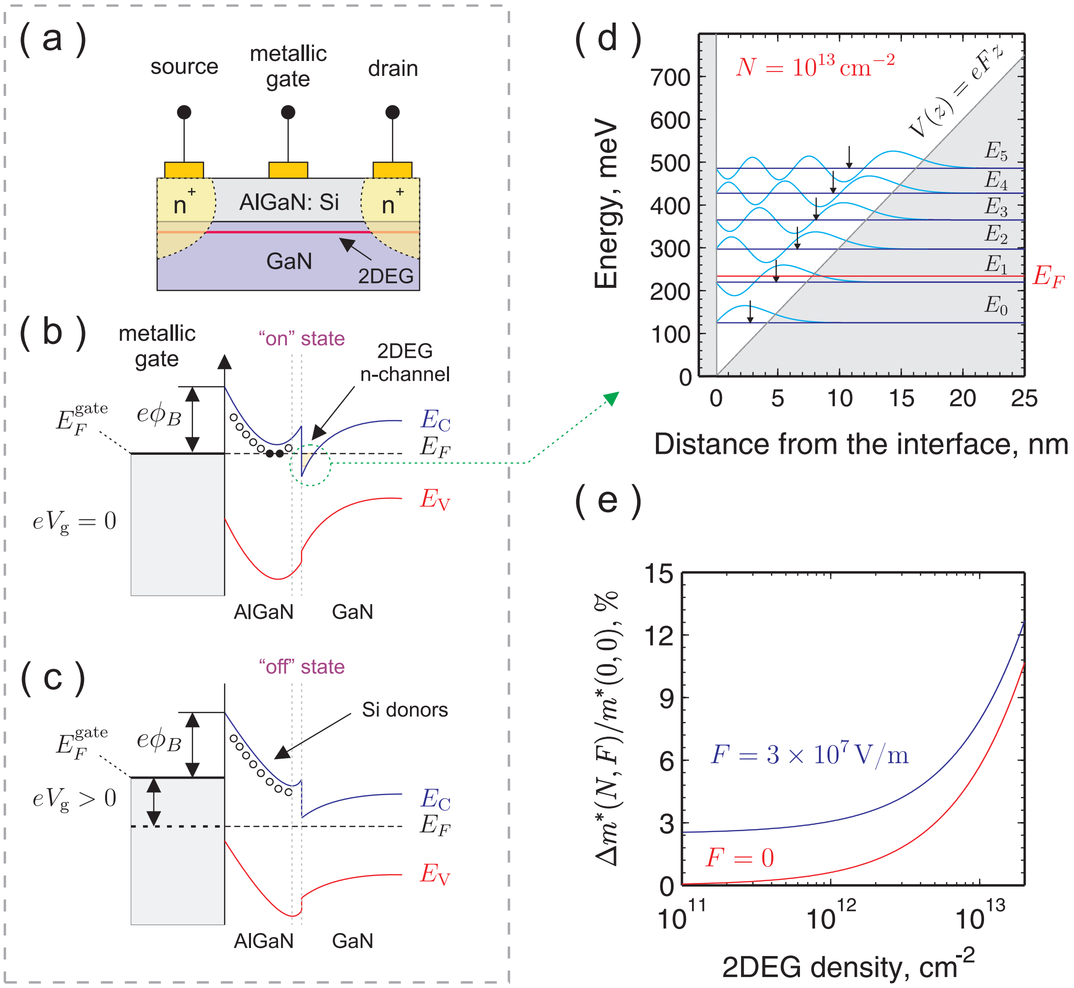

Figure 3.3: (a) Schematic cross-section of a typical, single-gate field-effect transistor (FET) based on the GaN/AlGaN heterostructure, with a conducting channel that is formed by a 2DEG connected to the source and drain contacts by highly n^+-doped regions. (b,c) The conduction (E_C) and valence (E_V) band profiles across the gated section of the FET from panel (a), plotted for two cases corresponding to the "on" and "off" state of a device, when depending on the negative value of the gate potential V_g, a triangular quantum well enclosed by a dashed green circle is either partially filled with electrons or totally empty. (d) The first six energy levels (solid dark-blue lines) and the corresponding unnormalized envelope functions (solid light-blue curves) of an electron in a triangular quantum well denoted schematically in diagram (b) and described by parameters taken from [32]. The solid red line represents a 2D Fermi level calculated with respect to the ground state (E_0) for a 2DEG density equal to $N = 10^{13}\,\text{cm}^{-2}$. For each state, the black arrow marks the mean distance of an electron from the GaN/AlGaN interface. (e) Non-parabolicity correction to the 2D effective mass of electrons occupying the ground state in a triangular quantum well from panel (d), calculated as a function of 2DEG density for two strengths of the electric field associated with the quantum well potential.

gate electrode, the spatial dependence of the conduction and valence band profiles in AlGaN barrier and GaN substrate layers resembles that shown in Fig. 3.3(b). As known from the fundamentals of solid-state-device physics [82, 83, 163], the bandbending results from the alignment of the Fermi level across the structure and the existence of built-in electrostatic potentials at the interfaces between the metallic gate and the AlGaN barrier (usually referred to as the Schottky barrier of height ϕ_B) as well as between the AlGaN barrier and the GaN substrate layer. The latter one gives rise to formation of a triangular quantum well in the conduction band, enclosed in Fig. 3.3(b) by a dashed green circle and subjected to more detailed analysis later on in this section. Since under the above conditions usually at least the ground state in the quantum well falls below the Fermi level denoted by E_F, the 2D channel of a FET is partially filled with electrons[5] and the device remains in a so-called "on" state. Upon application of a negative voltage to the gate, the Fermi level E_F^{gate} lifts with respect to E_F in the GaN/AlGaN heterostructure, causing a significant upward shift of the bands in the AlGaN barrier and a smaller one in the GaN substrate close to the GaN/AlGaN interface. As a results, the density of a 2DEG in the quantum well decreases. This process continues up to a certain value of V_g, below which the FET's channel becomes totally depleted of electrons, as shown in Fig. 3.3(c). Since no charge transfer between the source and drain electrodes is then possible, the state of a device changes from "on" to "off".

Fig. 3.3(d) displays the first six energy levels with the corresponding unnormalized electron envelope functions calculated for a triangular quantum well described by the parameters taken from [32], in particular, the electric field strength equal to $F = 3\times10^7\,\text{V/m}$. Because of a close affinity between the GaN/AlGaN heterostructure investigated in [32] and our samples, we claim that such an approach is fully justified. According to [80, 81, 164], the eigenenergies E_r and the unnormalized envelope functions $\phi_r(z)$ of an electron in a triangular quantum well described by:

$$V(z) = \begin{cases} \infty & \text{for} \quad z < 0, \\ eFz & \text{for} \quad z \geqslant 0, \end{cases} \tag{3.6}$$

where $z = 0$ corresponds to the GaN/AlGaN interface, can approximately[6] be expressed as:

$$E_r = \left(\frac{\hbar^2 e^2 F^2}{2m^*}\right)^{1/3} \cdot \left[\frac{3}{2}\pi\left(r + \frac{3}{4}\right)\right]^{2/3}, \tag{3.7}$$

$$\phi_r(z) = \text{Ai}\left[\left(\frac{2m^* eF}{\hbar^2}\right)^{1/3} \cdot \left(z - \frac{E_r}{eF}\right)\right], \tag{3.8}$$

---

[5] In GaN/AlGaN samples with high carrier concentration (like in our ones), the electrons occupying states in the quantum well are induced by spontaneous and piezoelectric polarization [77–79] as well as come from intentional doping of the AlGaN barrier with donors.

[6] With a few percent accuracy.

where $r = 0, 1, 2, ...$ and Ai[...] denotes the Airy function of an argument enclosed by the square brackets[7] [165]. They are plotted in Fig. 3.3(d) with solid dark-blue lines and light-blue curves, respectively. For each state, the mean distance of an electron from the GaN/AlGaN interface can be evaluated with the use of the following formula

$$\overline{z}_r = \frac{2E_r}{3eF}. \tag{3.9}$$

The values corresponding to the respective energy levels are marked in Fig. 3.3(d) with black arrows. In particular, it is worth noticing that $\overline{z}_0 = 2.77\,\mathrm{nm}$. Finally, the red line represents a 2D Fermi level calculated from $E_F = \hbar^2\pi N/m^*$ [22–24] with respect to the state E_0 for a 2DEG density equal to $N = 10^{17}\,\mathrm{cm}^{-2}$.

There are three main conclusions resulting from Fig. 3.3(d). First of all, in most of our GaN/AlGaN samples, the assumption of electrons occupying only the lowest-lying subband in a triangular quantum well might not be satisfied for the highest densities of 2DEG, corresponding to zero or small negative electrical polarization of the gate electrode. Because of somehow arbitrary choice of the electric field strength and a relatively small energy difference between the Fermi level and the first electronic subband (E_1) above the ground state, we shall not, however, take this uncertainty into account when interpreting the results of magnetooptical measurements. Nevertheless, we have to remember that this simplification may in general lead to some discrepancies between the experimental data and the model description. Secondly, in accordance with almost 100 meV energy separation between the E_0 and E_1 subbands, exceeding four times the energy range probed in our magnetospectroscopic studies (3–25 meV), we can completely reject the probability that any part of our results comes from the interband magnetoplasmon excitations. Finally, in connection with (3.9), the thickness of the AlGaN barrier required for evaluation of the resonant frequencies of the 2D magnetoplasma waves has to be increased in the simplest approximation by about 3 nm with respect to its technological value, in order to take into account the fact that electrons occupying the lowest-lying subband in a triangular quantum well do not reside exactly at the GaN/AlGaN interface.

The last but not least correction that should be included in a realistic description of the experimental data presented in the remaining part of this dissertation, is related to the non-parabolicity of the conduction band profile, which affects the electron effective mass. In a two-band approximation [98] it can be written as:

$$m^*(E) = m_0^*\left(1 + 4\frac{E}{E_\mathrm{g}}\right)^{1/2}, \tag{3.10}$$

---

[7] Eq. (3.8) in [80] is written in an incorrect form (see Eq. (3.23)), i.e. the numerical prefactor in the first parentheses is not raised to the power 1/3.

where E_g denotes the energy gap ($E_\mathrm{g} = 3.5\,\mathrm{eV}$ in the case of GaN), m_0^* is the effective mass at the bottom of the conduction band and $m^*(E)$ represents the mass of carriers with energy E with respect to the bottom of the conduction band [166]. For an electron occupying the ground state in a triangular quantum well, the above expression takes on the form:

$$m^*(N,F) = m^*(0,0)\left(1 + 4\frac{\langle K(N,F)\rangle_0 + E_F(N,F)}{E_\mathrm{g}}\right)^{1/2}, \tag{3.11}$$

where N stands for the 2DEG density, F is the strength of an electric field associated with the quantum well potential, $m^*(0,0) \equiv m^*(N=0,F=0) = m_0^*$ and $\langle K(N,F)\rangle_0$ denotes the expectation value of the electron's kinetic energy in the motion perpendicular to the quantum-well plane. According to [166], $\langle K(N,F)\rangle_0 \simeq E_0(N,F)/3$, where from Eq. (3.7):

$$E_0(N,F) = \frac{3}{8}\left(\frac{3h^2e^2F^2}{m^*(N,F)}\right)^{1/3}. \tag{3.12}$$

Since both $E_0(N,F)$ and $E_F(N,F)$ depend explicitly on the corrected effective mass $m^*(N,F)$, the estimation of its value for a given 2DEG density and an electric field strength treated as a constant parameter, has to be done in a self-consistent manner. The results of such calculations, performed for $F = 3\times10^7\,\mathrm{V/m}$ (solid blue curve) and $F = 0$ (solid red curve)[8] are presented in Fig. 3.3(e). The quantity $\Delta m^*(N,F)/m^*(0,0)$ laid off on the vertical axis, stems directly from Eqs. (3.11) and (3.12)

$$\frac{\Delta m^*(N,F)}{m^*(0,0)} \equiv= \frac{m^*(N,F) - m^*(0,0)}{m^*(0,0)} = \left\{1 + \frac{4}{E_\mathrm{g}}\left(E_F(N,F) + \frac{E_0(N,F)}{3}\right)\right\}^{1/2} - 1.$$

Although obtained for analogous parameters and with the use of exactly the same formulae, the trace of $F = 3\times10^7\,\mathrm{V/m}$ curve in Fig. 3.3(e) slightly differs from that in [32]. We have made several attempts to figure out the origin of discrepancies, but none of them showed that our simulations are wrong. Furthermore, we compared their predictions for a GaAs/AlGaAs heterostructure with [166]. Since almost a perfect agreement between the two was found, we concluded that there is no significant programming mistake in our routine utilized to prepare Fig. 3.3(e).

As can be seen, for 2DEG densities on the order of $10^{13}\,\mathrm{cm}^{-2}$ a correction to the electron effective mass due to non-parabolicity of the conduction band approaches 10% in a GaN/AlGaN heterostructure like the one investigated within the framework of this PhD thesis. Moreover, as noticed by T. Ando in [166], the experimentally

---

[8] The case with $F = 0$ is somehow artificial, since for zero electric field there is no quantization of the electron's motion in the growth direction. Nevertheless, it can still be considered as an oversimplified but instructive model of a very thin epilayer of GaN.

observed value is always 10–20% larger than the theoretical estimation based on Eq. (3.10), mainly because of the fact that it disregards the contribution coming from the electron-phonon interaction. Taking this into account, the effective mass of electrons extracted from the magnetooptical data collected on GaN/AlGaN structures containing a 2DEG, whose density exceeds $10^{13}\,\mathrm{cm}^{-2}$, can be as large as $0.25\,\mathrm{m}_0$.

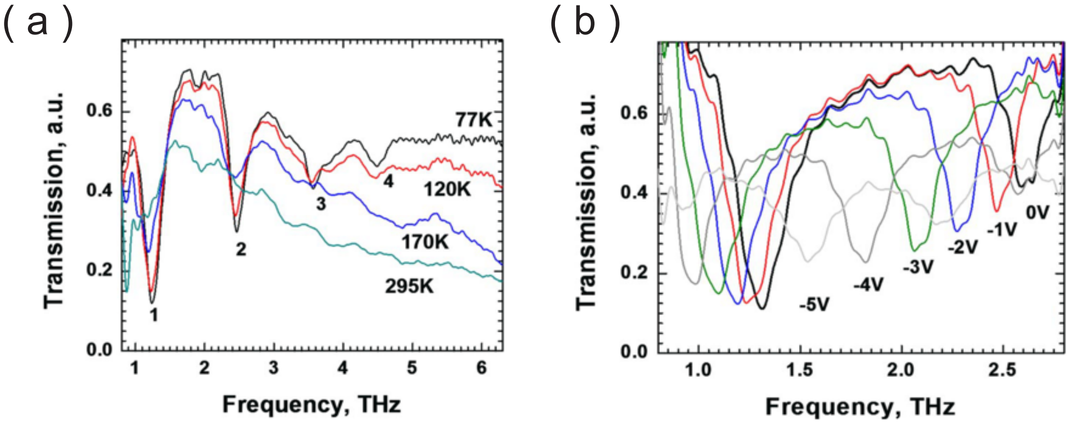

Figure 3.4: (a) Transmission spectra of the GaN/AlGaN transistor structure equipped with a grating gate of 1.5 µm period and an individual metallic finger's width equal to 1.15 µm. All the experimental curves, recorded at different temperatures and zero voltage applied to the gate electrode, are referenced to the free space. (b) Transmission spectra of the same GaN/AlGaN sample as in panel (a), measured at 77 K for different electrical polarizations of the gate electrode. Both figures are reprinted from [94].

In the last part of this section we would like to briefly discuss the results of the first optical experiments performed on a sample manufactured on the basis of exactly the same GaN/AlGaN heterostructure as our devices, but equipped with a grating-gate of 1.5 µm period (shorter as compared to any of the couplers that we had at our disposal) and the width of an individual metallic finger equal to 1.15 µm [94]. They were carried out with the use of a standard FTIR spectrometer and no magnetic field applied to the sample. As shown in Figs. 3.4(a) and (b), the authors analysed the temperature and gate-voltage dependence of transmission spectra exhibiting a series of well-developed minima occurring for $T \leqslant 170\,\mathrm{K}$. By analytical and numerical methods they proved them to originate from excitation of plasmon resonances (up to the fourth order), extending over the whole period of a grating-gate, but due to a relatively large mark fraction ($r = 0.77$), mostly determined by the gated parts of a 2DEG. As mentioned in the introduction to this chapter, their findings motivated us to extend the research they have initiated to magnetoplasma waves, which have not been yet systematically explored in the GaN-based systems.

Chapter 4

Experimental techniques and results of measurements

In Chapters 1 and 2 we introduced the theoretical background of the magnetoplasmon excitations as well as the magnetotransport properties of a 2DEG embedded in a semiconductor heterostructure. Furthermore, we pointed out the goals for the experimental part of this thesis, showing the model predictions we wanted to verify and the important parameters that we were interested in when carrying out the research. A major part of Chapter 3 was devoted to detailed presentation of the grating-gate GaN/AlGaN samples that we have chosen as an object of the study, since many of the magnetoplasma effects have not yet been systematically explored in structures based on this material. Thus, the aim of the following chapter is to supplement the aforementioned issues with description of the experimental techniques we utilized in the course of our magnetotransport and magnetospectroscopic investigations, as well as with the results of measurements, their interpretation and discussion of the analytical tools that were applied to extract from them the valuable information.

4.1 Magnetotransport measurements

4.1.1 Experimental set-up and raw data treatment

All the magnetotransport measurements were carried out at the Faculty of Physics of the University of Warsaw, in the experimental set-up which is schematically depicted in Fig. 4.1. Two DC voltage sources (Keithley 2400) were connected to one of the side contacts of the sample (drain) and to the overlaid grating-gate, respectively, whereas the second side contact (source) was kept at the ground potential. The sample was mounted at the end of about 1.2 m–long probe, enclosed within a protective tube made out of steel and filled in with gaseous helium of ambient pressure at room temperature. During measurements, the tube was placed in a cryostat and partially immersed in liquid helium in such a way that the sample was located in the center

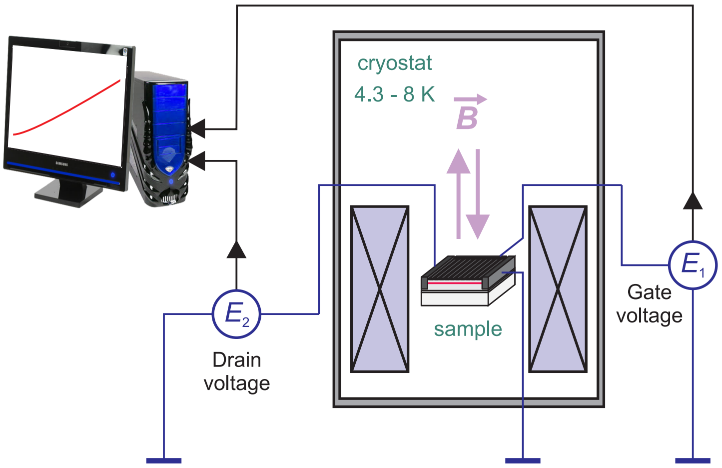

Figure 4.1: Schematic illustration of the experimental set-up used for magnetotransport measurements.

of a superconducting coil generating magnetic fields of maximally 10 T-strength (at 4.2 K) and a reversible direction. Within an experimental accuracy, the orientation of the magnetic field was perpendicular to the sample's surface. In order to monitor the temperature of the system under investigation we utilized a precisely calibrated Cernox thermometer stuck to a brass component of the probe about 3 mm above the sample. After 5 min. from putting the tube into the cryostat, the reading of the thermometer was reaching a stable value of 4.3 K. All the measurements done for the structure T0 (without a grating-coupler) were carried out at exactly this temperature. On the other hand, substantial leakage currents flowing through the barriers of grating samples each time a non-zero electric potential was applied to their gate electrodes, caused a noticeable drift of the temperature when sweeping the magnetic field. For the most negative gate-voltage used during magnetotransport experiments (-3.2 V), we observed a continuous decrease in the temperature from about 8 K at $B = 0$ to 4.3 K at $B = 10$ T. Because of this disadvantage of our GaN/AlGaN structures, we haven't attempted any temperature-dependent studies of their properties (possible with the aid of a so-called Variable Temperature Insert) as well as a low-current AC mode of magnetotransport measurements.

All the results discussed in the following part of the present section were obtained in a constant-voltage configuration, in which a drain current, I_d, understood as a current entering the 2DEG layer through the drain electrode, and a gate current, I_g, were recorded as a function of the magnetic field under a 100 mV potential applied to the drain contact and a given potential of the grating-gate. By considering both orientations of the magnetic field, we were able to determine the symmetric and anti-symmetric part of the currents:

$$I_{d(g)}^{\text{sym.}}(B) = \frac{I_{d(g)}(B) + I_{d(g)}(-B)}{2} \qquad I_{d(g)}^{\text{asym.}}(B) = \frac{I_{d(g)}(B) - I_{d(g)}(-B)}{2}$$

however, only the former one was subjected in the next step to further analysis. Because of the relation $I_{d(g)}^{\text{sym.}}(B) \gg I_{d(g)}^{\text{asym.}}(B)$ satisfied for all the samples under investigation, we ascribe the $I_{d(g)}^{\text{asym.}}(B)$ components to some inhomogeneity of the electrical leads and the gate electrode, which is practically unavoidable in the case of structures with the side lengths as large as hundreds of micrometers. Furthermore, we focused on the drain current as certainly flowing only in directions perpendicular to the applied magnetic field. The gate current served us merely to calculate a source current when we wanted to verify the conclusions drawn for $I_d^{\text{sym.}}(B)$ data that were expected to hold also for the current leaving or entering the sample from the source side.

In order to separate the classical (non-oscillating) contribution to the $I_d^{\text{sym.}}(B)$ traces from the oscillating one related to quantum effects, we numerically determined an upper (UP-EN) and lower (LOW-EN) envelope for each $I_d^{\text{sym.}}(0)/I_d^{\text{sym.}}(B)$ curve. This task was accomplished with the aid of a simple script based on an iterative smoothing of the original data by the Savitzky-Golay filter [167] that after each intermediate step i was followed by constructing a new input trace (for the step $i+1$) in accordance with the conditions:

$$\begin{aligned}
\text{UP-EN}_{\text{out}}^{i}(B) \geqslant I_d^{\text{sym.}}(0)/I_d^{\text{sym.}}(B) &\Rightarrow \text{UP-EN}_{\text{in}}^{i+1}(B) = \text{UP-EN}_{\text{out}}^{i}(B),\\
\text{UP-EN}_{\text{out}}^{i}(B) \leqslant I_d^{\text{sym.}}(0)/I_d^{\text{sym.}}(B) &\Rightarrow \text{UP-EN}_{\text{in}}^{i+1}(B) = I_d^{\text{sym.}}(0)/I_d^{\text{sym.}}(B),\\
\text{LOW-EN}_{\text{out}}^{i}(B) \geqslant I_d^{\text{sym.}}(0)/I_d^{\text{sym.}}(B) &\Rightarrow \text{LOW-EN}_{\text{in}}^{i+1}(B) = I_d^{\text{sym.}}(0)/I_d^{\text{sym.}}(B),\\
\text{LOW-EN}_{\text{out}}^{i}(B) \leqslant I_d^{\text{sym.}}(0)/I_d^{\text{sym.}}(B) &\Rightarrow \text{LOW-EN}_{\text{in}}^{i+1}(B) = \text{LOW-EN}_{\text{out}}^{i}(B),
\end{aligned}$$

where subscripts 'out' and 'in' refer to the state after the i-th and before the $(i+1)$-th iteration, respectively. Usually, about 200 steps were sufficient to obtain the well-shaped envelopes. Having them at hand, the non-oscillating and oscillating parts of the $I_d^{\text{sym.}}(0)/I_d^{\text{sym.}}(B)$ curve were readily calculated as:

$$\left(\frac{I_d(0)}{I_d(B)}\right)_{\text{non-osc.}} = \frac{\text{LOW-EN}(B) + \text{UP-EN}(B)}{2}, \tag{4.1}$$

$$\left(\frac{I_d(0)}{I_d(B)}\right)_{\text{osc.}} = \frac{I_d(0)}{I_d(B)} - \frac{\text{LOW-EN}(B) + \text{UP-EN}(B)}{2}, \tag{4.2}$$

where for the sake of clarity we have dropped out the superscript 'sym.'. At the final stage, the first one of them (Eq. (4.1)) was subjected to analysis from the point of view of the geometrical megnetoresistance effects and the momentum relaxation time, whereas the second one served us for estimating the 2DEG density (from the power spectrum of a Fast Fourier Transform (FFT) of the SdH oscillations) as well as the quantum relaxation time, determined on the basis of Dingle's plot discussed in detail in Chapter 2.

4.1.2 Experimental results

4.1.2.1 Reference structure without a grating-gate

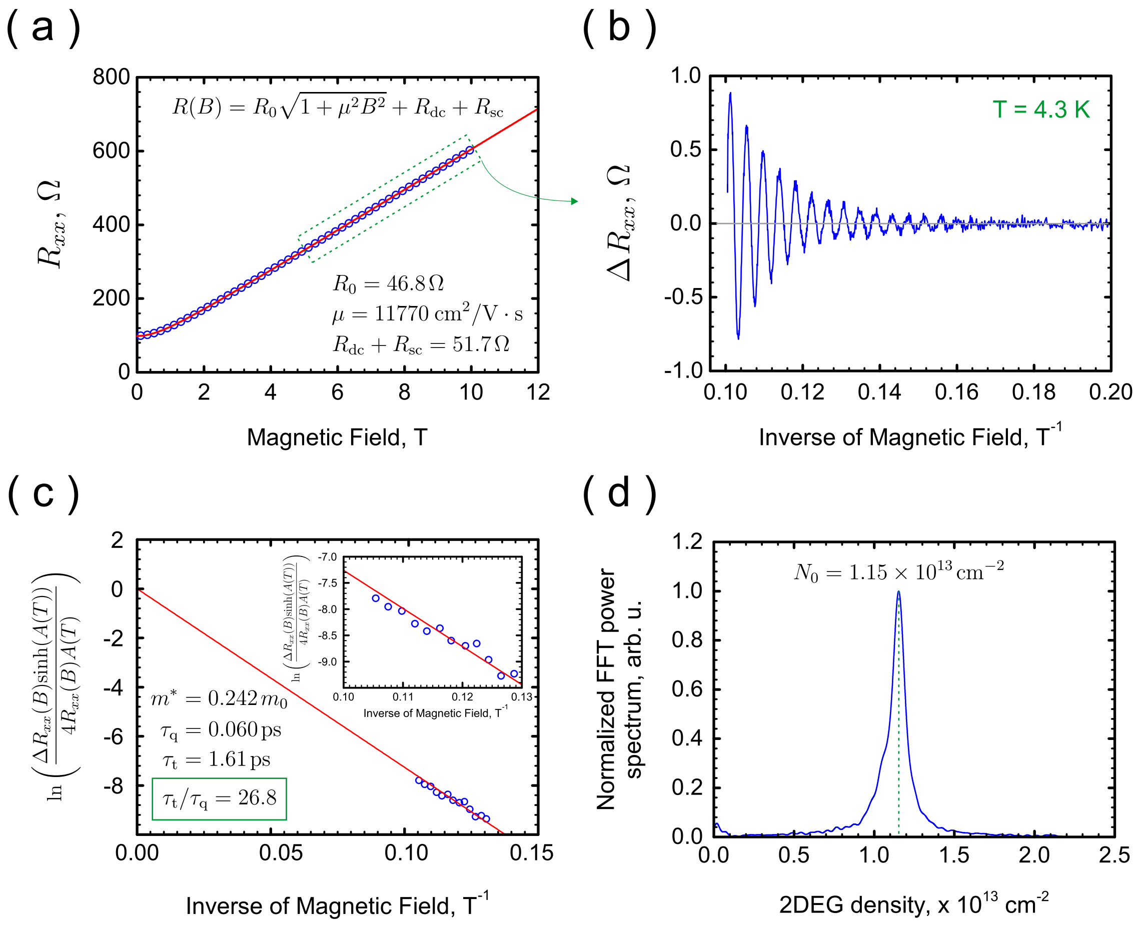

Figure 4.2: Results of magnetotransport measurements performed on the sample T0: (a) A comparison between the representative trace of the transverse magnetoresistance, $R_{xx}(B)$, (open blue circles) and the model predictions (solid red curve) resulting from the classical (non-scillating) part of Eq. (2.19) with R_{sc} and R_{dc} terms added to account for finite resistances of the source and drain electrodes. (b) The Shubnikov-de Haas (SdH) oscillations extracted from the high-field part of the data presented in panel (a) (see the rectangle drawn with dashed green line), and plotted versus the reciprocal magnetic field. (c) A so-called Dingle's plot of the first twelve extrema of the SdH oscillations from graph (b) (open blue circles), fitted with a straight red line given by Eq. (2.23). (d) A normalized Fast-Fourier-Transform (FFT) power spectrum of the SdH oscillations from diagram (b), with a well-developed peak of approximately Lorentzian shape, which indicates the presence of a single conductivity channel in the sample, with a 2DEG's density $N_0 = 1.15 \times 10^{13}\,\mathrm{cm}^{-2}$.

Figure 4.2 summarizes the results of magnetotransport measurements performed on the sample T0, i.e. the reference structure with no grating-coupler. In panel (a) we present the symmetrized resistance, $R_{xx}(B) = V_d/I_d(B)$, recorded as a function of the magnetic field for $V_d = 100\,\mathrm{mV}$ applied to the drain contact. We have checked that the shape of the registered curve does not change at all for V_d down to 10 mV. Open blue circles denote the experimental data. A model curve resulting from Eq. (2.10), written for $L = W = 1.6\,\mathrm{mm}$ and with a small modification added to account for finite resistances of the source-to-channel (R_{sc}) and drain-to-channel (R_{dc}) contacts, is drawn in red. The values of fitted parameters are given in the bottom right corner of the graph. As can be seen, the agreement between the model predictions and the results of measurements is highly satisfactory. From the estimated mobility, the momentum relaxation time, τ_t can readily by calculated and, provided that $m^* = 0.242m_0$, in accordance with the discussion on the non-parabolicity effects presented in Chapter 3, it equals to $\tau_\mathrm{t} = 1.61\,\mathrm{ps}$. When collated with reports of other researchers, it looks very similar to values given in [168, 169] for concentrations of a 2DEG, but different widths of the AlGaN barrier, and is proportionally lower than in [170, 171]. In Fig. 4.2(b) we show the oscillating part of the resistance from panel (a) (note the rectangle drawn with dashed green line), plotted as a function of the reciprocal magnetic field. When Fourier-transformed into the frequency domain (see diagram (d)), it appears as a well-developed peak of approximately Lorentzian shape, which in agreement with Eq. (2.15) corresponds to a sheet density of a 2DEG that equals to $N_0 = 1.15 \times 10^{13}\,\mathrm{cm}^{-2}$. It is worth emphasizing, that within a 2%–accuracy, this value matches the one that can be derived from the relation: $R_0 = 1/Ne\mu$ and the parameters listed in Fig. 4.2(a). Finally, in Fig. 4.2(c) we display the Dingle plot based on the first twelve extrema of the SdH oscillations depicted in panel (b). Like previously, open blue circles represent the experimental points, whereas the straight line drawn in red results from fitting them with expression (2.23). A value of the quantum relaxation time estimated with the aid of this plot ($\tau_\mathrm{q} = 0.06\,\mathrm{ps}$) is surprisingly low – similar to reported in [168], but for substantially shorter momentum relaxation times, and significantly lower than in [170, 171]. In consequence, the $\tau_\mathrm{t}/\tau_\mathrm{q}$ ratio reaches the level of almost 29. Although such a large discrepancy between τ_t and τ_q is nothing particularly unusual in the literature of the subject (see for example [172]), it has been observed so far only for very high-mobility modulation-doped 2DEGs in AlGaAs/GaAs heterostructures, where the small-angle scattering events indeed strongly dominate over the large-angle ones. Here, we think that a high value of the $\tau_\mathrm{t}/\tau_\mathrm{q}$ ratio has a twofold origin. Firstly, it can partially come from small density fluctuations in the 2DEG layer, which in the case of samples with $1.6 \times 1.6\,\mathrm{mm}^2$ surface are not only probable, but even highly expected. As demonstrated by S. Syed and co-workers [173], the inhomogeneities on the order of 3% can give rise to artificial reduction in τ_q by a factor of 6, if it is estimated on the basis of Dingle's plot prepared under an assumption of perfect homogeneity of a 2DEG. However, as will be shown in the next paragraph, the contribution from the small-angle scattering caused by the acceptor-like surface states present on top of the AlGaN barrier [174, 175], cannot be excluded as well.

4.1.2.2 Grating-gate samples: 2DEG density and quantum relaxation time

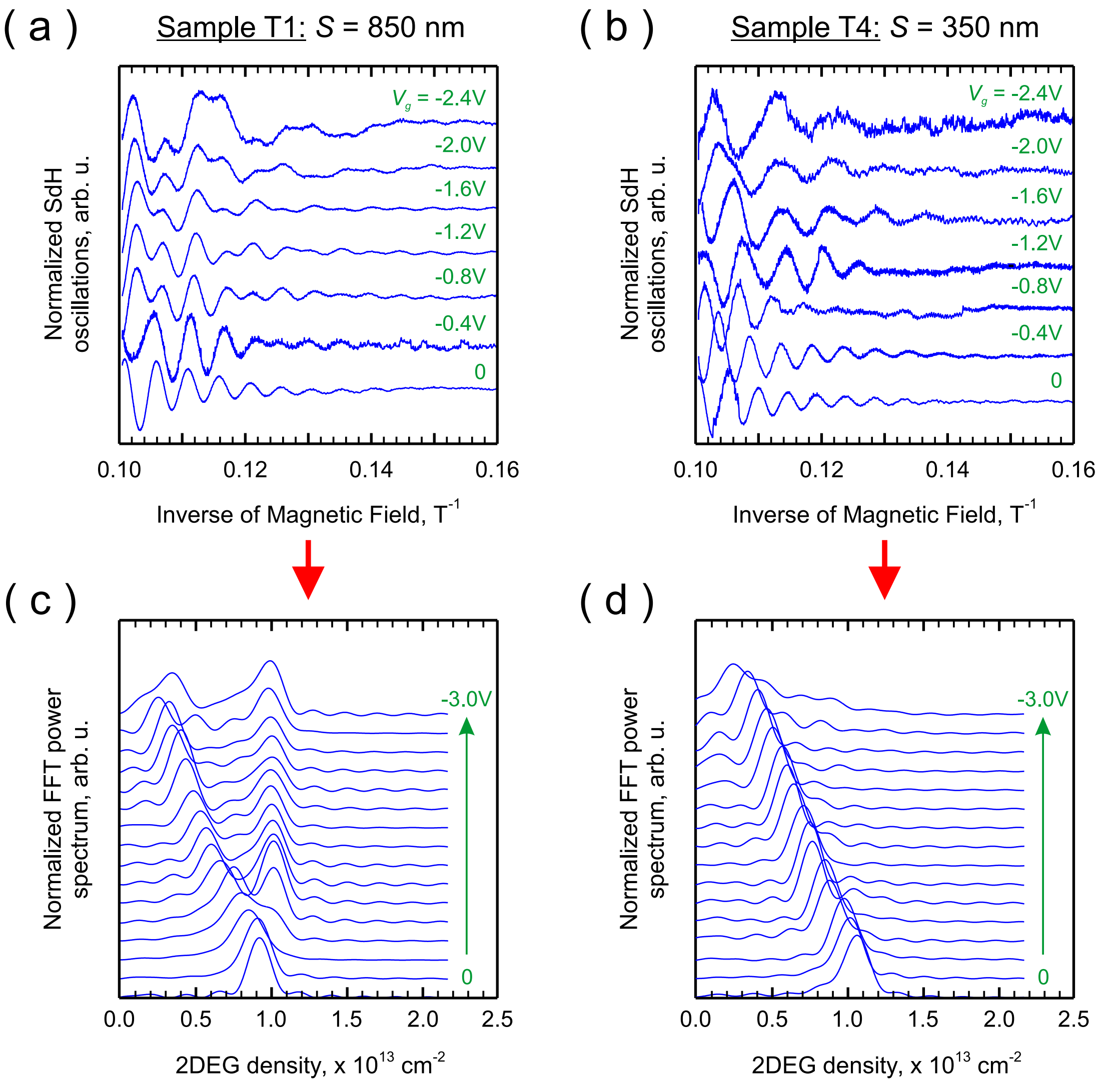

Figure 4.3: (a) and (b): Traces of the SdH oscillations recorded for various gate voltages on the samples T1 and T4, equipped with grating-gates of different geometry, in particular, the slit S between the adjacent gate's fingers. (c) and (d): Normalized FFT power spectra of the SdH oscillations from diagrams (a) and (b), indicating the presence of the 2DEG density modulation in the structure with larger S and the lack of such a modulation in the structure with smaller S.

In Fig. 4.3 we present the traces of the SdH oscillations (panels (a) and (b)) and the results of their Fourier transform (diagrams (c) and (d)) obtained for two samples: T1 and T4, equipped with grating gates of different periods and widths of an individual metallic gate's stripe (refer to Table 3.1 for details). Since all the features displayed in the sub-plots (a) and (c) can also be found in the results of magnetotransport measurements performed on the sample T2, whereas those from graphs (b) and (d) are equally well exhibited by the sample T3, we claim that a crucial parameter for the following analysis is the slit, S, between the adjacent fingers of the gate electrode. In the case of structures T1 and T2 it was equal to 850 nm. In samples T3 and T4, the neighbouring fingers of the grating-coupler were separated from each other by 350 nm. As can be seen, the gate-voltage (V_g) evolution of the SdH oscillations pattern is more complicated for the sample T1. With decreasing V_g they undergo a transition from the single-period ones to composed of more than one component, what results in appearance of clearly visible beatings. The power spectrum of FFT (see Fig. 4.3(c)) confirms this observation, displaying in general two peaks - one that is practically insensitive to the voltage applied to the gate electrode, and the second one, which, to a good approximation, linearly shifts with V_g towards 0, indicating a decrease in the density of a carrier population it corresponds to. It is worth emphasizing that with no doubt, both peaks merge into a single one at $V_g = 0$. In contrast, a much simpler behaviour is exhibited by the sample T4. Here, only the V_g–sensitive component of the SdH oscillations is visible in both the $\Delta(I_d(0)/I_d(B))$ traces plotted as a function of $1/B$ (panel (b)) as well as in their Fourier transforms presented in diagram (d). When combined with the results obtained on the sample T0, for which no signs of parallel conductivity have been found, the above observations indicate a gate-voltage induced splitting of the initially uniform[1] 2DEG layer into regions with higher and lowed density. In accordance with different sensitivity to V_g, we identify the former group with the openings of the gate electrode, whereas the latter one with the 2D electron channel sections that are located under the metallic stripes. The only point which surprises in this explanation is the minimal separation, $S_{\min}$, between the gate fingers, that is required to create a density modulation in the 2DEG layer. From the above analysis it is clear that $850\,\text{nm} \geqslant S_{\min} > 350\,\text{nm}$. However, as well known from the physics of electronic devices [82, 176], a so-called electric-field-fringing-effect, which leads to effective extension of the geometrical size of the gate, so that in reality it influences the electron gas not only in the zone that is placed directly beneath the metallic film but also slightly beyond this area, takes place in each direction over distances as large as the width of the barrier (or, equivalently, the gate-to-channel separation), i.e. 28–30 nm in the case of our samples. In GaN/AlGaN heterostructures, the diffusion of carriers in the presence of a density gradient plays a less important role than the fringing effect, and in consequence only slightly enlarges the value given above [177]. From this analysis, $S_{\min}$ should be equal to 60–100 nm, what is far even from the lower bound (350 nm) resulting from our magnetotransport measurements. In order to solve this puzzle, the surface states mentioned in the

---

[1] Within an accuracy discussed in the previous paragraph.

preceding paragraph have to be recalled again. As shown in [174, 175, 178] they are of acceptor-like type and can be efficiently charged by the gate-leakage current, thus acting as a 'virtual' gate controlling the density of a 2DEG in exactly the same way as an electrically polarized metallic film. Such a process can take place over distances as large as 500 nm, counting from the edge of a gate electrode [179]. This observation perfectly fits our findings, since all the grating-gate samples discussed in the present thesis exhibited substantial leakage currents even for $V_g = 0$.

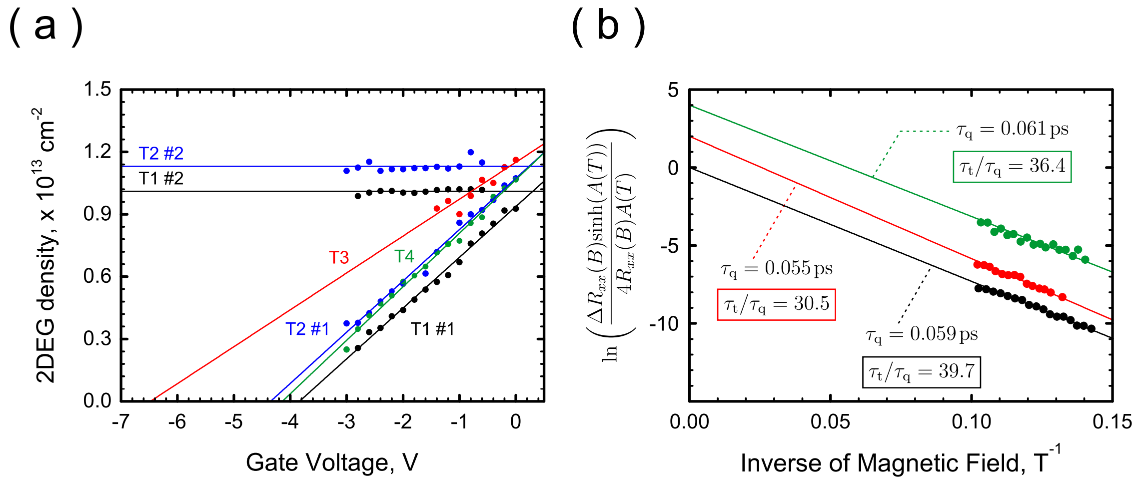

Figure 4.4: (a) Positions of peaks from the FFT power spectra of the SdH oscillations (solid circles), plotted as a function of the gate voltage for all the samples under investigation. The solid straight lines drawn with the same colors as the experimental points they correspond to, result from fitting the data with Eq. (4.3). The estimated values of the fitting parameters are collected in Table 4.1. (b) Dingle's plots of the SdH oscillations extrema recorded for the samples T1, T3 and T4 (solid circles) at $V_g = 0$, shown along with the model lines described by Eq. (2.23). Note a vertical shift by 2 and 4 in both the data and the fitted dependence, added to the results obtained for the structures T3 and T4, respectively, in order to make the graph more legible.

Figure 4.4(a) shows the positions of peaks from the FFT power spectra (solid circles), plotted as a function of the gate voltage for each of the structures under investigation. As can be seen, a linear dependence between V_g and the density of a 2DEG holds for all the data collected in the graph. This type of behaviour is typical for field-effect transistors with narrow barriers, in which the gate-control over the 2DEG concentration can successfully be described within a plane capacitor approximation that states:

$$N(V_g) = \frac{\varepsilon_{\mathrm{b}}\varepsilon_0}{ed}\left(V_g - V_{th}\right) = N_0\left(1 - \frac{V_g}{V_{th}}\right), \tag{4.3}$$

where: ε_0 is the dielectric permittivity of the free space, ε_{b} denotes the static dielectric constant of the barrier layer of thickness d, V_{th} is the so-called threshold voltage at

Name	N_0, $\times 10\,\mathrm{cm}^{-2}$	V_{th}, V	ε_b
T1 #1	9.4 ± 0.1	-3.83 ± 0.11	12.4 ± 0.3
T1 #2	10.1 ± 0.1	–	–
T2 #1	10.7 ± 0.1	-4.35 ± 0.14	12.5 ± 0.4
T2 #2	11.3 ± 0.1	–	–
T3	11.5 ± 0.2	-6.5 ± 1.1	9.0 ± 1.5
T4	10.7 ± 0.1	-4.14 ± 0.10	13.1 ± 0.3

Table 4.1: Estimations of the zero-gate-voltage concentration (N_0), threshold voltage (V_{th}) and the static dielectric constant of the the AlGaN barrier (ε_{textb}), obtained by fitting the experimental results depicted in Fig. 4.4 with the model dependence described by Eq. (4.3).

which the electron channel of a transistor becomes totally depleted of charge carriers, and $N_0 = N(V_g = 0)$ represents the density of a 2DEG for electrically unpolarized gate. The straight lines in Fig. 4.4 result from fitting the experimental points with the above formula. The values of adjustable parameters (N_0 and V_{th}) are given in the following table along with the estimation of ε_b, obtained under an assumption that $d = 28$nm, as mentioned in Chapter 3 when discussing the layout of the GaN/AlGaN structures under study.

In Fig. 4.4(b) we show the Dingle plots drawn on the basis of the SdH oscillations recorded on various samples at $V_g = 0$. The lack of data for the structure T2 is a consequence of very noisy traces of oscillations extracted from measurements done at zero gate voltage and inability to use the curves registered at $V_g = -0.2\,\mathrm{V}$ because of clearly visible beatings arising from modulation of the 2DEG density. The closed circles with colors corresponding to panel (a) denote the experimental results, while the solid straight lines illustrate the model dependency described by Eq. (2.23). In order to make the graph more legible, both the experimental points and fitted lines are vertically shifted for the samples T3 and T4 by 2 and 4, respectively. As can be seen, the estimated values of quantum relaxation time are almost the same as in the case of structure T0. Due to higher mobilities (refer to Table 3.1), the $\tau_\mathrm{t}/\tau_\mathrm{q}$ ratios are, however, increased by 14–48 %, what on one hand may reflect an enhanced scattering from the surface states, whereas on the other one, a further degradation of the 2DEG uniformity. The first mechanism is in our opinion of greater importance, since as figured out by numerical simulations of the electric potential distribution in the channel of a leaky-gate field-effect transistor, that we have performed with the use of a slightly modified 2D resistor-network model proposed by D. C. Look and T. A. Cooper [180], the maximal relative variation in the 2DEG concentration that originates from the presence of a substantial gate current is less than 0.5 % for $V_g = 0$.

4.1.2.3 Grating-gate samples: leakage-current-enhanced geometrical magnetoresistance

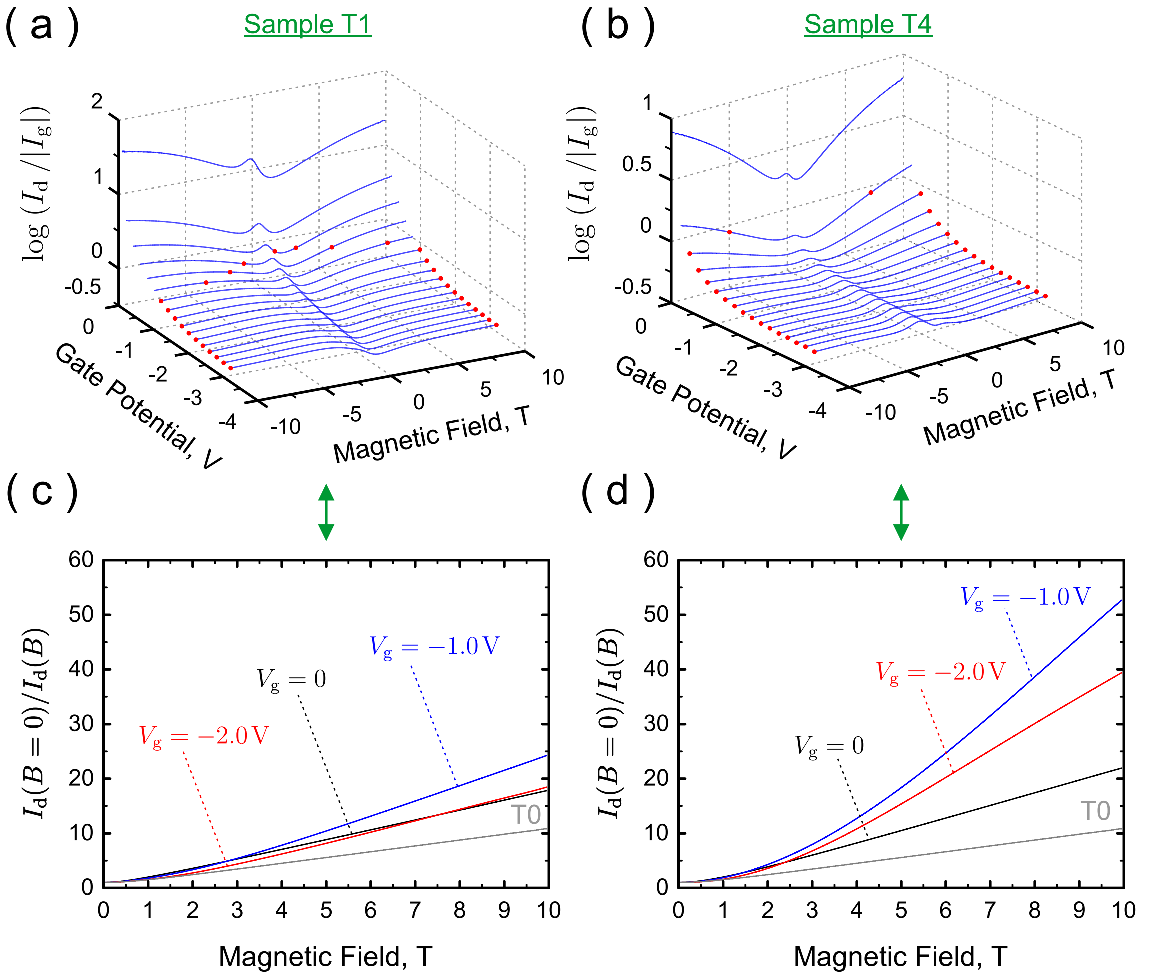

Figure 4.5: (a) and (b): The magnetic-field and gate-voltage dependence of a decimal logarithm of the drain-to-gate current ratio, $\log(I_d/|I_g|)$, (solid blue curves), plotted for the samples T1 and T4. The closed red circles superimposed on the majority of curves indicate the ends of sections, along which $|I_g| \geqslant I_d$. (c) and (d): A comparison between traces of the magnetic-field induced increase in the drain current, $I_d(0)/I_d(B)$, recorded for the structure T0 and the grating samples T1 and T4 at three different values of the gate polarization: 0, -1 V and -2 V.

In the preceding paragraph, we mentioned several times the gate-leakage current, I_g, as a potential origin of the unusual properties possessed by the GaN/AlGaN structures studied within the framework of this dissertation. In the following part we would like to discuss one more peculiar phenomenon, which in our opinion also results from a significant flow of the carriers through the gate electrode. In order to make it clear what we mean by a substantial gate current, in Figs. 4.5(a) and (b) a decimal logarithm of the $I_d(B)/|I_g(B)|$ ratio is plotted versus the magnetic field and the gate potential for the samples T1 and T4. The set of solid red circles superimposed on both graphs indicates the part of each curve that is located below 0, what corresponds to $|I_g(B)| > I_d(B)$. As can bee seen, starting from $V_g = -1.2\,\mathrm{V}$ for the structure T1 and $V_g = -0.4\,\mathrm{V}$ for the structure T4, the above relation was satisfied in the whole range of B used in our magnetotransport measurements. Under such conditions, two currents were flowing in opposite directions throughout some portions of the 2D electron channel. One of them, $I_d(B)$, was entering the 2DEG layer via the drain contact, while the second one, $I_s(B)$, was accessing the channel through the source electrode. At first sight, it might seem that except for causing the potential distribution inside the 2DEG layer to be a more complicated function of the position as compared to Fig. 2.2(a), such a configuration should not result in anything particularly interesting. However, as clearly shown in Figs. 4.5(c) and (d), it was evidently correlated with a shape-preserving enhancement of the $I_d(0)/I_d(B)$ dependence, which we have observed on all the samples equipped with grating-couplers.

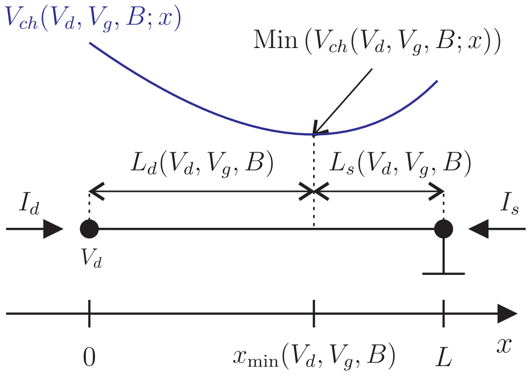

Figure 4.6: Schematic illustration of the cross-section of a leaky-gate field-effect-transistor, made along the length of the 2D electron channel (the x-axis). The blue curve represents a respective cross-section of the self-consistent electric potential distribution in the 2DEG layer.

In order to explain and describe the aforementioned phenomenon, we propose the following model. Let us consider a cross-section of a leaky-gate transistor made along the length of the 2D electron channel. It is schematically depicted in Fig. 4.6. From the fact that the two currents: $I_d(B) \equiv I_d(V_d, V_g, B)$ and $I_s(B) \equiv I_s(V_d, V_g, B)$, entering the 2DEG layer at opposite ends do not mix with each other we see, that the blue curve, $V_{ch}(V_d, V_g, B; x)$, representing an electrostatic potential distribution along the x direction, has to go through a minimum located somewhere between 0 and L. In consequence, the part of the 2DEG layer, which extends from 0 to $x_{\min}(V_d, V_g, B)$ is probed exclusively by $I_d(B)$, while in the remaining one, covering the distance from $x_{\min}(V_d, V_g, B)$ to L, only $I_s(B)$ flows towards the potential minimum. Since as displayed by Fig. 2.2(a), the current passing through a square-shaped piece of homogeneous conductor is uniformly spread over the bulk of the area, $x_{\min}(V_d, V_g, B)$ should not vary much, if at all, along the y-axis. As a result, we can assume the boundary between the two parts of the channel to be a straight line oriented perpendicularly to the x-direction and regard each of them as a rectangle of dimensions: $L_d(V_d, V_g, B) \times W$ and $L_s(V_d, V_g, B) \times W$ in the case of $I_d(B)$ and $I_s(B)$, respectively, with W denoting the width of the sample. By making next a linear approximation to the arms of the

$V_{ch}(V_d, V_g, B; x)$ curve, we can introduce the resistances $R_d(B) \equiv R_d(V_d, V_g; B)$ and $R_s(B) \equiv R_s(V_d, V_g; B)$ as:

$$R_d(B) = \frac{V_d - \text{Mean}\left\{\text{Min}(V_{ch}(V_d, V_g, B; x))\right\}}{I_d(B)}, \tag{4.4}$$

$$R_s(B) = \frac{\text{Mean}\left\{\text{Min}(V_{ch}(V_d, V_g, B; x))\right\}}{I_s(B)}, \tag{4.5}$$

where Mean{...} stands for an average over the boundary line. On the other hand, from the discussion of the geometrical magnetorsistance in the $L \sim W$ case (refer to Chapter 2), it is clear that:

$$R_d(B) = \rho_0 \frac{L_d(B)}{d_{ch} W} \sqrt{1 + \mu^2 B^2} \cdot F_{L_d(B), W, \mu}(B) + R^d_{\text{contact}}, \tag{4.6}$$

$$R_s(B) = \rho_0 \frac{L_s(B)}{d_{ch} W} \sqrt{1 + \mu^2 B^2} \cdot F_{L_s(B), W, \mu}(B) + R^s_{\text{contact}}, \tag{4.7}$$

where d_{ch} is the thickness of the 2DEG layer, ρ_0 denotes the zero-field resistivity, and $R^{d,s}_{\text{contact}}$ accounts for the resistance of electrical leads passed by the respective current. Since the expressions describing $R_d(B)$ and $R_s(B)$ are essentially the same, in what follows we will subject to further analysis only the former one. At zero magnetic field, Eqs. (4.4) and (4.6) acquire the form:

$$R_d(0) = \frac{V_d - \text{Mean}\left\{\text{Min}(V_{ch}(V_d, V_g, 0; x))\right\}}{I_d(0)} = \rho_0 \frac{L_d(0)}{d_{ch} W} + R^d_{\text{contact}}, \tag{4.8}$$

what means that:

$$\begin{aligned} \frac{I_d(0)}{I_d(B)} &= \frac{V_d - \text{Mean}\left\{\text{Min}(V_{ch}(V_d, V_g, 0; x))\right\}}{V_d - \text{Mean}\left\{\text{Min}(V_{ch}(V_d, V_g, B; x))\right\}} \times \\ &\times \frac{\dfrac{L_d(B)}{L_d(0)} \sqrt{1 + \mu^2 B^2} F_{L_d(B), W, \mu}(B) + \dfrac{d_{ch} W R_{\text{contact}}}{\rho_0 L_d(0)}}{1 + \dfrac{d_{ch} W R_{\text{contact}}}{\rho_0 L_d(0)}}. \end{aligned} \tag{4.9}$$

If $d_{ch} W R_{\text{contact}} / \rho_0 L_d(0) \ll 1$, what except for the structure T0, was actually the case of all the other samples under investigation (probably due to irreproducibility of the wire-boding), the above equation reads:

$$\frac{I_d(0)}{I_d(B)} \simeq \Phi(V_d, V_g; B) \frac{L_d(B)}{L_d(0)} \sqrt{1 + \mu^2 B^2} F_{L_d(B), W, \mu}(B), \tag{4.10}$$

where we have replaced the term with differences of electric potentials by $\Phi(V_d, V_g; B)$. Although derived by a sequence of logical steps, the expression we have just obtained cannot yield reliable estimations for the shape of the functions $L_d(B)$ and $\Phi(V_d, V_g; B)$.

Therefore, in order to become useful as a fitting formula, it has to be further simplified. The approach we propose is based on the following substitution:

$$F_{L'_d(B),W,\mu}(B) = \Phi(V_d, V_g; B)\frac{L_d(B)}{L_d(0)}F_{L_d(B),W,\mu}(B), \tag{4.11}$$

where $L'_d(B)$ is now an effective length of the area explored by the current $I_d(B)$. Then, by trying different probe functions and repeating the fitting procedure, the best candidate for $L'_d(B)$ can conveniently be established with no risk of being strongly correlated with any other fitting parameter, since the mobility that appears in (4.10) is known from the analysis of the low-field portion of the magnetotransport data (refer to discussion of Eq. (2.22) for details). When treating the results of our measurements we have examined the following functions:

$$L'_d(B) = L_0 + \alpha B \qquad L'_d(B) = \frac{L_0}{1+\alpha B} \qquad L'_d(B) = L_0 \exp\left(-\frac{B}{B_0}\right)$$

out of which the last one gave us the best agreement between Eqs. (4.10)–(4.11) and the experimental traces. Its quality is shown in Fig. 4.7 illustrating the data obtained for the sample T1 (open blue circles) along with the fitted curves drawn in red. The estimated values of the parameters which determine these curves are collected in Fig. 4.8. Although independent of the mobility, L_0 and B_0 are unavoidably correlated with each other. Therefore it is much more instructive to take a look at the shape of the full function $L'_d(V_d, V_g, B)$ they describe. The 3D plots of this function (corresponding to $V_d = 100\,\mathrm{mV}$) are depicted in Fig. 4.9(a) and (b) for the samples T1 and T4, respectively.

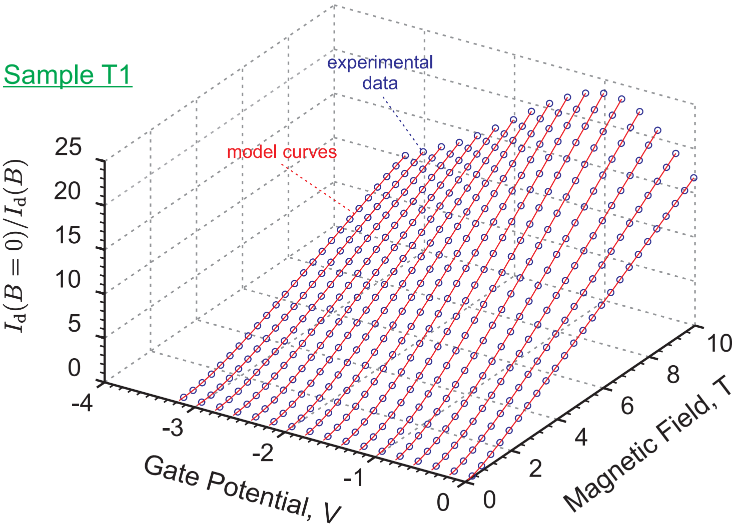

Figure 4.7: A comparison between the results of magnetotransport measurements performed on the sample T1 for different values of the gate polarization (open blue circles), and the model curves drawn in red, coming from fitting the experimental data with the formulae (4.10)–(4.11) describing an effect of the gate-leakage-current enhanced geometrical magnetoresistance.

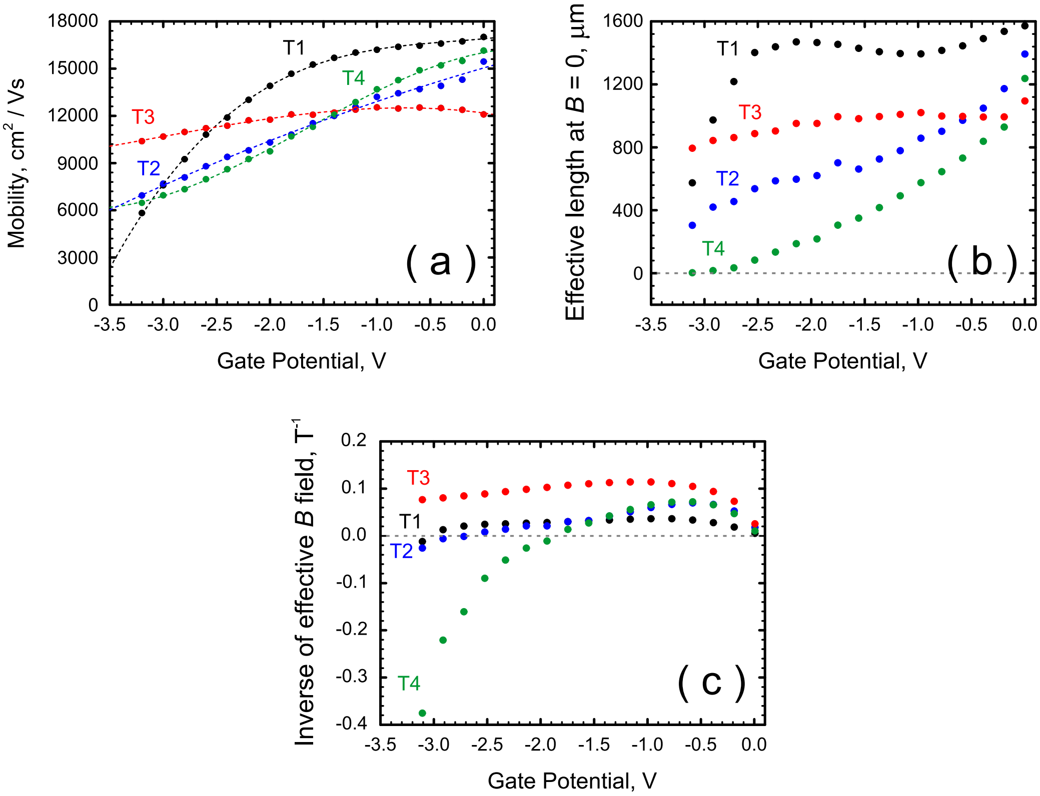

Figure 4.8: Estimations of adjustable parameters from the model of the gate-leakage-enhanced geometrical magnetoresistance, obtained by fitting the experimental data with expressions (2.22) and (4.10)–(4.11) (refer to Fig. 4.7 as an example of such a fitting) and plotted as a function of the gate potential: (a) The mobility derived from the low-field portion of the magnetotransport measurements (dashed curves are just the guides to the eye). (b) and (c): The effective length at zero magnetic field, L_0, and the inverse of the effective magnetic field, $1/B_0$, determining the shape of the probe function $L'_d(V_d, V_g, B) = L_0 \exp(-B/B_0)$ used when fitting the data with Eqs. (4.10)–(4.11).

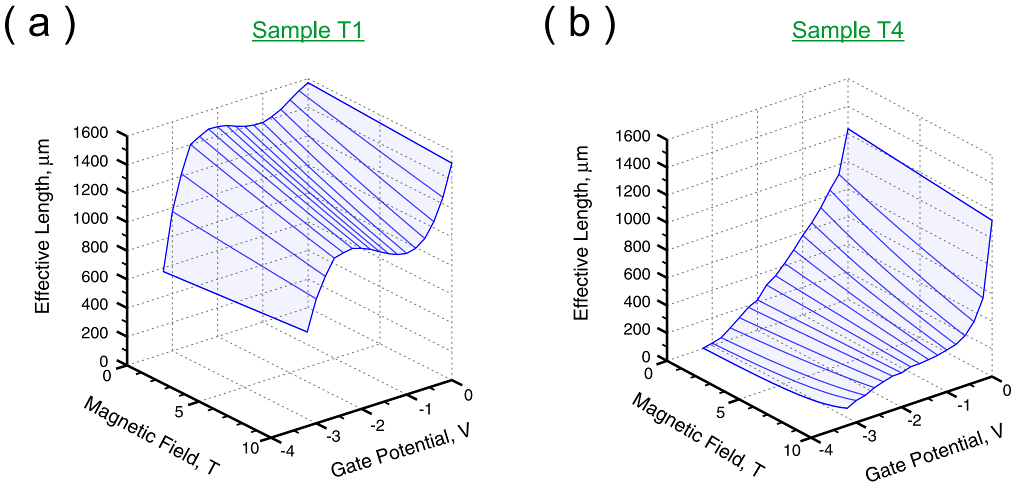

Figure 4.9: Three-dimensional plots of the effective length $L'_d(V_d, V_g, B)$ corresponding to $V_d = 100\,\mathrm{mV}$ and drawn on the basis of fitting parameters collected in Figs. 4.8(b) and (c) for the samples T1 and T4. We found the shape of the $L'_d(V_g, B)$ manifold determined for the structure T4 to be typical also for the samples T2 and T3.

Our model of the gate-leakage-current enhanced geometrical magnetoresistance may seem as a very crude approximation to the complicated situation inside the 2DEG layer. However, it not only satisfactorily fits the experimental data (as displayed by Fig. 4.7), but also gives reasonable estimations of the relevant parameters, what is clear from Fig. 4.9. Furthermore, its predictions are meaningful from both the qualitative and quantitative points of view. To see this, let us note, for instance, that for none of the samples L_0 exceeds the physical length, although no such a constriction was imposed on the fitting procedure when treating the experimental results. Therefore we feel justified to draw with its help the following conclusions:

1. Only in the sample T1, the gate tuning of the 2DEG density extended over a substantial area of the 2D electron channel. In other samples, for which Fig. 4.9(b) presents an appropriate shape of the $L'_d(V_g, B)$ manifold, changes of the 2DEG concentration were restricted to the close vicinity of the source and drain electrodes. In the central part of these structures, the carriers remained practically unaffected by the voltage applied to the grating-gate.

2. In all the samples, the effective length $L'_d(V_d, V_g, B)$ was much stronger influenced by the gate potential than the magnetic field.

As will be shown in the next section, the results of independent magnetooptical experiments on 2D magnetoplasmon excitations fully confirmed at least the first of the above-mention observations.

4.2 Magnetooptical experiments

4.2.1 Types of measurements and experimental set-ups

Two types of magnetooptical experiments have been carried out in order to probe the magnetoplasmon excitations of a 2DEG in the grating-gate GaN/AlGaN structures, which, as stated earlier, have not yet been systematically investigated in this respect.

The first one were magnetospectroscopic measurements performed at the Faculty of Physics of the University of Warsaw in the experimental set-up, which is schematically illustrated in Fig. 4.10. They were based on the use of an optically pumped far-infrared laser (FIRL), operating on methanol (CH_3OH) and providing several particularly strong lines of monochromatic radiation with the wavelengths, λ, spread over the range 70–190 µm.[2] From the point of view of the long-term stability of the output power, only one of these lines with $\lambda = 118.8\,\mu\text{m} \Leftrightarrow \nu = 2.52\,\text{THz} \Leftrightarrow \lambda^{-1} = 84.18\,\text{cm}^{-1}$ was, however, appropriate for systematic stud-

---

[2] $\lambda = 70\,\mu\text{m} \Leftrightarrow \nu = 4.28\,\text{THz} \Leftrightarrow \lambda^{-1} = 142.86\,\text{cm}^{-1} \Leftrightarrow h\nu = 17.7\,\text{meV}$ while $\lambda = 190\,\mu\text{m} \Leftrightarrow \nu = 1.58\,\text{THz} \Leftrightarrow \lambda^{-1} = 52.63\,\text{cm}^{-1} \Leftrightarrow h\nu = 6.53\,\text{meV}$.

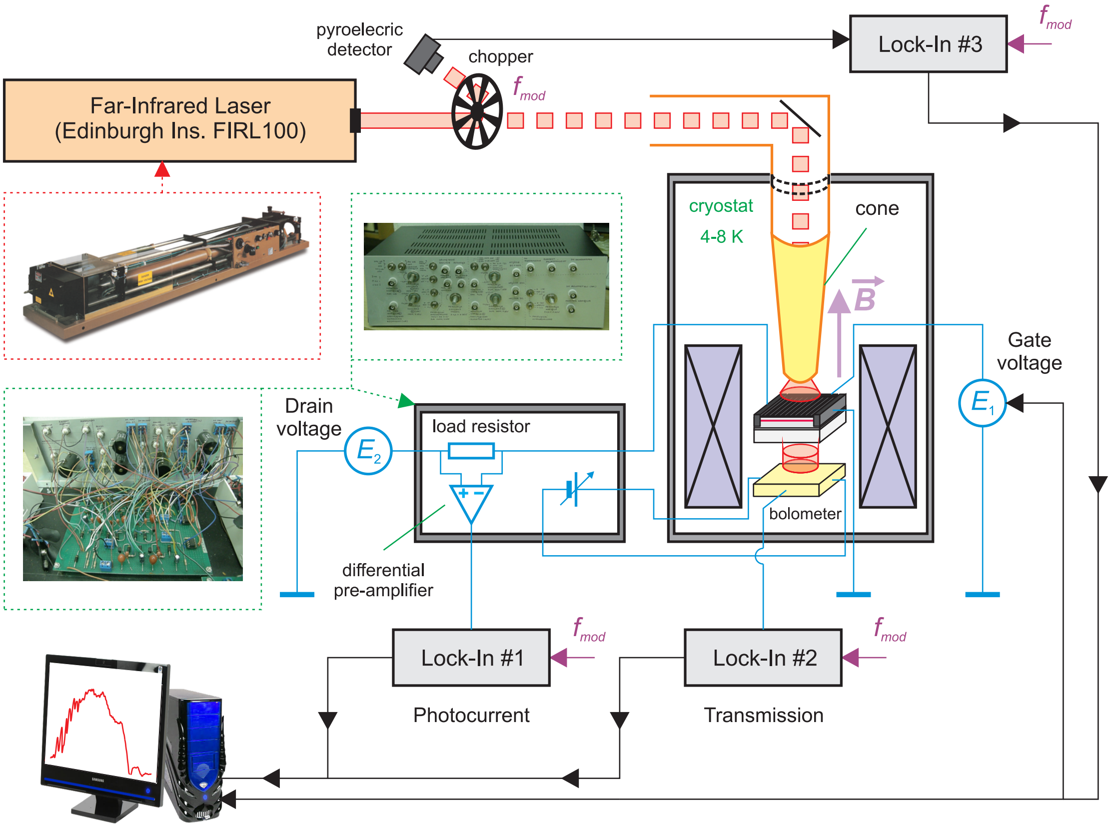

Figure 4.10: Schematic illustration of the experimental set-up used for magnetooptical measurements performed with the aid of an optically pumped far-infrared laser (FIRL). The picture of Edinburgh Ins. FIRL100 laser being a part of the equipment of the Far-Infrared and Transistor Quantum Physics Laboratory at the Faculty of Physics of the University of Warsaw is reprinted from [181].

ies. Another two with $\lambda = 96.5\,\mu\text{m} \Leftrightarrow \nu = 3.11\,\text{THz} \Leftrightarrow \lambda^{-1} = 103.63\,\text{cm}^{-1}$ and $\lambda = 163.3\,\mu\text{m} \Leftrightarrow \nu = 1.84\,\text{THz} \Leftrightarrow \lambda^{-1} = 61.24\,\text{cm}^{-1}$ served us, when necessary, to verify the frequency dependence of the features appearing in the experimental data. Because of the constant energy of the far-infrared radiation used to excite the 2D magnetoplasmon modes, the measurements were carried out either as a function of the magnetic field for a specific polarization of the gate electrode or for varying V_g but with B set to a given strength. Our initial intention was to simultaneously record both the magnetotransmission and the magnetoabsorption spectra, but due to the gate-leakage-current effects discussed in detail in the preceding section, a photocurrent (PC) underlying the latter ones, was probing too small portion of the 2DEG layer to be significantly influenced by the magnetoplasma waves. The PC traces measured as a function of B for a given V_g, confirmed, however, the results of DC magnetotransport investigations with respect to the patterns of the SdH oscillations.

The superconducting-magnet system and the sample probe used for magnetooptical experiments depicted in Fig. 4.10 were exactly the same as in the case of transport measurements. The far-infrared radiation was delivered to the sample through a pipe with a diameter of 12 mm and a truncated cone at the end to increase the intensity of the light in the close vicinity of the sample surface. Additionally, in order to prevent any short-wavelength radiation from influencing the sample, a film of black polyethylene was placed between the pipe and the cone. We haven't mentioned these features of the probe previously, since the electrical characterization of all the structures under study was carried out with no illumination (the input of the pipe capped with a piece of aluminium foil).

The power of radiation passing through the sample was monitored with the aid of a sensitive silicon bolometer operating at 4 K and firmly attached to the probe just beneath the sample holder. In order to improve its performance, we have designed and manufactured a low-noise, adjustable power supply equipped with symmetric voltage stabilizers based on the LM317 and LM337 voltage regulators and 9 V batteries (see the pictures of its front panel and the internal connections, enclosed in Fig. 4.10 by rectangles drawn with dashed green lines). Beside the bolometer unit, it also contained a low-noise differential pre-amplifier for PC measurements, built up on the basis of the OP27 operational amplifier, which enabled us to record current signals with amplitudes as low as 1 nA.

As shown in the scheme of the experimental set-up, a modulation of the laser beam was utilized to get rid of phenomena unrelated to the far-infrared illumination of the sample. The beam was switched on and off by a simple mechanical chopper rotated with a frequency $f_{\text{mod}} = 187\,\text{Hz}$ and angled at about 20° to the beam axis in order to avoid the interference effects. Another benefit from this configuration was the possibility of monitoring the FIRL output power with a pyroelectric detector collecting the part of radiation reflected off the chopper. Because of the modulation, all relevant electric signals were recorded with the aid of Lock-In amplifiers: two analogue (EG&G PAR 5210) and one digital (EG&G 7260).

The second type of magnetooptical experiments mentioned at the beginning of this section were measurements carried out at the Laboratoire National des Champs Magnétiques Intenses (LNCMI) in Grenoble, France, in the experimental set-up, which is schematically illustrated in Fig. 4.11. As can be seen, the main component of this set-up was a Fourier transform infrared spectrometer (FTIS, Bruker IFS 113v), which with a mercury lamp as a broadband source of the far-infrared radiation and the T222 multilayer beam-splitter, offered the possibility of exploring the spectral range from about $20\,\text{cm}^{-1}$ to $500\,\text{cm}^{-1}$.[3] Both the principles and technical details of the FTIS operation are well-known and comprehensively discussed in many excellent textbooks, like [182, 183], as well as in shorter, but clearly written introductions to

---

[3] $\lambda^{-1} = 20\,\text{cm}^{-1} \Leftrightarrow \lambda = 500\,\mu\text{m} \Leftrightarrow \nu = 0.6\,\text{THz}$ while $\lambda^{-1} = 500\,\text{cm}^{-1} \Leftrightarrow \lambda = 20\,\mu\text{m} \Leftrightarrow \nu = 15\,\text{THz}$.

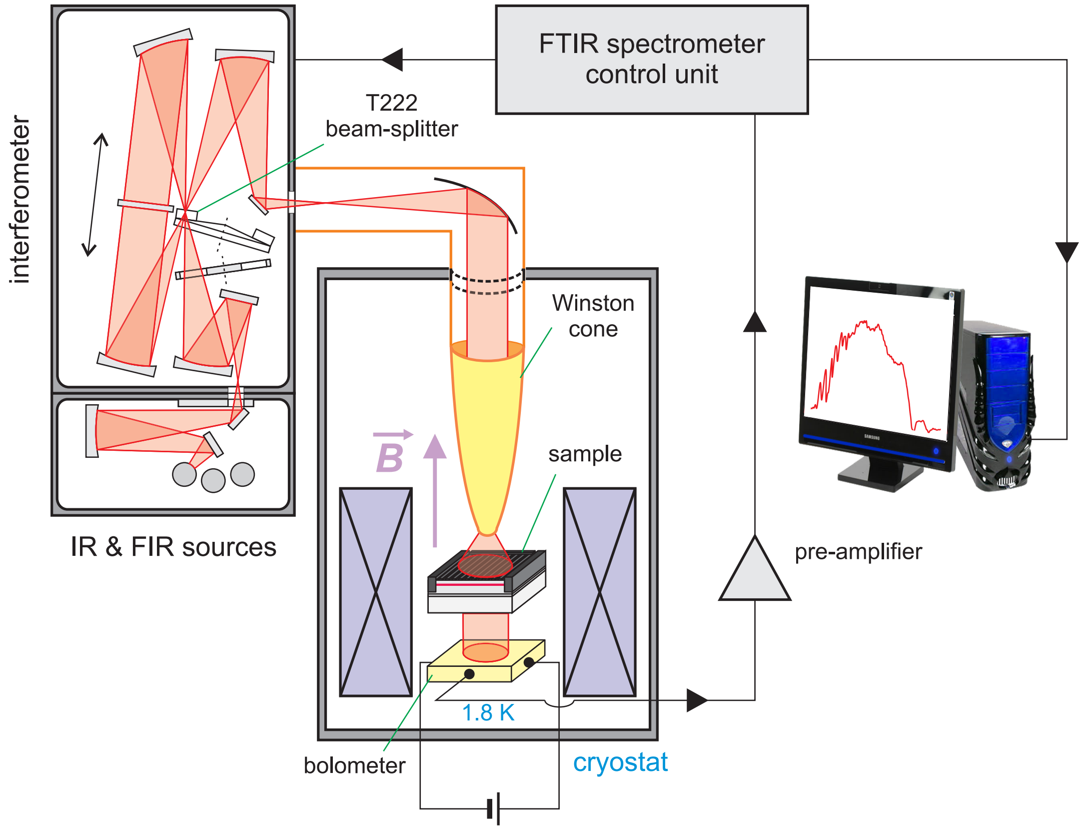

Figure 4.11: Schematic illustration of the experimental set-up used for magnetooptical measurements performed with the aid of a Fourier transform infrared spectrometer (Bruker IFS 113v), coupled with the magnetic field up to 13 T. The scheme of the optical path inside the interferometer unit of the IFS 113v spectrometer is redrawn from [6].

the subject of Fourier transform infrared spectrometry (see for example Subsection 10.3 in [6]). In the standard configuration, each FTIS provides two general modes of measurements: the recombined light[4] that leaves the interferometer unit can either be reflected off or transmitted through the sample before being focused on the detector. Because of relatively short time allocated for the experiment at the LNCMI, only the latter mode has been utilized for the purpose of this dissertation. Since our goal was to record the B-field induced changes in the transmission spectra, the far-infrared light from the interferometer's output was next directed in vacuum towards the sample mounted at the end of a probe and placed inside a superconducting coil immersed in pumped liquid helium. Under such conditions, the maximal strength of the magnetic field oriented perpendicularly to the plane of the 2DEG was equal to 13 T. After reflecting off a parabolic mirror used to create a parallel beam, the far-infrared radiation was travelling through a pipe ended with a Winston cone [184–186], which is commonly utilized in the long-wavelength optics as an efficient light concentrator.

---

[4] By recombined light we mean the light composed of superimposed beams that travelled different optical paths in the arms of the interferometer.

Finally, the power of the radiation transmitted through the sample was measured by a sensitive silicon bolometer operating at 1.8 K and connected to the FTIS control unit through a pre-amplifier in order to improve the quality of the recorded interferograms. Typically, for each value of B we were collecting 200 interferograms taken with a resolution of $2\,\mathrm{cm}^{-1}$, which were next subjected to averaging and FFT to get a spectrum. We have also tried higher resolutions: $0.5\,\mathrm{cm}^{-1}$ and $1\,\mathrm{cm}^{-1}$, but beside significantly increasing the scanning time, they only resulted in better reconstruction of dense interference fringes coming from multiple reflections of the far-infrared light between the top and back surfaces of the sapphire substrate.

4.2.2 Experimental results

4.2.2.1 Far-infrared-laser magnetospectroscopy

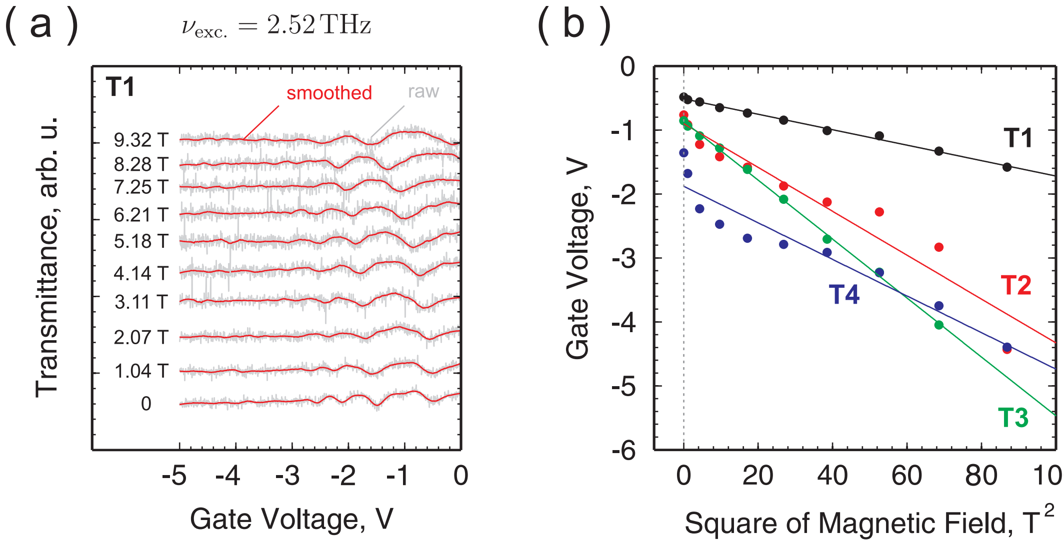

Figure 4.12: (a) Relative magnetotransmission spectra recorded at $\nu_{exc.} = 2.52\,\mathrm{THz}$ on the sample T1 as a function of the gate voltage and for a given value of the magnetic field's strength. (b) The abscissae of the first minimum (counting from the right-hand side) in transmittance spectra similar to those presented in panel (a), plotted as a function of the square of magnetic field for all the samples under study. The straight lines result from fitting the experimental data (solid circles) with Eq. (4.14).

Figure 4.12(a) presents a set of relative magnetotransmission traces recorded at $\nu_{\text{exc.}} = 2.52\,\mathrm{THz}$ on the sample T1 as a function of the gate voltage and for a given value of the magnetic field's strength. The data before and after smoothing with the Savitzky-Golay filter are shown in grey and red, respectively. In order to cover a unitary span, each of the curves was normalized prior to plotting in accordance with the following formula:

$$\left(\frac{T_{\mathrm{T1}}(B;V_g)}{T_{\mathrm{T0}}(B)}\right)_{\text{norm.}} = \frac{T_{\mathrm{T1}}(B;V_g)/T_{\mathrm{T0}}(B) - \mathrm{Min}\left\{T_{\mathrm{T1}}(B;V_g)/T_{\mathrm{T0}}(B)\right\}}{\mathrm{Max}\left\{T_{\mathrm{T1}}(B;V_g)/T_{\mathrm{T0}}(B)\right\} - \mathrm{Min}\left\{T_{\mathrm{T1}}(B;V_g)/T_{\mathrm{T0}}(B)\right\}} \quad (4.12)$$

where $T_{\mathrm{T1}}(B; V_g)$ denotes the value of transmittance measured on the structure T1 at a given V_g and B, $T_{\mathrm{T0}}(B)$ stands for the corresponding value of transmittance taken from the spectrum of the reference sample T0 and Min{...} as well as Max{...} represent the minimal and maximal value of the expression enclosed by the brackets. Clearly visible minima, which shift to more negative gate voltages as the magnetic field increases, are related to magnetoplasmon modes excited in the 2DEG layer. Various minima appearing in the same curve correspond to magnetoplasma waves characterized by different wave vectors. It is worth noting, that only the sample T1 exhibited magnetotransmission spectra composed of more than one minimum, what confirms our finding from the magnetoresistance investigations, that solely in this structure the voltage applied to the gate electrode was changing the 2DEG density over a substantial part of the electron channel.

In order to compare the experimental results collected in Fig. 4.12(a) with predictions of the theoretical model of magnetoplasma excitations developed in Chapter 1,[5] we need first to express the gate potential, V_g, in terms of 2DEG's concentration. However, because of the gate-leakage-current effects, we cannot simply use for this purpose the parameters estimated on the basis of magnetotransport data. Fortunately, if only an analytical form of the $N(V_g)$ dependence is known, its coefficients can be numerically determined with the aid of Eq. (1.94), which in the case of constant frequency of excitation, $\omega_{\mathrm{exc.}} = 2\pi\nu_{\mathrm{exc.}}$, reads:

$$\omega_{\mathrm{exc.}}^2 = \frac{N(V_g^{\mathrm{res.}})e^2}{2m^*(V_g^{\mathrm{res.}})\varepsilon_0\varepsilon_{\mathrm{eff.}}(qd)}q + \left\{\frac{eB_{\mathrm{res.}}}{m^*(V_g^{\mathrm{res.}})}\right\}^2, \tag{4.13}$$

where $m^*(V_g^{\mathrm{res.}})$ denotes an $N(V_g)$-dependent effective mass (due to the non-parabolicity corrections) and the superscript/subscript 'res.' emphasizes the fact that the above relation is valid only under resonance conditions. Although in Chapter 3 we have discussed in detail the influence of the non-parabolicity of the conduction band on the effective mass of electrons in GaN/AlGaN heterostructures, it was not possible to reliably establish the actual form of the function $m^*(V_g^{\mathrm{res.}})$ for the samples we were dealing with. Therefore in what follows we will not take it into consideration, treating $m^*(V_g^{\mathrm{res.}}) = m^*$ as just a fitting parameter. In the simplest plane-capacitor approximation (refer to Eq. (4.3)), expression (4.13) yields:

$$V_g^{\mathrm{res.}}(B_{\mathrm{res.}}, q) = -\frac{a(q)e^2}{m^*}B_{\mathrm{res.}}^2 + a(q)m^*\omega_{\mathrm{exc.}}^2 + V_{th}^{\mathrm{opt.}}, \tag{4.14}$$

---

[5] Strictly speaking, this model was formulated for a 2DEG with only a small disturbance of the equilibrium density. Therefore using it for analysis of magnetoplasmon excitations in grating-gate samples, in which the 2DEG properties can be strongly modulated by V_g, is not fully justified. However, as long as the modulation is moderate, the description of magnetoplasma oscillations in such structures should not differ much from the uniform case [15].

where: $a(q) = 2d\varepsilon_{\text{eff.}}(qd)/\varepsilon_{\text{b}}^{*}eq$, $\varepsilon_{\text{b}}^{*} \neq \varepsilon_{\text{b}}$ stands for the reduced static dielectric constant of the barrier, which effectively accounts for the gate-leakage-current-related phenomena and $V_{th}^{\text{opt.}}$ is the threshold voltage corresponding to this part of the 2DEG layer, in which the excitation of the magnetoplasma waves takes really place. Thus, $V_{g}^{\text{res.}}(B_{\text{res.}}, q)$ represents a linear function of the square of resonant magnetic field, with the slope and intercept given by: $D_1(q) = -a(q)e^2/m^*$ and $D_2(q) = a(q)m^*\omega_{\text{exc.}}^2 + V_{th}^{\text{opt.}}$, respectively. Provided that both of these parameters are known from fitting the experimental data with Eq. (4.14), $V_{th}^{\text{opt.}}$ can readily be determined as:

$$V_{th}^{\text{opt.}} = D_2(q) + \left(\frac{m^*\omega_{\text{exc.}}}{e}\right)^2 D_1(q). \tag{4.15}$$

The situation looks a bit more complicated for $\varepsilon_{\text{b}}^{*}$, since in order to estimate its value, one has to directly refer to the wave vector of the magnetoplasmon mode chosen for the above analysis. However, as displayed by the right-hand side of Eq. (4.3), we can equally well express the $N(V_g)$ dependence as:

$$N(V_g) = N_0\left(1 - \frac{V_g}{V_{th}^{\text{opt.}}}\right), \tag{4.16}$$

with the same N_0 as derived from the magnetotransport investigations summarized in Table 4.1.

In Fig. 4.12(b), the abscissae of the first minimum (counting from 0 on the gate-voltage axis) are plotted versus B^2 for all the samples under study. The straight lines drawn in the same colors as the solid circles denoting the experimental points, are described by (4.14) with the estimated values of the parameters $D_1(q)$ and $D_2(q)$ listed in Table 4.2. As can be seen, for good-quality spectra (either with relatively narrow dips (sample T1) or sufficiently low level of noise (sample T3)), the linear relationship between $V_g^{\text{res.}}$ and $B_{\text{res.}}^2$ was very well satisfied.

Name	$D_1(q)$, $\times 10^{-4}\,\text{V/T}^2$	$D_2(q)$, $\times 10^{-3}\,\text{V}$
T1	-120.8 ± 3.1	-513 ± 13
T2	-343 ± 34	-900 ± 140
T3	-460.7 ± 6.3	-864 ± 21
T4	-286 ± 31	-1880 ± 130

Table 4.2: Estimations of the adjustable parameters describing the straight lines in Fig. 4.12(a), obtained by fitting the experimental data with Eq. (4.14).

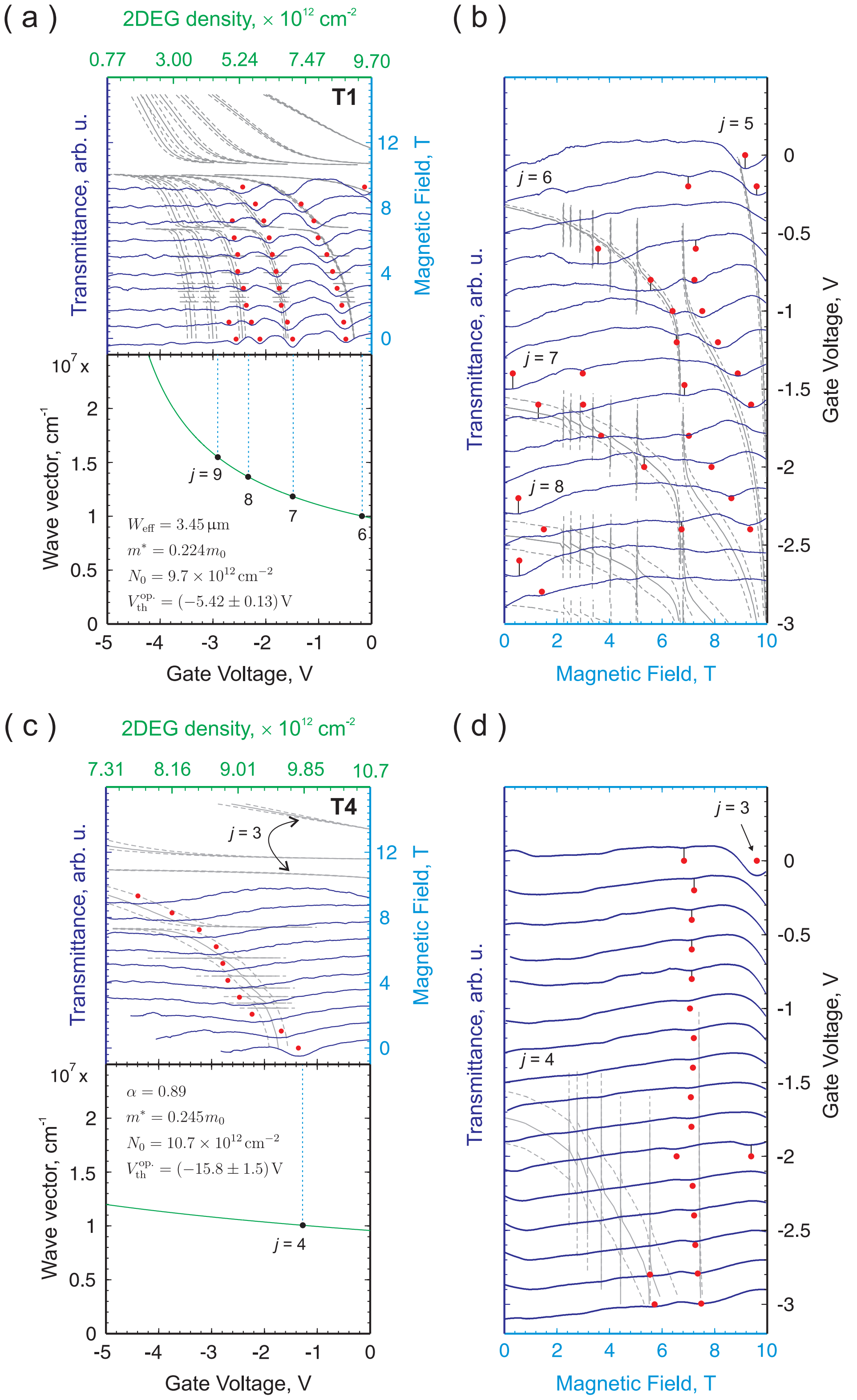

Figure 4.13: A comparison between predictions of the theoretical model of magnetoplasma oscillations developed in Chapter 1 (solid and dashed curves drawn in grey) and the relative magnetotransmission spectra (curves plotted in dark blue tones) recorded on the samples T1 (panels (a) and (b)) and T4 (panels (c) and (d)) as a function of the gate voltage for a given value of the magnetic field's strength or for varying B, but with V_g kept at the constant level. Solid red circles indicate the transmittance minima and are appropriately positioned along axes on the right-hand side.

Having determined a corrected form of the $N(V_g)$ dependence, valid for the central part of the 2DEG layer, we are able to compare the data with the model curves given by Eqs. (1.117)–(1.119) and (3.1)–(3.5). The results of such an examination are illustrated in Fig. 4.13 for the samples T1 (panels (a) and (b)) and T4 (panels (c) and (d)), respectively.[6] Diagrams (a) and (c) correspond to the measurements carried out as a function of the gate voltage for a given value of the magnetic field's strength, whereas subplots (b) and (d) present the magnetotransmission traces recorded for varying B, but with V_g kept at the constant level. The experimental curves are drawn in dark blue tones. Solid red circles indicate the transmittance minima and are appropriately positioned along axes on the right-hand side. In order to plot the model curves displayed in grey, we have performed a series of fittings in accordance with the following procedure:

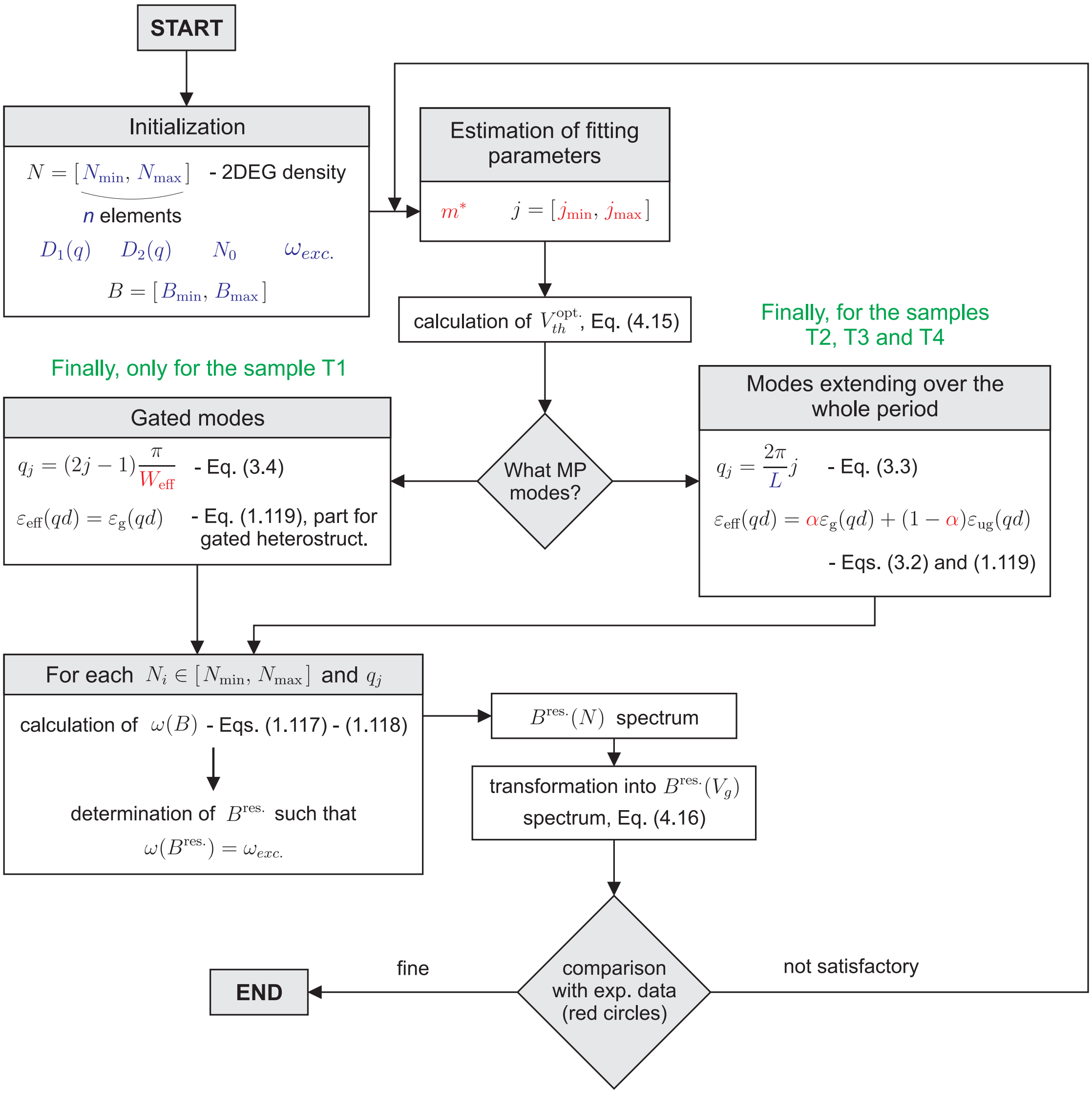

---

[6] The magnetotransmission spectra recorded for the samples T2 and T3 look very similar to those obtained for the structure T4. Therefore, we are not presenting them here.

where the input and adjustable parameters are marked in blue and red, respectively. By $W_{\text{eff}} > W$ we mean an effective width of an individual metallic gate's stripe, extended in comparison with W due to the electric-field-fringing effect, diffusion of carriers and charging of surface states on top of the AlGaN barrier. As shown in the above scheme, the best results were obtained under an assumption that the transmittance minima recorded for the sample T1 correspond to the excitation of magnetoplasma waves confined to the gated portions of the 2DEG layer, while those observed for the other samples are related to absorption of the far-infrared radiation by magnetoplasmon modes extending over the whole period of the grating-gate. It is worth pointing out, that such a conclusion remains in full agreement with the outcome of the magnetotransport measurements discussed in detail in the first part of the present chapter. Further confirmation of their validity is provided by Table 4.3 listing the estimations of fitting parameters, which determine the model curves in Fig. 4.13. First of all, for each structure, $V_{th}^{\text{opt.}}$ exceeds V_{th} from Table 4.1. Moreover, as expected from the shape of $L'_d(V_d, V_g, B)$ manifolds (refer to Fig. 4.9), the smallest, though still significant, discrepancy occurs for the sample T1. For other samples, the differences are much larger, what explains why the magnetotransmission spectra they exhibit look so similar. Secondly, the value of W_{eff} found for the structure T1 supports the hypothesis of strong enhancement of the geometrical size of each individual grating-gate's finger, extending far beyond a typical range that results from the electric-field-fringing effect and diffusion of carriers.

Name	m^*	$V_{th}^{\text{opt.}}$, V	W_{eff}, µm	α	j_{min}	$j_{\text{max.}}$
T1	0.224	-5.42 ± 0.13	3.45	–	5	9
T2	0.245	-17.6 ± 1.7	–	0.8	3	4
T3	0.242	-22.73 ± 0.30	–	0.9	3	4
T4	0.245	-15.8 ± 1.5	–	0.9	3	4

Table 4.3: Estimations of the fitting parameters describing the model curves in Fig. 4.13.

From the magnetooptical point of view, the overall agreement between the experimental data and the model curves drawn in grey with either solid (for $V_{th}^{\text{opt.}}$) or dashed (for $V_{th}^{\text{opt.}} \pm \delta V_{th}^{\text{opt.}}$) lines, can be acknowledged as satisfactory. In analogy with [61, 62], we see that in the $B \to 0$ limit, the non-local model of 2D magnetoplasma oscillations yields lower estimations for the electron gas' concentration as compared to the local description, illustrated in bottom panels of Figs. 4.13(a) and

(c) with solid green curves given by:[7]

$$V_g(q) = \left(\frac{2m^*\varepsilon_0\varepsilon_{\text{eff}}(qd)|V_{th}^{\text{opt.}}|}{N_0e^2q}\right)\left(\frac{\omega_{exc}^2-\omega_{\text{LO}}^2}{\omega_{exc}^2-\omega_{\text{TO}}^2}\right)\omega_{exc}^2 + V_{th}^{\text{opt.}}. \tag{4.17}$$

In our case, the discrepancy is, however, much smaller what may result from taking into account the plasmon-LO phonon coupling and including in the analysis a larger number of terms of the infinite series of non-local corrections to the magnetoconductivity tensor.

In accordance with the discussion from Chapter 3, the values of coefficient α obtained for samples T2, T3 and T4 are close to the $r = W/L$ ratio, but in order to reliably examine the range of validity of this approximation, structures with significantly smaller r should be considered as well.

Finally, the anti-crossings which are clearly visible in Fig. 4.13(b) indicate the excitation of Bernstein modes and their interaction with the upper-hybrid modes of different wave vectors. As stated in Chapter 1 of this dissertation, up to the best knowledge of the author, such an interaction has not yet been observed for the GaN/AlGaN heterostructures. It is also worth to point out, that they appear in the close vicinity of the model curves, what once again emphasizes the necessity of using the non-local approach when studying the properties of the magnetoplasma oscillations.

4.2.2.2 Fourier-Transform Magnetospectroscopy

Raw data treatment

When processing the data recorded with the aid of a Fourier transform infrared spectrometer for different values of the magnetic field applied to the sample, it is a common practice to divide a spectrum measured at a given B by a reference one taken at B_0 (usually $B_0 = 0$). Such a transformation leads to a relative spectrum, which does not contain any features that are insensitive to the magnetic field. Provided the characteristic width of the spectral lines we want to analyse is smaller than the B-field induced shift of their position along the energy axis, each extreme of the relative spectrum acquires clear interpretation: the minima and maxima indicate the positions of lines at B_0 and B, respectively. This case is illustrated in Fig. 4.14(a) with the help of computer generated curves, drawn in blue and magenta, that contain some constant background and a series of B-sensitive Lorentzian peaks with decreasing amplitudes, which are plotted in black and red. However, when the shift of the lines does not exceed their characteristic width, the above statement is no longer true. As shown

---

[7] Equation (4.17) is readily obtained from expression (1.116) by writing it down in the local limit and replacing the 2DEG density by (4.16).

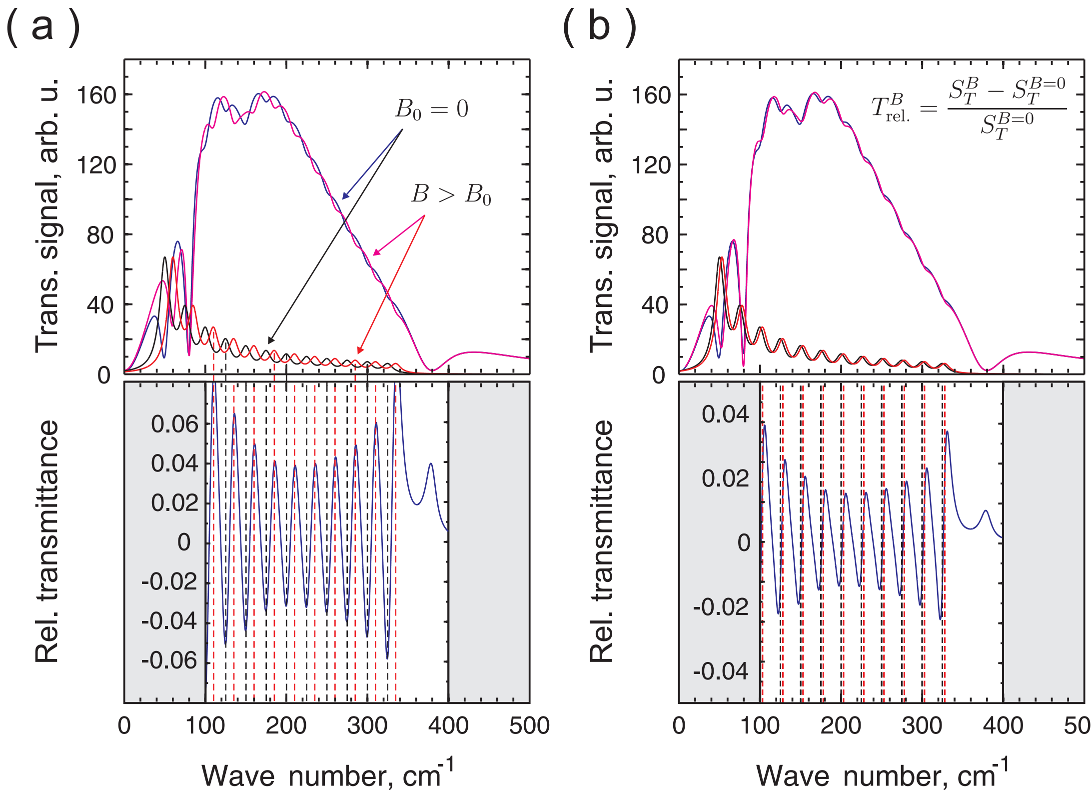

Figure 4.14: Schematic illustration of the standard way of processing the spectra measured at different magnetic fields and composed of contributions, out of which some are B-field dependent, whereas the other appear as just a constant background. In diagram (a), the B-field-induced shift of the lines drawn in black and red is larger than their characteristic width, what gives the relative transmittance spectrum a clear interpretation. Diagram (b) demonstrates the opposite situation.

in Fig. 4.14(b), the extrema of the relative spectrum, which corresponds to such conditions, do not match the actual positions of the respective peaks. Thus, a special approach to data treatment is then required.

Since when performing the Fourier measurements presented in the remaining part of this dissertation, we were mostly dealing with spectra of the latter type, we had to find some alternative way to process them prior to further analysis. The procedure we have established for this purpose was based of the following steps:

1. filtering the experimental curve (a Fourier transformed voltage signal recorded by the bolometer as a function of the position of the moving mirror inside the spectrometer) in order to remove from it the remainder of the Fabry-Pérot oscillations originating from multiple reflections of the far-infrared light inside the sapphire substrate of the GaN/AlGaN structures under study;

2. computing the upper numerical envelope, $S^B_{\text{env.}}$, of the cleansed trace, S^B_T, in accordance with the algorithm discussed in detail in Subsection 4.1.1;

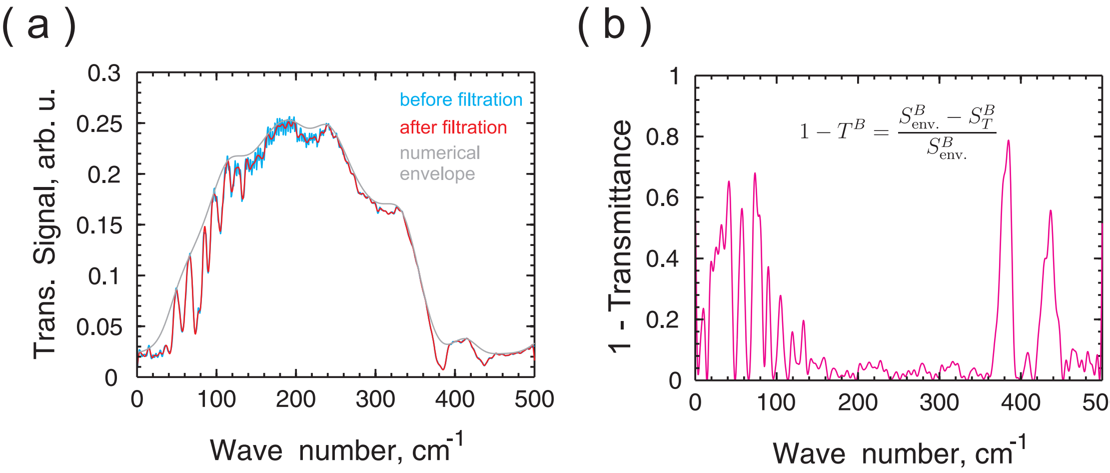

Figure 4.15: (a) Illustration of the subsequent steps of preliminary data treatment established for the purpose of this dissertation. (b) The difference between the upper numerical envelope, $S^B_{\text{env.}}$, and the filtered experimental trace, S^B_T (the grey and the red curve from panel (a), respectively) divided by $S^B_{\text{env.}}$ in order to yield a quasi-absorptance spectrum, $1-T^B$.

3. calculating the quasi-absorptance spectrum given by:

$$1-T^B=\frac{S^B_{\text{env.}}-S^B_T}{S^B_{\text{env.}}}. \tag{4.18}$$

The results of their application to the experimental data are presented in Fig. 4.15.

After completing the preliminary treatment described above, we have performed on the $(1-T^B)$ spectra one more useful numerical operation, namely, the so-called Fourier Self-Deconvolution (FSD), which helps to resolve the spectral profiles, which are composed of many overlapped lines of similar characteristic widths [187–192]. Without this step, a correct estimation of energies of closely spaced magnetoplasmon resonances, especially under strong interaction conditions (i.e. in the anti-crossing regions of the $\omega(q,B)$ diagram), would not be possible.

The FSD relies on the fact that an experimental spectrum $E(\tilde{\nu})$, where $\tilde{\nu}$ denotes a wave number, can be expressed as:

$$E(\tilde{\nu})=G(\tilde{\nu})*\tilde{E}(\tilde{\nu})=\int_{-\infty}^{+\infty}G(\tilde{\nu}')\tilde{E}(\tilde{\nu}-\tilde{\nu}')\mathrm{d}\tilde{\nu}'. \tag{4.19}$$

In the above formula, $\tilde{E}(\tilde{\nu})$ represents a real spectrum, $G(\tilde{\nu})$ determines the shape of spectral lines (i.e. the broadening, which can originate from both the physical and apparatus reasons) and $*$ stands for the convolution operation, defined as shown on the right-hand side. A real-space counterpart of $E(\tilde{\nu})$ is its interferogram, $I(x)$, given by:

$$I(x)=\mathcal{F}^{-1}\{E(\tilde{\nu})\}=\int_{-\infty}^{+\infty}E(\tilde{\nu})\exp(-2\pi i\tilde{\nu}x)\mathrm{d}\tilde{\nu}, \tag{4.20}$$

where $\mathcal{F}^{-1}\{...\}$ denotes an inverse Fourier transform [18,19]. Since a normal/inverse Fourier transform of the convolution of two functions is equal to the product of normal/inverse Fourier transforms of these functions (performed separately on each of them):

$$I(x) = \mathcal{F}^{-1}\{E(\tilde{\nu})\} = \mathcal{F}^{-1}\{G(\tilde{\nu})\} \cdot \mathcal{F}^{-1}\{\tilde{E}(\tilde{\nu})\}, \tag{4.21}$$

and thus

$$\tilde{E}(\tilde{\nu}) = \mathcal{F}\left\{\frac{I(x)}{\mathcal{F}^{-1}\{G(\tilde{\nu})\}}\right\} = \mathcal{F}\left\{\frac{\mathcal{F}^{-1}\{E(\tilde{\nu})\}}{\mathcal{F}^{-1}\{G(\tilde{\nu})\}}\right\}, \tag{4.22}$$

what means that the real spectrum can be recovered from the experimental one, provided the line profile (i.e. the analytical form of $G(\tilde{\nu})$) is known or at least can be reasonably approximated. Table 4.4 lists the most commonly observed profiles of the spectral lines together with their inverse Fourier transforms.

Name	Formula	$\mathcal{F}^{-1}\{...\} =$
Lorentz's profile	$L(\gamma;\tilde{\nu}) \equiv \dfrac{\gamma}{\pi(\tilde{\nu}^2+\gamma^2)}$	$\exp\left(-2\pi\gamma\lvert x\rvert\right)$
Gauss's profile	$G(\sigma;\tilde{\nu}) \equiv \dfrac{1}{\sqrt{2\pi}\sigma}\exp\left(-\dfrac{\tilde{\nu}^2}{2\sigma^2}\right)$	$\exp\left(-2\pi^2\sigma^2x^2\right)$
Voigt's profile	$V(\gamma,\sigma;\tilde{\nu}) \equiv L(\gamma;\tilde{\nu}) * G(\sigma;\tilde{\nu})$	$\mathcal{F}^{-1}\left\{L(\gamma;\tilde{\nu})\right\} \cdot \mathcal{F}^{-1}\left\{G(\sigma;\tilde{\nu})\right\}$

Table 4.4: A list of the most commonly observed line profiles together with their inverse Fourier transforms. $\tilde{\nu}$ denotes a wave number, while σ and γ are related to the characteristic width of the respective profiles (i.e. the full width at half-maximum, Γ) by: $\Gamma_L = 2\gamma$ and $\Gamma_G = 2\sqrt{2\ln 2}\sigma$.

The above prescription indeed yields a spectrum with significantly reduced widths of the constituent peaks as compared to the original data. However, it also generates a lot artifacts arising from quickly oscillating side lobes of the main lines, which in the worst case of constructive interference can become the most pronounced features of the resulting curve. Therefore, an important modification has to be introduced to Eq. (4.22) in order to make it more resistant to disruption by unwanted effects. It relies on multiplying the interferogram associated with the experimental spectrum by a so-called apodization function, $D_a(x)$, which sets the upper limit, L, for its length, as well as determines the way it decays to 0 at the boundaries of the $[0, L]$ range [182,183]. Thus, the central formula of the FSD can be written as:

$$\tilde{E}(\tilde{\nu}) = \mathcal{F}\left\{\frac{D_a(x)I(x)}{\mathcal{F}^{-1}\{G(\tilde{\nu})\}}\right\} = \mathcal{F}\left\{\frac{D_a(x)\mathcal{F}^{-1}\{E(\tilde{\nu})\}}{\mathcal{F}^{-1}\{G(\tilde{\nu})\}}\right\}. \tag{4.23}$$

Although there are available commercial implementations of the FSD (like in the OPUS software controlling the work of Fourier transform spectrometers produced by Bruker), they suffer from numerous constrictions: only two types of line profiles (Lorentz's and Gauss's) included in the libraries, inability to manipulate all the relevant parameters: L, γ, σ at the same time, no tools for preliminary treatment of the input data prior to calculating the final spectrum. Because of this state of affairs, we have developed for the purpose of the present thesis our own procedure, which to a large extent is free from the aforementioned limitations. Two examples of curves processed with its help are given in Fig. 4.16. In diagram (a) we show a model line drawn in blue, which is composed of two identical Lorentzian contributions (see the dashed grey curves), separated from each other by an energy smaller than the half of their characteristic width (the full width at half-maximum). In accordance with the Rayleigh criterion [193], such closely spaced lines should appear as a single one, and indeed, the shape of the blue peak does not give any indication of being more complex than just a simple Lorentz curve. In spite of this, the FSD procedure precisely reveals the positions of its constituents. In diagram (b), a part of a representative spectrum taken from our Fourier measurements is shown before and after processing with the FSD algorithm. Once again, some of the lines, which are hardly visible in the blue trace, appear as clearly distinguishable in the red one.

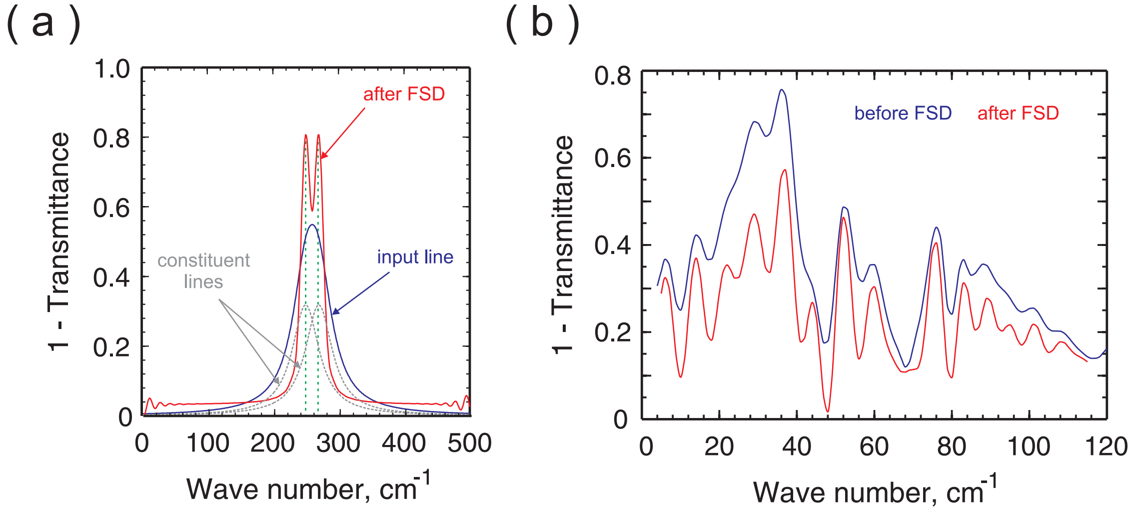

Figure 4.16: Two examples of spectra subjected to the line-narrowing procedure based on the Fourier Self-Deconvolution (FSD). (a) A computer-generated spectrum composed of a single line drawn in blue and representing the superposition of two identical Lorentzian contributions (the grey dashed curves), separated from each other by an energy smaller than the half of their characteristic width. (b) The results of application of the FSD procedure to one of the spectra recorded for the purpose of this dissertation.

Experimental results

Figure 4.17(a) displays the $(1 - T^B)$ spectra (solid blue curves) recorded on the samples T2, T3 and T4 for different values of the magnetic field's strength. The data obtained for the structure T1 are not included in the graph, since unluckily, prior to the Fourier experiments, the grating-coupler of this sample had been partially destroyed, when changing the sample holder. The red triangles indicate the positions of magnetoplasmon resonances (and the cyclotron resonance at higher magnetic field) derived from the spectra subjected to deconvolution. When performing the FSD, we made numerous trials with different line profiles and characteristic widths in order to become sure that extracted peaks are trustworthy. These computations brought us to conclusion that the best profile for the curves collected in Fig. 4.17(a), is the Voigt one with γ and σ equal to about $5\,\mathrm{cm}^{-1}$. The green triangles show two lines originating from the presence of the T222 beam-splitter in the optical path of our set-up. As can be seen, they were not moving with the magnetic field applied to the sample. Diagrams from the column (b) display the positions of all the aforementioned peaks in the way, which highlights the details of their B-field evolution. In Fig. 4.18 we compare them with predictions of the theoretical model of magnetoplasma excitations developed in Chapter 1 and modified in Chapter 3 in order to correctly describe the case of grating-gate structures. The solid blue curves represent the solutions of Eq. (1.117) limited to the first nine terms, with the high-frequency plasma oscillations given by expressions (1.118)–(1.119) and (3.2) for N, m^* and α treated as fitting parameters. The grey lines show the B-field dependence of the cyclotron resonance (CR) and its first eight harmonics (CRH). In the left part of each diagram, the $\omega(q)$ dispersion curve obtained from the above-mentioned equations written in the $B \to 0$ limit is drawn in green. The solid black circles indicate the wave vectors allowed by the grating of period L, i.e. the integer multiples of the fundamental wave vector $q = 2\pi/L$. In full agreement with [93], also in our case $j_{\max} \approx \lfloor L/(L-W) \rfloor$, where $\lfloor ... \rfloor$ denotes the floor of the number, what directly reflects the fact, that the spatial variation of the electric field just beneath the grating-coupler is closely related to the Fourier transform of its shape. As can be seen, the experimental data very closely follow the model curves. For all the samples, the anti-crossings arising from the interaction of the first-order Bernstein mode with respective upper-hybrid modes are clearly visible and perfectly reproduced by the semi-classical theory. The spectra recorded on the sample T4 contain also some traces of excitation of the second-order Bernstein mode, propagating at a frequency close to $3\omega_c$. However, measurements carried out with significantly smaller increment in the magnetic field would be required to fully justify this observation, as well as to look for other Bernstein modes of even higher orders.

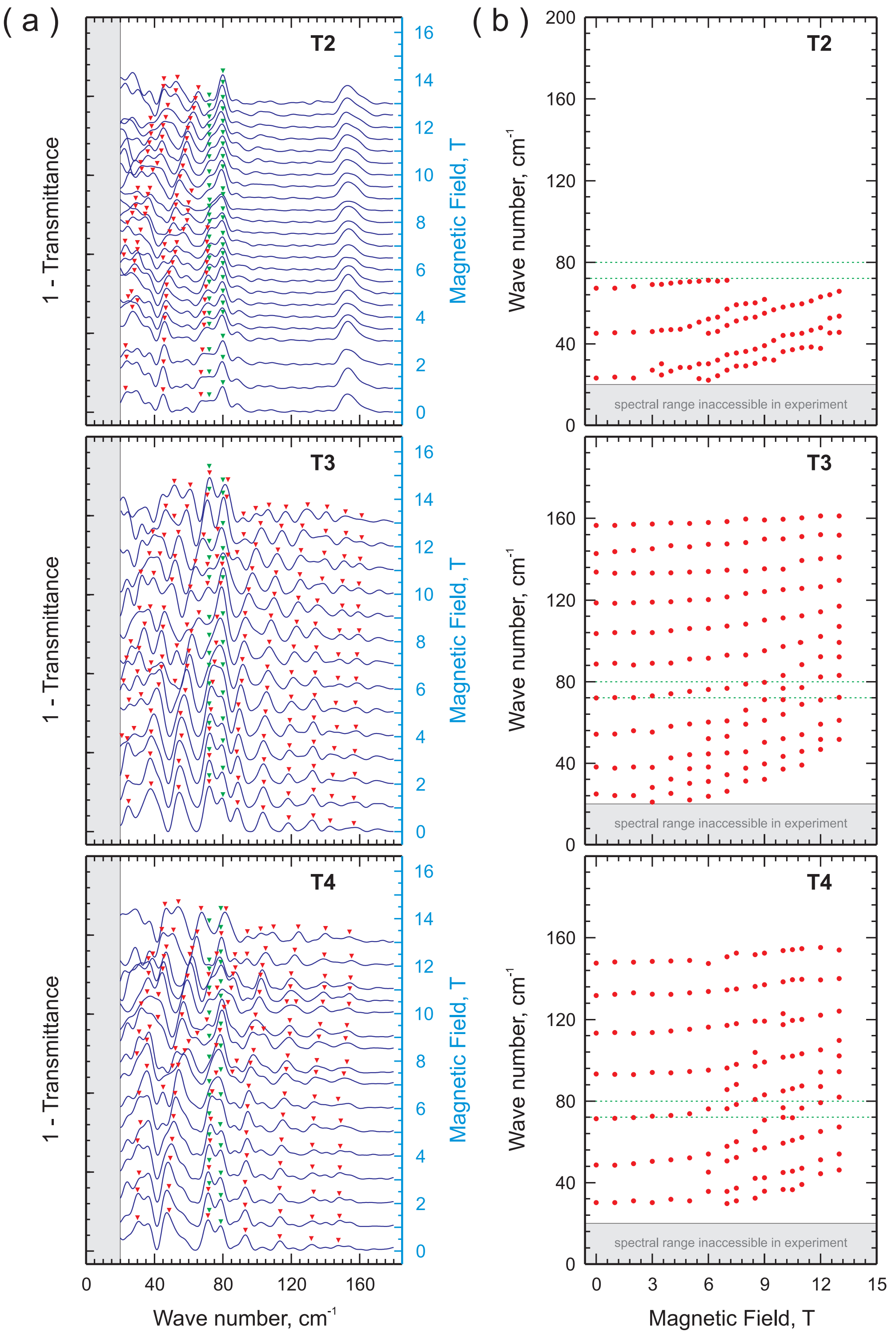

Figure 4.17: Magnetotransmission spectra recorded with the use of a Fourier transform infrared spectrometer for different values of the magnetic field's strength. The solid red triangles in panel (a) and solid red circles in panel (b) indicate the positions of maxima associated with magnetoplasmon resonances or the cyclotron resonance (CR), which becomes visible at higher magnetic field. They were all red out from the spectra subjected to a line-narrowing procedure based on the Fourier Self-Deconvolution. The green triangles show two lines recognized as originating from the presence of the T222 beam-splitter in the experimental set-up.

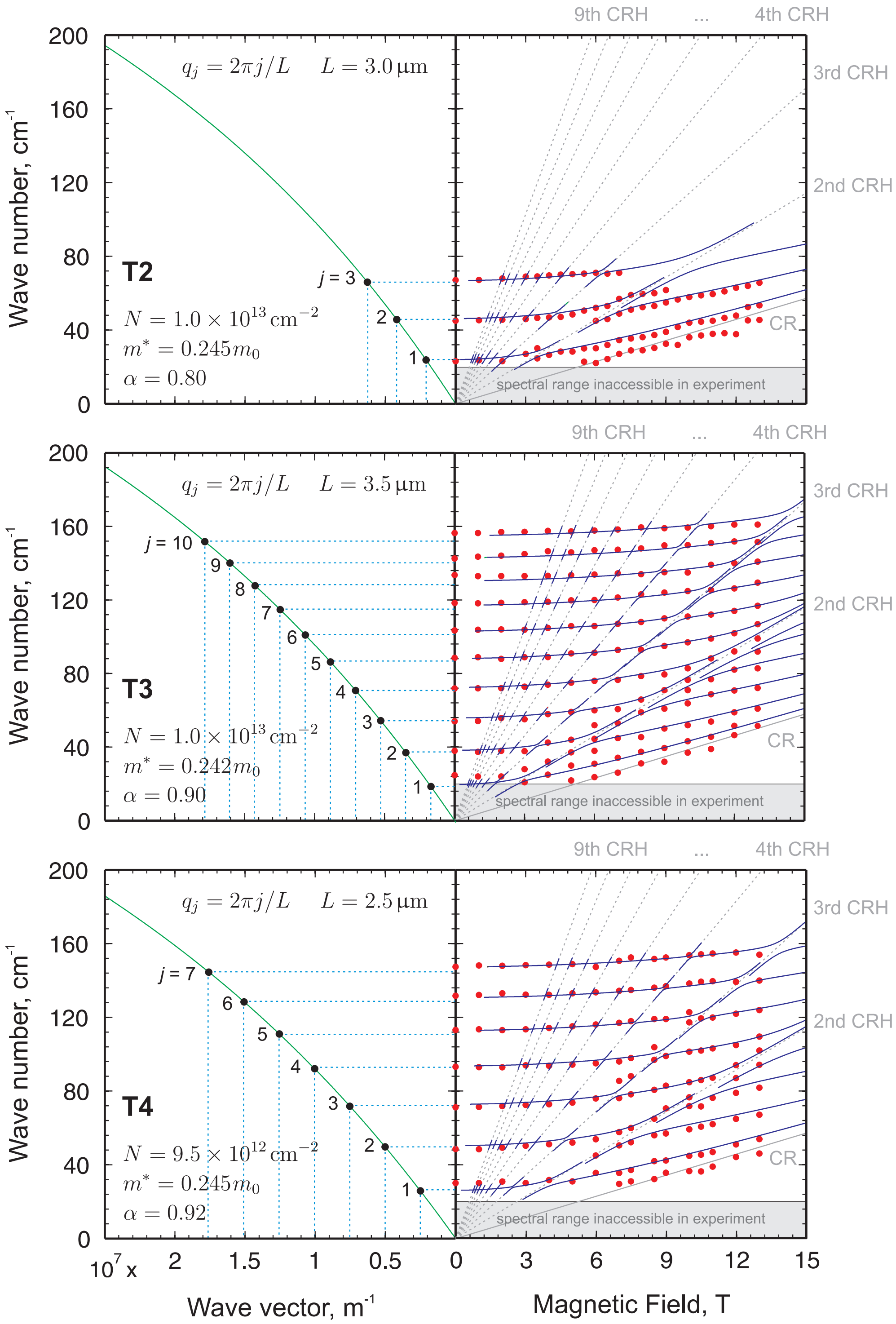

Figure 4.18: A comparison between the experimental results (solid red circles) taken from Fig. 4.17(b) and the predictions of theoretical model of 2D magnetoplasma oscillations (solid blue curves), given by Eqs. (1.117)–(1.119) and (1.118) with N, m^* and α treated as fitting parameters and the infinite series of non-local corrections to the magnetoconductivity tensor of a 2DEG limited to the first nine terms. The grey lines show the B-field dependence of the cyclotron resonance (CR) and its first eight harmonics (CRH). The $\omega(q)$ dispersion curves obtained from the above-mentioned equations written in the $B \to 0$ limit are drawn in green. The solid black circles indicate the wave vectors allowed by the grating of period L, i.e. the integer multiples of the fundamental wave vector $q = 2\pi/L$.

Summary

In summary, we have carried out detailed and systematic investigations on the magnetoplasmon excitations and the magnetotransport properties of 2DEG in large-area, grating-gate GaN/AlGaN heterostructures. Owing to relatively large periods and narrow openings of the grating-couplers as well as high concentration of the 2DEG, we were able to study numerous modes of magnetoplasma oscillations with the wave vectors and frequencies ranging from $0.2 \times 10^5\,\mathrm{cm}^{-1}$ to $1.8 \times 10^5\,\mathrm{cm}^{-1}$ and from 0.6 THz to 4.8 THz, respectively. Our measurements brought about the first observation of the Bernstein modes (up to the second order) in the GaN-based systems. Furthermore, due to high-quality of the magnetooptical data, composed of several dozens of experimental points for each sample under study, we examined the existing semiclassical theory of 2D magnetoplasmon excitations to much larger extent as reported in the literature for the GaAs/AlGaAs heterostructures. In particular, a very good agreement between the model predictions and the experimental results was found for the case of degenerate 2DEG with unmodulated density.

Our magnetotransport studies provided further evidence for the presence of acceptor-like states on top of the unpassivated AlGaN barrier, which up to now have been mainly investigated by means of a scanning capacitance microscopy. They also revealed a novel phenomenon, i.e. the gate-leakage-current-enhanced geometrical magnetoresistance, which as showed, can be a valuable tool in the sample characterization, giving insight into the spatial distributions of various quantities like the gate current density, 2DEG concentration or the local electric potential in a transistor channel.

Taking into account that there are available GaN/AlGaN structures of much better parameters as compared to the samples studied in this dissertation (significantly higher mobilities, ultra-thin barriers, negligible leakage of the gate electrode), we claim that they should be seriously considered for further exploration of plasma- and magnetoplasma-related phenomena in solid-state systems.

Bibliography

[1] H. Ehrenreich and M. H. Cohen, “Self-Consistent Field Approach to the Many-Electron Problem,” Phys. Rev. **115**, 786 (1959).

[2] J. Goldstone and K. Gottfried, “Collective Excitations of Fermi Gases,” Nuovo Cimento [10] **13**, 849 (1959).

[3] D. E. Bangert, R. J. Stuart, H. P. Hughes, D. A. Ritchie, and J. E. F. Frost, “Bernstein modes in grating-coupled 2DEGs,” Semicond. Sci. Technol. **11**, 352 (1996).

[4] F. J. Blatt, *Theory of Mobility of Electrons in Solids* (Academic Press, Inc., New York, USA, 1957), Vol. 4 of Solid State Physics, pp. 199–366.

[5] W. Greiner, *Classical Electrodynamics* (Springer-Verlag New York, Inc., New York, USA, 1998).

[6] M. Dressel and G. Grüner, *Electrodynamics of Solids: Optical Properties of Electrons in Matter* (Cambridge University Press, Cambridge, England, 2002).

[7] M. P. Greene, H. J. Lee, J. J. Quinn, and S. Rodriguez, “Linear Response Theory for a Degenerate Electron Gas in a Strong Magnetic Field,” Phys. Rev. **177**, 1019 (1969).

[8] K. W. Chiu and J. J. Quinn, “Plasma oscillations of a two-dimensional electron gas in a strong magnetic field,” Phys. Rev. B **9**, 4724 (1974).

[9] P. M. Platzman and P. A. Wolff, *Waves and Interactions in Solid State Plasmas*, Solid State Physics (Academic Press, Inc., New York, USA, 1973).

[10] S. L. Adler, “Quantum Theory of the Dielectric Constant in Real Solids,” Phys. Rev. **126**, 413 (1962).

[11] N. Wiser, “Dielectric Constant with Local Field Effects Included,” Phys. Rev. **129**, 62 (1963).

[12] M. H. Cohen, M. J. Harrison, and W. A. Harrison, "Magnetic-Field Dependence of the Ultrasonic Attenuation in Metals," Phys. Rev. **117**, 937 (1960).

[13] R. G. Chambers, "The Kinetic Formulation of Conduction Problems," Proc. Phys. Soc. A **65**, 458 (1952).

[14] R. G. Chambers, "Magneto-Resistance Effects in the Group I Metals at High Fields," Proc. R. Soc. Lond. A **238**, 344 (1957).

[15] A. V. Chaplik and D. Heitmann, "Geometric resonances of two-dimensional magnetoplasmons," J. Phys. C: Solid State Phys. **18**, 3357 (1985).

[16] J. Liouville, "Note sur la Théorie de la Variation des constantes arbitraires," J. Math. Pure Appl. **3**, 342 (1838).

[17] W. Greiner, L. Neise, and H. Stöcker, *Thermodynamics and Statistical Mechanics* (Springer-Verlag New York, Inc., New York, USA, 1995).

[18] G. B. Arfken and H. J. Weber, *Mathematical Methods for Physicists* (Elsevier Academic Press, USA, 2005), 6 edn.

[19] T. M. Apostol, *Mathematical Analysis*, World Student Series Edition (Addison-Wesley Publishing Company, Inc., USA, 1981), 5 edn.

[20] H. Flanders, "Differentiation Under the Integral Sign," Am. Math. Mon. **80**, 615 (1973).

[21] A. Erdélyi, W. Magnus, F. Oberhettinger, and F. G. Tricomi, *Higher Transcendental Functions*, Vol. 2 (McGraw-Hill Book Company, New York, 1953).

[22] H. Ibach and H. Lüth, *Solid-State Physics: An Introduction to Principles of Materials Science*, Advanced Texts in Physics (Springer-Verlag Berlin Heidelberg, Germany, 2009), 4 edn.

[23] P. Y. Yu and M. Cardona, *Fundamentals of Semiconductors: Physics and Materials Properties* (Springer-Verlag Berlin Heidelberg, Germany, 2005), 3 edn.

[24] C. Kittel, *Introduction to Solid State Physics* (John Wiley & Sons, Inc., USA, 2005), 8 edn.

[25] A. B. Pippard, *Magnetoresistance in Metals*, Cambridge Studies in Low Temperature Physics (Cambridge University Press, Cambridge, 1989).

[26] H. Haug and S. W. Koch, *Quantum Theory of the Optical and Electronic Properties of Semiconductors* (World Scientific Publishing Co. Pte. Ltd., Singapore, 2004), 4 edn.

[27] M. Drechsler, D. M. Hofmann, B. K. Meyer, T. Detchprohm, H. Amano, and I. Akasaki, "Determination of the Conduction Band Electron Effective Mass in Hexagonal GaN," Jpn. J. Appl. Phys. **79**, L1178 (1995).

[28] P. Perlin, E. Litwin-Staszewska, B. Suchanek, W. Knap, J. Camassel, T. Suski, R. Piotrzkowski, I. Grzegory, S. Porowski, E. Kaminska, and J. C. Chervin, "Determination of the effective mass of GaN from infrared reflectivity and Hall effect," Appl. Phys. Lett. **68**, 1114 (1996).

[29] Y. J. Wang, R. Kaplan, H. K. Ng, K. Doverspike, D. K. Gaskill, T. Ikedo, I. Akasaki, and H. Amono, "Magneto-optical studies of GaN and GaN/Al$_x$Ga$_{1-x}$N: Donor Zeeman spectroscopy and two dimensional electron gas cyclotron resonance," J. Appl. Phys. **79**, 8007 (1996).

[30] W. Knap, H. Alause, J. M. Bluet, J. Camassel, J. Young, M. Asif Khan, Q. Chen, S. Huant, and M. Shur, "The cyclotron resonance effective mass of two-dimensional electrons confined at the GaN/AlGaN interface," Solid State Commun. **99**, 195 (1996).

[31] W. Knap, S. Contreras, H. Alause, C. Skierbiszewski, J. Camassel, M. Dyakonov, J. Yang, Q. Chen, M. Asif Khan, M. L. Sadowski, S. Huant, F. H. Yang, M. Goiran, J. Leotin, and M. S. Shur, "Cyclotron resonance and quantum Hall effect studies of the two-dimensional electron gas confined at the GaN/AlGaN interface," Appl. Phys. Lett. **70**, 2123 (1997).

[32] H. Alause, W. Knap, S. Contreras Azema, J. M. Bluet, M. L. Sadowski, S. Huant, J. Young, M. Asif Khan, Q. Chen, and M. Shur, "Optical and electrical properties of 2-dimensional electron gas in GaN/AlGaN heterostructures," Mater. Sci. Eng. B **46**, 79 (1997).

[33] A. M. Witowski, K. Pakuła, J. M. Baranowski, M. L. Sadowski, and P. Wyder, "Electron effective mass in hexagonal GaN," Appl. Phys. Lett. **75**, 4154 (1999).

[34] T. Azuhata, T. Sota, K. Suzuki, and S. Nakamura, "Polarized Raman spectra in GaN," J. Phys.: Condens. Matter **7**, L129 (1995).

[35] F. Stern, "Polarizabilty of a Two-Dimensional Electron Gas," Phys. Rev. Lett. **18**, 546 (1967).

[36] E. D. Palik and J. K. Furdyna, “Infrared and microwave magnetoplasma effects in semiconductors,” Rep. Prog. Phys. **33**, 1193 (1970).

[37] F. Wooten, *Optical Properties of Solids* (Academic Press (New York), Inc., USA, 1972).

[38] N. J. M. Horing and R. W. Danz, “Bernstein modes and the quasiclassical model of the quantum plasma in magnetic field,” J. Phys. C: Solid State Phys. **5**, 3245 (1972).

[39] I. B. Bernstein, “Waves in a Plasma in a Magnetic Field,” Phys. Rev. **109**, 10 (1958).

[40] F. W. Crawford, “A review of cyclotron harmonic phenomena in plasmas,” Nucl. Fusion **5**, 73 (1965).

[41] J. R. Wait, *Electromagnetics and Plasmas* (Holt, Rinehart and Winston, Inc., USA, 1968).

[42] T. Kamimura, T. Wagner, and J. M. Dawson, “Simulation study of Bernstein modes,” Phys. Fluids **21**, 1151 (1978).

[43] T. H. Stix, *Waves in Plasmas* (American Institute of Physics, New York, USA, 1992).

[44] T. J. M. Boyd and J. J. Sanderson, *The Physics of Plasmas* (Cambridge University Press, New York, USA, 2003).

[45] N. J. M. Horing and G. Gumbs, “Two-dimensional magnetoplasma/Bernstein modes coupled with bulk and surface optical phonons,” Phys. Rev. B **59**, 2261 (1999).

[46] G. Gumbs, “Coupling of Bernstein modes in two- and three-dimensional plasmas and effect on their lifetimes,” Solid State Commun. **122**, 11 (2002).

[47] P. A. Wolff, “Effect of Nonparabolicity on Light Scattering from Plasmas in Solids,” Phys. Rev. **171**, 436 (1968).

[48] N. J. M. Horing, M. Orman, and M. Yildiz, “Magnetoconductivity Tensor of a Two Dimensional Plasma in Quantizing Magnetic Field,” Phys. Lett. **48A**, 7 (1974).

[49] N. J. M. Horing and M. M. Yildiz, “Quantum Theory of Longitudinal Dielectric Response Properties of a Two-Dimensional Plasma in a Magnetic Field,” Ann. Phys. **97**, 216 (1976).

[50] M. L. Glasser, “Longitudinal dielectric behavior of a two-dimensional electron gas in a uniform magnetic field,” Phys. Rev. B **28**, 4387 (1983).

[51] A. Brataas, V. Gudmundsson, A. G. Mal’shukov, and K. A. Chao, “Magnetoconductivity Tensor of a Two Dimensional Plasma in Quantizing Magnetic Field,” J. Phys.: Condens. Matter **8**, 4797 (1996).

[52] P. M. Platzman, P. A. Wolff, and N. Tzoar, “Light Scattering from a Plasma in a Magnetic Field,” Phys. Rev. **174**, 489 (1968).

[53] C. K. N. Patel and R. E. Slusher, “Light scattering from electron plasmas in magnetic field,” Phys. Rev. Lett. **21**, 1563 (1968).

[54] N. Tzoar and E.-N. Foo, “Raman Scattering by Coupled Plasmon-Cyclotron-Harmonic Modes in Semiconducting Plasmas,” Phys. Rev. **180**, 535 (1969).

[55] T. N. Theis, J. P. Kotthaus, and P. J. Stiles, “Two-Dimensional Magnetoplasmons in the Silicon Inversion Layer,” Solid State Commun. **24**, 273 (1977).

[56] E. Batke, D. Heitmann, J. P. Kotthaus, and K. Ploog, “Non-locality in the Two-Dimensional Plasmon Dispersion,” Phys. Rev. Lett. **54**, 2367 (1985).

[57] E. Batke and D. H. an C. W. Tu, “Plasmon and magnetoplasmon excitation in two-dimensional electron space-charge layers on GaAs,” Phys. Rev. B **34**, 6951 (1986).

[58] V. Gudmundsson, A. Brataas, P. Grambow, B. Meurer, T. Kurth, and D. Heitmann, “Bernstein modes in quantum wires and dots,” Phys. Rev. B **51**, 17 744 (1995).

[59] C. Steinbach, R. Krahne, G. Biese, C. Schüller, D. Heitmann, and K. Eberl, “Internal electron-electron interactions in one dimensional systems detected by Raman spectroscopy,” Phys. Rev. B **54**, 14 281 (1996).

[60] E. Ulrichs, G. Biese, C. Steinbach, C. Schüller, D. Heitmann, and K. Eberl, “One dimensional plasmons in magnetic fields,” Phys. Rev. B **56**, R12 760 (1997).

[61] J. Lefebvre, J. Beerens, Y. Feng, Z. Wasilewski, J. Beauvais, and E. Lavalée, “Far-infrared transmission study of Bernstein modes in a two-dimensional electron gas with a tunable lateral modulation,” J. Vac. Sci. Technol. A **16**, 821 (1998).

[62] J. Lefebvre, J. Beerens, Y. Feng, Z. Wasilewski, J. Beauvais, and E. Lavalée, "Bernstein modes in a laterally modulated two-dimensional electron gas," Semicond. Sci. Technol. **13**, 169 (1998).

[63] J. Lefebvre, J. Beerens, Y. Feng, Z. Wasilewski, J. Beauvais, and E. Lavalée, "Electrical transport and far-infrared transmission in a qunatum wire array," J. Vac. Sci. Technol. B **16**, 2915 (1998).

[64] V. E. Kirpichev, L. V. Kulik, I. V. Kukushkin, K. v. Klitzing, K. Eberl, and W. Wegscheider, "Direct observation of the intersubband Bernstein modes: Many-body coupling with spin- and charge-density excitations," Phys. Rev. B **59**, R12 751 (1999).

[65] L. V. Kulik, I. V. Kukushkin, V. E. Kirpichev, K. v. Klitzing, and K. Eberl, "Interaction between intersubband Bernstein modes and coupled plasmon-phonon modes," Phys. Rev. B **61**, 12 717 (2000).

[66] R. Krahne, M. Hochgräfe, C. Heyn, and D. Heitmann, "Bernstein modes in density-modulated two-dimensional electron systems and quantum dots," Phys. Rev. B **61**, R16 319 (2000).

[67] S. Holland, C. Heyn, D. Heitmann, E. Batke, R. Hey, K. J. Friedland, and C.-M. Hu, "Quantized Dispersion of Two-Dimensional Magnetoplasmons Detected by Photoconductivity Spectroscopy," Phys. Rev. Lett. **93**, 186 804 (2004).

[68] A. Wysmołek, D. Plantier, M. Potemski, T. Słupiński, and Z. R. Żytkiewicz, "Coupled plasmon-LO-phonon modes at high magnetic fields," Phys. Rev. B **74**, 165 206 (2006).

[69] J. von Neumann and E. P. Wigner, "Uber merkwürdige diskrete Eigenwerte. Uber das Verhalten von Eigenwerten bei adiabatischen Prozessen." Z. Physik **30**, 467 (1929).

[70] K. R. Naqvi and W. B. Brown, "The Non-Crossing Rule in Molecular Quantum Mechanics," Int. J. Quantum Chem. **6**, 271 (1972).

[71] L. F. Shampine, I. Gladwell, and S. Thompson, *Solving ODEs with MATLAB* (Cambridge University Press, United Kingdom, 2003).

[72] S. R. Otto and J. P. Denier, *An Introduction to Programming and Numerical Methods in Matlab* (Springer-Verlag London Ltd., USA, 2005).

[73] L. D. Landau and E. M. Lifshitz, *The Classical Theory of Fields*, Vol. 2 of Course of Theoretical Physics (Pergamon Press, Great Britain, 1971), third revised English edn.

[74] W. A. Harrison, *Solid State Theory* (Dover Publishing, Inc., New York, USA, 1979).

[75] J. M. Luttinger and W. Kohn, "Motion of Electrons and Holes in Perturbed Periodic Fields," Phys. Rev. **97**, 869 (1955).

[76] F. Bernardini, V. Fiorentini, and D. Vanderbilt, "Spontaneous polarization and piezoelectric constants of III-V nitrides," Phys. Rev. B **56**, R10 024 (1997).

[77] O. Ambacher, J. Smart, J. R. Shealy, N. G. Weimann, K. Chu, M. Murphy, W. J. Schaff, L. F. Eastman, R. Dimitrov, L. Wittmer, M. Stutzmann, W. Rieger, and J. Hilsenbeck, "Two-dimensional electron gases induced by spontaneous and piezoelectric polarization charges in N- and Ga-face AlGaN/GaN heterostructures," J. Appl. Phys. **85**, 3222 (1999).

[78] O. Ambacher, B. Foutz, J. Smart, J. R. Shealy, N. G. Weimann, K. Chu, M. Murphy, A. J. Sierakowski, W. J. Schaff, L. F. Eastman, R. Dimitrov, A. Mitchell, and M. Stutzmann, "Two dimensional electron gases induced by spontaneous and piezoelectric polarization in undoped and doped AlGaN/GaN heterostructures," J. Appl. Phys. **87**, 334 (2000).

[79] O. Ambacher, J. Majewski, C. Miskys, A. Link, M. Hermann, M. Eickhoff, M. Stutzmann, F. Bernardini, V. Fiorentini, V. Tilak, B. Schaff, and L. F. Eastman, "Pyroelectric properties of Al(In)GaN/GaN hetero- and quantum well structures," J. Phys.: Condens. Matter **14**, 3399 (2002).

[80] T. Ando, A. B. Fowler, and F. Stern, "Electronic properties of two-dimensional systems," Rev. Mod. Phys. **54**, 437 (1982).

[81] G. Bauer, F. Kuchar, and H. Heinrich, eds., *Two-Dimensional Systems, Heterostructures, and Superlattices*, Vol. 53 of Springer Series in Solid-State Sciences (Springer-Verlag Berlin Heidelberg New York Tokyo, Germany, 1984), Proceedings of the International Winter School Mauterndorf, Austria, February 26 - March 2, 1984.

[82] S. M. Sze, *Physics of Semiconductor Devices* (Wiley-Interscience, USA, 1969).

[83] J.-P. Colinge and C. A. Colinge, *Physics of Semiconductor Devices* (Kluwer Academic Publishers, USA, 2002).

[84] M. Nakayama, "Theory of Surface Waves Coupled to Surface Carriers," J. Phys. Soc. Jpn **36**, 393 (1974).

[85] A. V. Chaplik, "Possible Crystallization of Charge Carriers in Low-Density Inversion Layers," Sov. Phys. JETP **35**, 395 (1972), [Zh. Eksp. Teor. Fiz. **62**, 746 (1972)].

[86] N. Okisu, Y. Sambe, and T. Kobayashi, "Far-infrared emission from two-dimensional plasmons in AlGaAs/GaAs heterointerfaces," Appl. Phys. Lett. **48**, 776 (1986).

[87] V. V. Popov, "Plasmon Excitation and Plasmonic Detection of Terahertz Radiation in the Grating-Gate Field-Effect-Transistor Structures," J. Infrared Milli. Terahz. Waves **32**, 1178 (2011).

[88] Y. Deng, R. Kersting, J. Xu, R. Ascazubi, X.-C. Zhang, M. S. Shur, S. Gaska, G. S. Simin, M. Asif Khan, and V. Ryzhii, "Millimeter wave emission from GaN high electron mobility transistor," Appl. Phys. Lett. **84**, 70 (2004).

[89] A. El Fatimy, S. Boubanga-Tombet, F. Teppe, W. Knap, D. B. Veksler, S. Rumyantsev, M. S. Shur, N. Pala, R. Gaska, Q. Fareed, X. Hu, D. Seliuta, G. Valusis, C. Gaquiere, D. Theron, and A. Cappy, "Terahertz detection by GaN/AlGaN transistors," Electron. Lett. **42**, 1342 (2006).

[90] N. Dyakonova, A. El Fatimy, J. Łusakowski, W. Knap, M. I. Dyakonov, M.-A. Poisson, E. Morvan, S. Bollaert, A. Shchepetov, Y. Roelens, C. Gaquiere, D. Theron, and A. Cappy, "Room-temperature terahertz emission from nanometer field-effect transistors," Appl. Phys. Lett. **88**, 141 906 (2006).

[91] G. Ariyawansa, M. B. M. Rinzan, M. Strassburg, N. Dietz, A. G. U. Perera, S. G. Matsik, A. Asghar, I. T. Ferguson, H. Luo, and H. C. Liu, "GaN/AlGaN heterojunction infrared detector responding in 8–14 and 20–70 μm ranges," Appl. Phys. Lett. **89**, 141 122 (2006).

[92] N. Pala, D. Veksler, A. Muravjov, W. Stillman, R. Gaska, and M. S. Shur, "Resonant Detection and Modulation of Terahertz Radiation by 2DEG Plasmons in GaN Grating-Gate Structures," Proc. of IEEE Sensors **2007**, 570 (2007).

[93] A. V. Muravjov, D. B. Veksler, X. Hu, R. Gaska, N. Pala, H. Saxena, R. E. Peale, and M. S. Shur, "Resonant terahertz absorption by plasmons in grating-gate GaN HEMT structures," Proc. of SPIE **7311**, 73 110D (2009).

[94] A. V. Muravjov, D. B. Veksler, V. V. Popov, O. V. Polischuk, N. Pala, X. Hu, R. Gaska, H. Saxena, R. E. Peale, and M. S. Shur, "Temperature dependence of plasmonic terahertz absorption in grating-gate gallium-nitride transistor structures," Appl. Phys. Lett. **96**, 042 105 (2010).

[95] T. Onishi, T. Tanigawa, and S. Takigawa, "High power terahertz emission from a single gate AlGaN/GaN field effect transistor with periodic Ohmic contacts for plasmon coupling," Appl. Phys. Lett. **97**, 092 117 (2010).

[96] A. El Fatimy, N. Dyakonova, Y. Meziani, T. Otsuji, W. Knap, S. Vandenbrouk, K. Madjour, D. Théron, C. Gaquiere, M. A. Poisson, S. Delage, P. Prystawko, and C. Skierbiszewski, "AlGaN/GaN high electron mobility transistors as a voltage-tunable room temperature terahertz sources," J. Appl. Phys. **107**, 024 504 (2010).

[97] L. Wang, X.-S. Chen, W.-D. Hu, J. Wang, J. Wang, X.-D. Wang, and W. Lu, "The plasmonic resonant absorption in GaN double-channel high electron mobility transistors," Appl. Phys. Lett. **99**, 063 502 (2011).

[98] C. Hamaguchi, *Basic Semiconductor Physics* (Springer-Verlag Berlin Heidelberg, Germany, 2010), 2 edn.

[99] M. A. Stroscio and M. Dutta, *Phonons in Nanostructures* (Cambridge University Press, United Kingdom, 2004).

[100] R. K. Ahrenkiel and M. S. Lundstrom, eds., *Minority Carriers in III-V Semiconductors: Physics and Applications*, Vol. 39 of Semiconductors and Semimetals (Academic Press, Inc., USA, 1993).

[101] W. A. Weber and R. Merlin, eds., *Raman Scattering in Materials Science* (Springer-Verlag Berlin Heidelberg, Germany, 2000).

[102] M. O. Manasreh and H. X. Jiang, eds., *III-Nitride Semiconductors: Optical Properties I*, Vol. 13 of Optoelectronic Properties of Semiconductors and Superlattices (Taylor & Francis Books, Inc., USA, 2002).

[103] L. Challis, ed., *Electron-Phonon Interactions in Low-Dimensional Structures* (Oxford University Press, Great Britain, 2003).

[104] W. Martienssen and H. Warlimont, eds., *Springer Handbook of Condensed Matter and Materials Data* (Springer Berlin Heidelberg, Germany, 2005).

[105] T. Azuhata, T. Matsunaga, K. Shimada, K. Yoshida, T. Sota, K. Suzuki, and S. Nakamura, “Optical phonons in GaN,” Physica B **219&220**, 493 (1996).

[106] T. Deguchi, D. Ichiryu, K. Toshikawa, K. Sekiguchi, T. Sota, R. Matsuo, T. Azuhata, M. Yamaguchi, T. Yagi, S. Chichibu, and S. Nakamura, “Structural and vibrational properties of GaN,” J. Appl. Phys. **86**, 1860 (1999).

[107] N. Miura, *Physics of Semiconductors in High Magnetic Fields*, Series on Semiconductor Science and Technology (Oxford University Press, Great Britain, 2008).

[108] J. Heremans, “Solid state magnetic field sensors and applications,” J. Phys. D: Appl. Phys. **26**, 1149 (1993).

[109] D. C. Look, *Electrical Characterization of GaAs Metarials and Devices*, Design and Measurement in Electronic Engineering (John Wiley & Sons Ltd., Great Britain, 1989).

[110] D. C. Look, “Schottky-barrier profiling techniques in semiconductors: Gate current and parasitic resistance effects,” J. Appl. Phys. **57**, 377 (1985).

[111] M. M. Parish and P. B. Littlewood, “Non-saturating magnetoresistance in heavily disordered semiconductors,” Nature **426**, 162 (2003).

[112] M. M. Parish and P. B. Littlewood, “Classical magnetotransport of inhomogeneous conductors,” Phys. Rev. B **72**, 094 417 (2005).

[113] R. F. Wick, “Solution of the Field Problem of the Germanium Gyrator,” J. Appl. Phys. **25**, 741 (1954).

[114] H. J. Lippmann and F. Kuhrt, “Der Geometrieeinfluß auf den transversalen magnetischen Widerstandseffekt bei rechteckförmigen Halbleiterplatten,” Z. Naturforsch. **13a**, 462 (1958).

[115] H. J. Lippmann and F. Kuhrt, “Der Geometrieeinfluß auf den HALL-Effekt bei rechteckigen Halbleiterplatten,” Z. Naturforsch. **13a**, 474 (1958).

[116] R. W. Rendell and S. M. Girvin, “Hall voltage dependence on inversion-layer geometry in the quantum Hall-effect regime,” Phys. Rev. B **23**, 6610 (1981).

[117] B. P. Paneah, *The oblique derivative problem: the Poincaré-problem*, Vol. 17 of Mathematical Topics (Wiley-VCH, USA, 2000).

[118] R. Kubo, S. J. Miyake, and N. Hashitsume, *Quantum Theory of Galvanomagnetic Effect at Extremely High Magnetic Fields* (Academic Press, New York, 1965), Vol. 17 of Solid State Physics, pp. 269–364.

[119] L. M. Roth and P. N. Argyres, *Magnetic Quantum Effects* (Academic Press, New York, 1966), Vol. 1 of Semiconductors and Semimetals, pp. 159–202.

[120] T. Ando, "Theory of Quantum Transport in a Two-Dimensional Electron System under Magnetic Fields. IV. Oscillatory Conductivity," J. Phys. Soc. Jpn. **37**, 1233 (1974).

[121] T. Ando, Y. Matsumoto, and Y. Uemura, "Theory of Hall Effect in a Two-Dimensional Electron System," J. Phys. Soc. Jpn. **39**, 279 (1975).

[122] A. Isihara and L. Smrčka, "Density and magnetic field dependences of the conductivity of two-dimensional electron systems," J. Phys. C: Solid State Phys. **19**, 6777 (1986).

[123] P. T. Coleridge, R. Stoner, and R. Fletcher, "Low-field transport coefficients in GaAs/$\mathrm{Ga}_{1-x}\mathrm{Al}_x\mathrm{As}$ heterostructures," Phys. Rev. B **39**, 1120 (1989).

[124] S. Das Sarma and F. Stern, "Single-particle relaxation time versus scattering time in an impure electron gas," Phys. Rev. B **32**, 8442 (1985).

[125] R. B. Dingle, "Some Magnetic Properties of Metals. II. The Influence of Collisions on the Magnetic Behaviour of Large Systems," Proc. R. Soc. A **211**, 517 (1952).

[126] S. Syed, M. J. Manfra, Y. J. Wang, H. L. Stormer, and R. J. Molnar, "Large splitting of the cyclotron-resonance line in $\mathrm{Al}_x\mathrm{Ga}_{1-x}\mathrm{N}$/GaN heterostructures," Phys. Rev. B **67**, 241 304(R) (2003).

[127] S. Syed, Y. J. Wang, H. L. Stormer, M. J. Manfra, L. N. Pfeiffer, K. W. West, and R. Molnar, "Large Cyclotron-Resonance Line Splitting of Two-Dimensional Electrons in AlGaN/GaN and AlGaAs/GaAs Heterostructures," Int. J. Mod. Phys. B **18**, 3761 (2004).

[128] E. A. Henriksen, S. Syed, Y.-J. Wang, H. L. Stormer, L. N. Pfeiffer, and K. W. West, "Disorder-mediated splitting of the cyclotron resonance in two-dimensional electron systems," Phys. Rev. B **73**, 241 309(R) (2006).

[129] E. A. Henriksen, S. Syed, Y. J. Wang, M. J. Manfra, L. N. Pfeiffer, K. W. West, and H. L. Stormer, "Splitting of the cyclotron resonance in two-dimensional electron systems," Physica E **34**, 318 (2006).

[130] A. Wolos, W. Jantsch, K. Dybko, Z. Wilamowski, and C. Skierbiszewski, "Properties of the Two-Dimensional Electron Gas Confined in GaN/AlGaN Interface Studied by Electron Spin Resonance," AIP Conf. Proc. **893**, 1313 (2007).

[131] A. Wolos, W. Jantsch, K. Dybko, Z. Wilamowski, and C. Skierbiszewski, "Plasmon-cyclotron resonance in two-dimensional electron gas confined at the GaN/$\mathrm{Al}_x\mathrm{Ga}_{1-x}\mathrm{N}$ interface," Phys. Rev. B **76**, 045 301 (2007).

[132] A. Wolos, Z. Wilamowski, C. Skierbiszewski, A. Drabinska, B. Lucznik, I. Grzegory, and S. Porowski, "Electron spin resonance and Rashba field in GaN-based materials," Physica B **406**, 2548 (2011).

[133] A. V. Chaplik, "Absorption and Emission of Electromagnetic Waves by Two-Dimensional Plasmons," Surf. Sci. Rep. **5**, 289 (1985).

[134] S. J. Allen Jr., D. C. Tsui, and R. A. Logan, "Observation of Two-Dimensional Plasmon in Silicon Inversion Layers," Phys. Rev. Lett. **38**, 980 (1977).

[135] T. N. Theis, "Plasmons in Inversion Layers," Surf. Sci. **98**, 515 (1980).

[136] D. Heitmann, J. P. Kotthaus, and E. G. Mohr, "Plasmon Dispersion and Intersubband Resonance at High Wavevectors in Si(100) Inversion Layers," Solid State Commun. **44**, 715 (1982).

[137] E. Batke, D. Heitmann, A. D. Wieck, and J. P. Kotthaus, "Two-Dimensional Plasmons in Hole Space Charge Layers on Silicon," Solid State Commun. **46**, 269 (1983).

[138] E. Batke and D. Heitmann, "Charge Density and Orientation Dependence of the Effective Mass in Electron Inversion Layers on the Principal Surfaces of Si," Solid State Commun. **47**, 819 (1983).

[139] D. C. Tsui, S. J. Allen Jr., R. A. Logan, A. Kamgar, and S. N. Coppersmith, "High Frequency Conductivity in Silicon Inversion Layers: Drude Relaxation, 2D Plasmons and Minigaps in a Surface Superlattice," Surf. Sci. **73**, 419 (1978).

[140] R. Petit, ed., *Electromagnetic Theory of Gratings*, Vol. 22 of Topics in Current Physics (Springer, New York, USA, 1980).

[141] L. Zheng, W. L. Schaich, and A. H. MacDonald, "Theory of two-dimensional grating couplers," Phys. Rev. B **41**, 8493 (1990).

[142] C. D. Ager and H. P. Hughes, "Optical properties of stratified systems including lamellar gratings," Phys. Rev. B **44**, 13 452 (1991).

[143] C. D. Ager, R. J. Wilkinson, and H. P. Hughes, “Periodic grating-gate screening of plasmons in heterojunction structures,” J. Appl. Phys. **71**, 1322 (1991).

[144] V. V. Popov, M. S. Shur, G. M. Tsymbalov, and D. V. Fateev, “Higher-Order Plasmon Resonances in GaN-Based Field-Effect Transistor Arrays,” Int. J. High Speed Electron. Syst. **17**, 113 (2007).

[145] U. Mackens, D. Heitmann, L. Prager, J. P. Kotthaus, and W. Beinvogl, “Minigaps in the Plasmon Dispersion of a Two-Dimensional Electron Gas with Spatially Modulated Charge Density,” Phys. Rev. Lett. **53**, 1485 (1984).

[146] R. J. Wilkinson, C. D. Ager, T. Duffield, H. P. Hughes, D. G. Hasko, H. Ahmed, J. E. F. Frost, D. C. Peacock, D. A. Ritchie, G. A. C. Jones, C. R. Whitehouse, and N. Apsley, “Plasmon excitation and self-coupling in a bi-periodically modulated two-dimensional electron gas,” J. Appl. Phys. **71**, 6049 (1992).

[147] D. V. Fateev, V. V. Popov, and M. S. Shur, “Transformation of the Plasmon Spectrum in a Grating-Gate Transistor Structure with Spatially Modulated Two-Dimensional Electron Channel,” Semicond. **44**, 1406 (2010), [Fiz. Tekh. Poluprovodn. **44**, 1455 (2010)].

[148] S. J. Pearton, ed., *GaN and Related Materials*, Vol. 2 of Optoelectronic Properties of Semiconductors and Superlattices (Gordon and Breach Science Publishers, Amsterdam, The Netherlands, 1997).

[149] J. J. Pankove and T. D. Moustakas, eds., *Gallium Nitride (GaN) I*, Vol. 50 of Semiconductors and Semimetals (Academic Press, Inc., Great Britain, 1997).

[150] J. J. Pankove and T. D. Moustakas, eds., *Gallium Nitride (GaN) II*, Vol. 57 of Semiconductors and Semimetals (Academic Press, Inc., Great Britain, 1999).

[151] H. Morkoç, *Nitride Semiconductors and Devices* (Springer-Verlag Berlin Heidelberg, Germany, 1999).

[152] S. J. Pearton, ed., *GaN and Related Materials II*, Vol. 7 of Optoelectronic Properties of Semiconductors and Superlattices (Gordon and Breach Science Publishers, Amsterdam, The Netherlands, 2000).

[153] S. Nakamura, S. Pearton, and G. Fasol, eds., *The Blue Laser Diode: The Complete Story* (Springer-Verlag Berlin Heidelberg, Germany, 2000).

[154] M. E. Levinshtein, S. L. Rumyantsev, and M. S. Shur, eds., *Properties of Advanced Semiconductor Materials: GaN, AlN, InN, BN, SiC, SiGe* (John Wiley & Sons, United Kingdom and Canada, 2001).

[155] B. Gil, *Low-Dimensional Nitride Semiconductors* (Oxford University Press, Great Britain, 2002).

[156] P. Ruterana, M. Albrecht, and J. Neugebauer, eds., *Nitride Semiconductors: Handbook on Materials and Devices* (Wiley-VCH Verlag GmbH & Co. KGaA, Federal Republic of Germany, 2003).

[157] M. S. Shur and R. F. Davies, eds., *GaN-Based Materials and Devices: Growth, Fabrication, Characterization and Performance*, Vol. 33 of Selected Topics in Electronics and Systems (World Scientific Publishing Co., Pte. Ltd., Singapore, 2004).

[158] R. Quay, *Gallium Nitride Electronics*, Vol. 96 of Springer Series in Materials Science (Springer-Verlag Berlin Heidelberg, Germany, 2008).

[159] H. Morkoç, *Handbook of Nitride Semiconductors and Devices* (Wiley-VCH Verlag GmbH & Co. KGaA, Federal Republic of Germany, 2009), especially: *Volume 3: GaN-based Optical and Electronic Devices.*

[160] D. Ehrentraut, E. Meissner, and M. Bockowski, eds., *Technology of Gallium Nitride Crystal Growth*, Vol. 133 of Springer Series in Materials Science (Springer-Verlag Berlin Heidelberg, Germany, 2010).

[161] S. Pearton, ed., *GaN and ZnO-based Materials and Devices*, Vol. 156 of Springer Series in Materials Science (Springer-Verlag Berlin Heidelberg, Germany, 2012).

[162] R. Gaska, "Migration-enhanced MOCVD advances AlGaN performance," online article published on compoundsemiconductor.net (2005), R. Gaska is the President and CEO at Sensor Electronic Technology, Inc., Columbia, South Carolina, USA.

[163] B. R. Nag, *Physics of Quantum Well Devices*, Vol. 7 of Solid-State Science and Technology Library (Kluwer Academic Publishers, USA, 2000).

[164] J. H. Davies, *The Physics of Low-Dimensional Semiconductors: An Introduction* (Cambridge University Press, USA, 2003).

[165] O. Valleé and M. Soares, *Airy Functions and Applications to Physics* (Imperial College Press, Singapore, 2004).

[166] T. Ando, "Self-Consistent Results for a GaAs/$\mathrm{Al}_x\mathrm{Ga}_{1-x}\mathrm{As}$ Heterojunction. I. Subband Structure and Light-Scattering Spectra," J. Phys. Soc. Jpn **51**, 3893 (1982).

[167] A. Savitzky and M. J. E. Golay, “Smoothing and Differentiation of Data by Simplified Least Squares Procedures,” Anal. Chem. **36**, 1627 (1964).

[168] J. J. Harris, K. J. Lee, T. Wang, S. Sakai, Z. Bougrioua, I. Moerman, E. J. Thrush, J. B. Webb, H. Tang, T. Martin, D. K. Maude, and J.-C. Portal, “Relationship between classical and quantum lifetimes in AlGaN/GaN heterostructures,” Semicond. Sci. Technol. **16**, 402 (2001).

[169] M. Sakowicz, R. Tauk, J. Łusakowski, A. Tiberj, W. Knap, Z. Bougrioua, M. Azize, P. Lorenzini, K. Karpierz, and M. Grynberg, “Low temperature electron mobility and concentration under the gate of AlGaN/GaN field effect transistors,” J. Appl. Phys. **100**, 113 726 (2006).

[170] M. J. Manfra, S. H. Simon, K. W. Baldwin, A. M. Sergent, K. W. West, R. J. Molnar, and J. Caissie, “Quantum and transport lifetimes in a tunable low-density AlGaN/GaN two-dimensional electron gas,” Appl. Phys. Lett. **85**, 5278 (2004).

[171] C. Skierbiszewski, K. Dybko, W. Knap, M. Siekacz, W. Krupczyński, G. Nowak, M. Boćkowski, J. Łusakowski, Z. R. Wasilewski, D. Maude, T. Suski, and S. Porowski, “High mobility two-dimensional electron gas in AlGaN/GaN heterostructures grown on bulk GaN by plasma assisted molecular beam epitaxy,” Appl. Phys. Lett. **86**, 102 106 (2005).

[172] P. T. Coleridge, “Small-angle scattering in two-dimensional electron gases,” Phys. Rev. B **44**, 3793 (1991).

[173] S. Syed, M. J. Manfra, Y. J. Wang, M. J. Molnar, and H. L. Stormer, “Electron scattering in AlGaN/GaN structures,” Appl. Phys. Lett. **84**, 1507 (2004).

[174] K. V. Smith, X. Z. Dang, E. T. Yu, and J. M. Redwing, “Charging effects in AlGaN/GaN heterostructures probed using scanning capacitance microscopy,” J. Vac. Sci. Technol. B **18**, 2304 (2000).

[175] D. Mistele, O. Katz, A. Horn, G. Bahir, and J. Salzman, “Engineering and impact of surface states on AlGaN/GaN-based hetero field effect transistors,” Semicond. Sci. Technol. **20**, 972 (2005).

[176] R. F. Harrington, *Introduction to Electromagnetic Engineering* (Dover Publications, USA, 2003).

[177] M. S. Shur (2011), private communication.

[178] A. Horn, O. Katz, G. Bahir, and J. Salzman, “Surface states and persistent current photocurrent in GaN heterostructure field effect transistor,” Semicond. Sci. Technol. **21**, 933 (2006).

[179] W. Knap and G. Nowak (2012), private communication.

[180] D. C. Look and T. A. Cooper, “Schottky-Barrier Mobility Profiling Measurements With Gate-Current Corrections,” Solid State Electronics **28**, 521 (1985).

[181] “FIR Series flyer,” (2013), www.edinburghphotonics.com/lasers-leds/optically-pumped-lasers.

[182] R. J. Bell, *Introductory Fourier Transform Spectroscopy* (Academic Press, New York, USA, 1972), 2 edn.

[183] P. R. Griffiths and J. A. de Haseth, *Fourier Transform Infrared Spectrometry* (John Wiley & Sons, Inc., USA, 2007), 2 edn.

[184] R. Winston, “Light Collection within the Framework of Geometrical Optics,” J. Opt. Soc. Am. **60**, 245 (1970).

[185] R. H. Hildebrand and R. Winston, “Throughput of diffraction-limited field optics systems for infrared and millimetric telescopes,” Appl. Opt. **21**, 1844 (1982).

[186] R. H. Hildebrand and R. Winston, “Throughput of diffraction-limited field optics systems for infrared and millimetric telescopes: errata,” Appl. Opt. **24**, 616 (1985).

[187] J. K. Kauppinen, D. J. Moffatt, D. G. Cameron, and H. H. Mantsch, “Fourier Self-Deconvolution: A Method for Resolving Intrinsically Overlapped Bands,” Appl. Spectrosc. **35**, 271 (1981).

[188] J. K. Kauppinen, D. J. Moffatt, D. G. Cameron, and H. H. Mantsch, “Noise in Fourier self-deconvolution,” Appl. Optics **20**, 1866 (1981).

[189] J. K. Kauppinen, D. J. Moffatt, H. H. Mantsch, and D. G. Cameron, “Fourier Transforms in the Computation of Self-Deconvoluted and First-Order Derivative Spectra of Overlapped Band Contours,” Anal. Chem. **53**, 1454 (1981).

[190] J. K. Kauppinen, D. J. Moffatt, D. G. Cameron, and H. H. Mantsch, “Smoothing of spectral data in the Fourier domain,” Appl. Optics **21**, 1866 (1982).

[191] J. K. Kauppinen, D. J. Moffatt, M. R. Hollberg, and H. H. Mantsch, “A New Line-Narrowing Procedure Based on Fourier Self-Deconvolution, Maximum Entropy and Linear Prediction,” Appl. Spectrosc. **45**, 411 (1991).

[192] L. Smeller, K. Goossens, and K. Heremans, “How to Minimize Certain Artifacts in Fourier Self-Deconvolution,” Appl. Spectrosc. **49**, 1538 (1995).

[193] M. Born and E. Wolf, *Priciples of optics: Electromagnetic theory of propagation, interference and diffraction of light* (Cambridge University Press, United Kingdom, 1999), 7 edn.